CO lines and dust emission from merging star-forming galaxies as CMB foregrounds

Mattia Righi

München 2008

CO lines and dust emission from merging star-forming galaxies as CMB foregrounds

Mattia Righi

Dissertation
an der Fakultät für Physik
der Ludwig–Maximilians–Universität
München

vorgelegt von
Mattia Righi
aus Trento, Italien

München, den 30. April 2008

Erstgutachter: Prof. Dr. Rashid A. Sunyaev
Zweitgutachter: Prof. Dr. Gerhard Börner
Tag der mündlichen Prüfung: 3. Juli 2008

to Luisa

Restano i sogni senza tempo,
le impressioni di un momento,
le luci nel buio di case
intraviste da un treno.
Siamo qualcosa che non resta,
frasi vuote nella testa,
e il cuore di simboli pieno.

Francesco Guccini, Incontro

Contents

Zusammenfassung (Summary in German) **3**

Summary **5**

1. Introduction **7**

2. A model for star formation and dust emission in merging haloes **15**
2.1. Star formation from halo mergers 15
2.2. Lifetime of the starburst phase 17
2.3. Infrared luminosity of the haloes 19
2.4. A model for dust emission 21
2.4.1. Dust emission in the CMB thermal bath at high redshift 22

3. Three observational tests **25**
3.1. SCUBA source counts 25
3.2. Intensity of the cosmic infrared background 32
3.2.1. Escape fraction 32
3.3. The Madau plot for cosmic star formation history 34

4. Dust emission as CMB foreground **37**
4.1. Angular fluctuations from the star-forming objects 37
4.2. Results 38
4.2.1. Contribution from normal spiral galaxies 40
4.2.2. Comparison with galactic foregrounds sources 43
4.2.3. Comparison with previous works 43
4.3. Sensitivity to the parameters 45
4.3.1. Spectral parameters 46
4.3.2. Frequency dependence 46
4.3.3. Escape fraction 52
4.3.4. Gas fraction 52

4.4. Intergalactic dust 53
4.4.1. Equilibrium temperature 53
4.4.2. Radiative transfer 54
4.4.3. Average density and optical depth 55
4.4.4. The signature of intergalactic dust in the power spectrum 58

5. Carbon monoxide line emission as CMB foreground 61
5.1. Line luminosities from a sample of objects 62
5.2. The angular power spectrum 68
5.3. Results for the CO lines 70
5.3.1. Source counts and background intensity 70
5.3.2. Power spectrum of angular fluctuations 73
5.4. Angular fluctuations from fine-structure lines of atom and ions . 82
5.4.1. Comparison with similar works 84

6. Concluding remarks 87

A. The angular correlation of dust emission from star forming haloes 91
A.1. Model of measured intensity fluctuations 91
A.2. Correlation of the measured intensity fluctuations 95

B. The angular correlation of line emission from star forming haloes 99

C. Useful cosmological formulae 103
C.1. Growth factor 103
C.2. Power spectrum 104
C.3. Mass variance 104
C.4. Critical density 105
C.5. Halo bias factor 105
C.6. Distances 105

References 106

Zusammenfassung

Seit dem ersten Nachweis der Anisotropien im kosmischen Mikrowellenhintergrund (CMB) mit dem COBE-Satelliten, ist deren Erforschung ein schnell wachsendes Gebiet der modernen Astrophysik geworden. Der Erfolg der WMAP-Mission mit ihrer höheren Genauigkeit und Empfindlichkeit führt uns heute in die Ära der Präzisionskosmologie. Für die nächsten Jahre sind schon neue Experimente geplant: der PLANCK surveyor und die bodenbasierten Teleskope ACT und SPT werden große Mengen an neuen Daten mit bedeutend besserer Empfindlichkeit und Winkelauflösung liefern. In diesem Kontext wird die Erforschung der Vordergrundquellen des CMB immer detaillierter und konzentriert sich sowohl auf die galaktische Emission (Synchrotronstrahlung, Bremsstrahlung, Emission von rotierendem und vibrierendem Staub) als auch auf die (oft nicht aufzulösenden) kleinskaligen extragalaktischen Quellen (eine der bestbekanntesten ist der Sunyaev-Zel'dovich Effekt in Clustern). Auch ist der von diesen Studien abgedeckte Frequenzbereich sehr groß, um den heutigen und zukünftigen Beobachtungsmissionen mit ihrer großen Anzahl an Frequenzkanälen Rechnung zu tragen. Es ist wichtig zu erwähnen, dass die verschiedenen Vordergrundquellen nicht nur eine Behinderung bei der Beobachtung des primordialen CMB-Signals darstellen, sondern sich auch als ein mächtiges Instrument für die Bestimmung der physikalischen Eigenschaften der Vordergrundquellen selbst herausstellen könnten. Hierfür ist es entscheidend, dass in vielen verschiedenen Frequenzbändern beobachtet wird.

In dieser Dissertation entwickle ich ein auf dem Press-Schechter Formalismus beruhendes Modell (veröffentlicht in Righi et al, 2008) um eine Ansammlung verschmelzender, sternbildender Objekte im Universum und ihre Wärmestrahlung zu untersuchen. Die Wärmestrahlung entsteht durch die Reprozessierung des von neu entstandenen Sternen emittierten ultravioletten Lichts durch Staub. Die sogenannte Kennicut-Relation besagt, dass die Sternentstehungsrate in Galaxien sehr stark mit der Leuchtkraft im fernen Infrarot (8-1000 μm) korreliert ist. Dies erlaubt es mir, zwischen der Verteilung von verschmelzenden, sternbildenden Objekten im Universum und deren Leuchtkraftfunktion im

Infraroten eine Verbindung herzustellen. Ich zeige, dass die Verklumpung solcher Objekte im $150-350$ GHz-Band und auf Winkelskalen von Bogenminuten eine bedeutende Vordergrundquelle ist. Dies wird für die hohen Frequenzkanäle von PLANCK und für ACT und SPT von besonderer Wichtigkeit sein. Andere Projekte wie CCAT, ASTE, APEX und ALMA werden, obwohl sie nicht auf die Erforschung des CMB ausgelegt sind, ähnliche Frequenzbereiche abdecken und können daher die Eigenschaften dieser Objekte gut einschränken.

Die selben sternbildenden Regionen, von welchen die Staubemission herrührt, geben große Mengen an Metallen an das interstellare Medium ab: die erste Generation von Sternen im frühen Universum produziert Kohlenstoff und Sauerstoff schon bei sehr hoher Rotverschiebung ($z \sim 15-20$). Die Rotationsübergänge des Kohlenmnoxydmoleküls verursachen sehr starke Emissionslinien, sowohl in lokalen Objekten als auch in Objekten hoher Rotverschiebung, wie von vielen Beobachtungen belegt wird. Ich kombiniere die vorhandenen Beobachtungsdaten mit dem "merging model" und zeige, dass die Emission in diesen Linien einen bedeutenden Einfluss auf das Leistungsspektrum des CMB im $10-60$ GHz-Band haben könnte, wo das Signal des Staubs stark abnimmt. Darüber hinaus demonstriere ich, wie Beobachtungen mit unterschiedlicher spektraler Auflösung die Amplitude der Fluktuation um eine Größensordnung verstärken können und es somit erlauben, die Signatur der Linien von anderen Vordergründen zu unterscheiden, die von Kontinuumsemission herrühren. Beobachtungen in verschiedenen Frequenzkanälen werden es ermöglichen, unterschiedlich weit entfernte Regionen des Universums zu untersuchen und Informationen über die Geschichte der Sternentstehung, die Anreicherung von Metallen im Universum und die Epoche der Reionisation zu erhalten.

Die Dissertation gliedert sich wie folgt: im ersten Kapitel wird ein kurzer Überblick gegeben, im zweiten Kapitel wird das "merging model" beschrieben und die Verbindung zur Staubemission erklärt. Das dritte Kapitel beinhaltet eine Beschreibung der drei beobachtungsbasierten Tests, die durchgeführt wurden um das Modell zu kalibrieren. Im vierten Kapitel präsentiere ich die Ergebnisse für die kontinuierliche Staubemission, während das fünfte Kapitel sich mit der Linienemission beschäftigt. Die technischen und mathematischen Aspekte der Arbeit werden im Detail in den Anhängen dargestellt.

Summary

Since the first detection of anisotropies in the Cosmic Microwave Background (CMB) by the COBE satellite, their study has been a rapidly growing branch of modern astrophysics. The success of the WMAP mission, with its higher accuracy and sensitivity, is now leading us to the era of precision cosmology. New experiments are already planned for the next years: the PLANCK surveyor and the ground-based ACT and SPT telescopes will provide large new datasets with significant improvements in both sensitivity and angular resolution. In this context, the study of the CMB foreground sources is becoming even more detailed and it is focusing on both the large-scale galactic emission (synchrotron, free-free, rotating and vibrating dust) and the (often unresolved) small-scale extragalactic populations (Sunyaev-Zel'dovich effect from clusters is one of the best-known). The range of frequencies covered by these studies is also very wide, given the large number of channels designed for present and future observations. It is worthy of mention that the different foreground sources are not only an obstacle to the detection of the primary CMB signal, but that they might become a powerful tool to explore the physical properties of the intervening sources themselves. In this sense, multifrequency observations are crucial.

In this thesis, I will develope a model (reported in Righi et al. 2008), based on the extended Press-Schechter formalism, to study a population of merging star-forming objects in the universe and their thermal emission due to the reprocessing by dust of ultraviolet light emitted by newly born stars. The star-formation rate in galaxies is known to correlate very well with far-infrared ($8 - 1000\,\mu$m) luminosity through the so-called Kennicutt relation. This allows me to link the distribution of merging star-forming objects in the universe to their infrared luminosity function. I will demonstrate that the clustering of this kind of population will be a significant source of foreground in the $150-350$ GHz band and on arcminute angular scales. This will be particulary important for the high-frequency channels of PLANCK and for ACT and SPT. Other projects, like CCAT, ASTE, APEX and ALMA, though not designed for CMB studies will cover similar bands and might therefore provide precise constraints on this

population.

The same star-forming regions that are responsible for dust emission inject large amounts of metals into the insterstellar medium: the first generation of stars in the early universe produces carbon and oxygen already at very high redshift ($z \sim 15 - 20$). The transitions between the rotational levels of carbon monoxide molecule give rise to very bright emission lines in both local and high-redshift objects, as demonstrated by many observations. Combining the available observational data with the merging model, I will show that the emission in these lines might leave a significant imprint in the angular power spectrum in the $10 - 60$ GHz band, where the signal from dust strongly decreases. Furthermore, I will demonstrate how observations with different spectral resolutions can boost the amplitude of the fluctuations by over one order of magnitude and allow one to distinguish the signature of the lines from other foregrounds generated by continuum emission. Observations in different channels will give the possibility to probe different slices of the universe and to put constraints on the history of star formation, of metal enrichment of the universe and on the reionzation epoch.

The thesis is organized as follows: a short overview is given in Chapter 1, the merging model is outlined in Chapter 2 and the link with the dust emission is explained. The three observational tests performed to calibrate the model are described in Chapter 3. In Chapter 4 I present the results for the dust continuum emission, while Chapter 5 is devoted to the emission in the lines. The technical and mathematical aspects of the work are presented in detail in the Appendixes.

1 Introduction

Three very important CMB experiments are due to operate in the next two years: the PLANCK surveyor spacecraft (Tauber 2004) and two ground based experiments, ACT (Kosowsky 2006) and SPT (Ruhl et al. 2004). They will cover the $150-350$ GHz frequency range with a resolution of a few arcminutes and with unprecedented sensitivity. A lot of work has been devoted in the last years to the study of possible foreground sources for these relatively high CMB frequencies.

The galactic dust radiation is obviously the most well known foreground source (Schlegel et al. 1998; Tegmark et al. 2000) on the large and intermediate angular scales relevant for CMB observations, but it is very important also to look for foreground sources that have significant power at small angular scales (i.e. in the multipole range $l \sim 10^3 - 10^4$). Several well-studied foregrounds, like clusters of galaxies, observable with the thermal and kinetic SZ effects (Sunyaev & Zeldovich 1972, 1980; Komatsu & Kitayama 1999; Hernández-Monteagudo et al. 2006), SCUBA galaxies (Scott & White 1999) and bright infrared galaxies (Sanders & Mirabel 1996; Lagache et al. 2005) are predicted to contribute significantly to the angular power spectrum of the fluctuations measured by the instruments mentioned above. It is relevant that these foregrounds are not only considered as difficulties impeding the study of primordial angular fluctuations, but that they might also provide us with extremely useful information on the statistical properties of objects like clusters of galaxies and compact

sub-millimeter sources, and about the history of enrichment by heavy elements (Basu et al. 2004). There are several projects, including APEX (Güsten et al. 2006), ASTE (Kohno 2005) and CCAT (Sebring et al. 2006), which also plan to observe the sky in the sub-millimeter band.

In this thesis, I will study the consequences of a simple model in which haloes become bright in sub-millimeter wavelengths due to intense star formation resulting from mergers and the corresponding supply of fresh gas. I use the Lacey & Cole (1993) approach, based on the extended Press-Schechter formulation, to obtain the space density of the haloes in the universe. Knowing the space density of merging objects as a function of final mass and of the progenitor mass, I then introduce the lifetimes of the bright star formation phase as derived from numerical simulations of merging gas-rich disk galaxies. Using the Kennicutt relation between star formation rate and infrared luminosity (Kennicutt 1998) and taking into account that the bulk of infrared luminosity of the galaxies with intense star formation peaks in the sub-millimeter band at $\lambda \sim 100$ μm, I obtain the luminosity function of the merging sub-millimeter objects. The emission spectrum of optically thin dust is a strongly increasing function of frequency (close to $\nu^{2+\beta}$, with $\beta = 1.5$, Hildebrand 1983). Therefore distant objects are observed at a rest-frame frequency closer to the peak of their spectrum. At frequencies below 1000 GHz, there is strong K-correction and the flux from galaxies at $z > 1$ remains approximately constant with increasing redshift (Blain et al. 2002).

Recent observations of quasars at very high redshift ($z \sim 6$) and of extremely massive galaxies at $z > 4$ show that the chemical abundance of the gas (including dust) in the most dense parts of star-forming galaxies is close to or exceeds the solar value (Fan 2006). Therefore it is natural to assume that the dust radiation spectrum does not change dramatically with the redshift of the merging objects. This is the weakest assumption of this work, which might lead to some changes in the dust emission spectrum at very high redshift when the abundance of heavy elements in gas and dust will drop below $10^{-2} - 10^{-3}$ of the solar value. Nevertheless, observations of the Magellanic Clouds indicate that absorption and emission of dust remains similar to that in the Milky Way, when the abundance of chemical elements is changing by one order of magnitude (Li & Draine 2002).

This simple approach permits me to obtain several predictions that can be compared with the experimental results:

1. the star formation rate density in the universe as function of redshift (i.e. the *Madau plot*, Madau et al. 1996, 1998; Hopkins 2004; Hopkins &

Beacom 2006);

2. the upper limit on the intensity of the infrared background set by COBE-FIRAS observations (Fixsen et al. 1998);

3. the source counts of sub-millimeter sources performed by SCUBA (Coppin et al. 2006);

4. the redshift distributions of the brightest SCUBA sources (Chapman et al. 2005).

This model explains all but one of the above experiments. It demonstrates a deficiency of the brightest sources in comparison with the SCUBA data, but much more importantly it shows that the redshift distribution of the brightest objects is also significantly different. I am then forced to make the simplest conclusion that SCUBA is observing objects of a different nature. Forthcoming SPT and ACT deep surveys will be able to find an additional population of sub-millimeter sources, since at the sensitivity levels of these instruments, up to $\sim 50\%$ of all detected objects should be merging galaxies. This population should have a different redshift distribution than the SCUBA objects. Much deeper surveys with ALMA (Tarenghi & Wilson 2005) could also be dominated by sub-millimeter objects connected with merging galaxies, depending on the properties of SCUBA sources, whose exact physical nature is still a matter of debate. Ongoing observations with SPITZER and the future results of Herschel will give additional clues about the merging population in the infrared observations.

The merging model is able to produce a rather good fit to the SCUBA source counts if the dust temperature is close to 25 K, but this value is not in agreement with the numbers presented in the SCUBA papers. Additional energy coming from relatively weak AGN inside the merging objects could increase the flux from individual sources and mimic the source counts curve of SCUBA.

The results of my computations show that the dust emission of the merging objects should be one of the key foreground sources for primordial fluctuations of CMB, in the very broad range of angular scales $l \simeq 10^2 - 10^4$. The model demonstrates the importance of the correlation term in providing the fluctuations due to haloes at high redshift ($z \simeq 2 - 6$) and that its contribution exceeds the predictions for the Poisson fluctuations in the number of star forming haloes. In this way I confirm earlier conclusions of Haiman & Knox (2000), about the importance of the correlation signal, which were based on a different

model of sub-millimeter sources and on a different statistical characterization of the population (number of haloes instead of number of mergers).

The correlation term from the relatively small mass ($10^8 - 10^{11}\,M_\odot$) but numerous merging objects gives a contribution that samples the typical comoving correlation length of these objects ($\lesssim 10\,h^{-1}$Mpc). This signal probes the most overdense regions in the universe at high redshift, that eventually will give rise to clusters and superclusters of galaxies. The Poisson term is smaller than the correlation term up to $l \sim 3000$, but becomes more important at higher l. ACT and SPT will be so sensitive that they will be able to perform successful source counts in their high frequency spectral bands which will permit the removal of the brightest sources (including mainly SCUBA sources) from the resulting maps at lower frequency, decreasing the contribution of the Poisson noise to the power spectrum of the background. This procedure will be unable to affect significantly the correlation term, which arises mainly from the numerous low-flux sources.

I model here the sub-millimeter emission arising after violent starburst episodes, with large populations of young stars appearing on very short timescales (of the order of $10^7 - 10^8$ years). The level of the predicted correlated signal depends strongly on the assumptions about:

1. the escape fraction of UV radiation from merging star-forming galaxies and its evolution with redshift;

2. the properties of the dust emitting in the sub-millimeter band (its effective temperature at high redshift and the emissivity index β);

3. the redshift dependence of heavy elements and dust abundance;

4. the amount of gas inside merging haloes.

All these parameters are interconnected. Observations will give some hints about them and I will discuss the information that could be obtained by precise observations of the angular power spectrum at different frequencies.

The flexibility of this model in describing the population of merging star-forming objects gives me the possibility to extend it to other sources of foregrounds. As an example, I will discuss the effect of narrow line emission. The nucleosynthesis in the first generation of stars is able to produce significant amounts of carbon and oxygen already by redshift $z \sim 15 - 20$ (Heger & Woosley 2002; Yoshida et al. 2006). This brought my attention to the carbon

monoxide rotational lines originating from the star-forming haloes in the early universe. Recent observations show that these lines are very bright in the most distant quasars and radiogalaxies at redshift $z \sim 4$ (see e.g. Greve et al. 2005) and also in the star-forming galaxies in our vicinity (Gao et al. 2001; Weiß et al. 2005b; Bayet et al. 2006; Baan et al. 2008). They are also the brightest radio lines in our Galaxy (Wright et al. 1991; Fixsen et al. 1999).

I therefore compute the angular power spectrum of the foreground fluctuations due to emission in such lines from merging star-forming galaxies. The main difficulty of this task is related to the presence, at the same frequencies, of the continuum emission of dust discussed above. To separate the line contribution, I propose to make observations in several spectral bands with resolutions in the range $\Delta\nu/\nu_{\rm obs} = 10^{-1} - 10^{-3}$. I will demonstrate that with this technique it will be possible to increase significantly (over one order of magnitude) the amplitude of the signal due to the lines emission, while the contribution from other foregrounds generated by continuum emission (dust, radio sources, SZ effects in clusters of galaxies and the primordial fluctuations themselves) does not depend on the observing spectral resolution. Observations of the power spectrum of CO line emission with high spectral resolution permits to probe narrow slices of the universe at different redshifts, with a thickness $\Delta z/z \sim \Delta\nu/\nu_{\rm obs}$. Performing the computations for different spectral resolutions and proving the strength of this method, I recognized that an analogous approach is used in demonstrating the results of numerical simulations of the large scale structure of the universe. In that case the best contrast is achieved using slices with a very small thickness ($\sim$ 15 Mpc) compared to huge dimensions of the box ($\sim$ Gpc, Springel private communication). The observations in the CO lines can use comparable $\Delta\nu/\nu_{\rm obs}$ to increase the amplitude of the signal and to separate it from other continuum sources.

It is rather difficult, at present, to obtain a reliable theoretical estimate of the luminosity of different CO lines in the star-forming haloes (Silk & Spaans 1997; Combes et al. 1999; Greve & Sommer-Larsen 2008), and for this reason I shall use existing observational data to calibrate the model. I will consider local merging galaxies and luminous infrared galaxies, together with a sample of high-redshift sub-millimeter galaxies, observed at $z \sim 2-4$. Using such samples I calibrate the luminosity of the different lines on the star formation rate of the object, assuming a linear scaling. Using the merging model, which provides me with a statistical description of the distribution of the haloes as a function of their star formation rate, combined with these observational data, I can compute the power spectrum of angular fluctuations arising from the emission in the CO lines, at any frequency and for any spectral resolution. This technique

will allow one to measure the integrated properties of the population of weak star-forming merging galaxies in a broad redshift range: by calibrating with observational data obtained from different galaxy samples, one can describe the history of formation of giant molecular clouds and model the subsequent process of CO enrichment of the IGM throughout cosmic history.

The beauty and the strength of the proposed method of observing the angular fluctuations in the narrow line emission is connected with the fact that for a given line, at a fixed observing frequency, one detects the radiation from a slice of the universe with given Δz. The data on the cosmic star formation history (the aforementioned Madau plot) shows that the bulk of the star formation activity in the universe takes place in a very broad redshift range. Here I am considering the star-forming objects in the range $0 < z < 20$, corresponding to $\nu = 5 - 115$ GHz for the first CO transition. This is close to the WMAP and PLANCK LFI's detectors (Bennett et al. 2003; Bersanelli & Mandolesi 2000) and is accessible also for many ground-based experiments, like ALMA. Higher CO transitions are still bright upto ~ 350 GHz and are therefore interesting for the PLANCK HFI's bands (Lamarre et al. 2003), as well as for ACT and SPT. The same spectral band can cover different slices of the universe and I will show that the $10-40$ GHz region is the most interesting for the CO emission, because only the first two transitions contribute significantly to the angular fluctuations in this band. I will present, however, the frequency (and redshift) distribution for all the CO transitions upto $J = 7$, which will allow one to recognize which redshift range will give the main contribution to the signal.

According to the same model, I also compute the differential source counts curve for the emission in every line. The cumulated signal from many weak sources might contribute more to the power spectrum due to the clustering. Therefore, in addition to the simple Poisson fluctuations, I compute the correlation signal taking into account the regions of higher merging activity, corresponding to the positions where the future clusters and super-clusters of galaxies will appear.

From the same sample of objects that I used to calibrate the model, I found that the emission from the CN, HCN, HNC and HCO^+ molecules, with resonant frequency close to the CO ones (within $\sim 20\%$), do not add more than 10% to the amplitude of the CO signal (Baan et al. 2008). At higher frequencies, the dominant contribution comes from the CII line at 158 μm, while other atomic lines are much weaker. Here, however, I am interested not in the absolute luminosity of the lines, but in their ratio to the primordial fluctuations and to dust continuum emission in the same spectral band and with a given $\Delta\nu/\nu_{\rm obs}$. This argument makes the first two CO transitions more important

than the (more luminous) higher transitions, given their contribution to the power spectrum of angular fluctuations relative to the primordial CMB signal and to the foreground from extragalactic sources emitting in the sub-millimeter band due to the presence of large amounts of dust. The first CO transitions are usually saturated and their ratio follows the same Rayleigh-Jeans law of the CMB at low frequencies. At the same time, the dust particles have very low opacity at low frequencies and therefore their effect becomes weaker with decreasing frequency, compared with CO (1-0) and (2-1) transitions.

This model has a lot of uncertainties, which are not only related to the limitation of the extended Press-Schechter formalism in the estimate of the merging rate. The main one is connected to the value of the star formation rates in the selected sample. For the low redshift sample I used only the IRAS data, combined with the Kennicutt relation, to estimate $\dot{M}$. The galaxies in the high-redshift sample, on the other hand, often harbour an AGN and this is a further source of uncertainty in the estimate of $\dot{M}$. An additional difficulty derives from the different angular resolution of the CO and infrared observations.

I believe that the future observervations with different spectral resolutions will allow one to measure the predicted signal. In my view, it is important to develop a new method which will permit to directly measure the rate of enrichment of the universe with CO, not in the very rare and extremely bright objects (as QSO and radiogalaxies at $z \sim 4-6$), but in the most abundandant and less bright objects, which are not detected individually. The correlated signal which I have computed in this work and its dependence on the spectral resolution of the instrument provides a unique way to measure the contribution of the star-forming haloes at the different redshifts defined by the frequency of observations.

Throughout this thesis I will use the WMAP3 cosmological parameters for standard ΛCDM cosmology (Spergel et al. 2007).

2

A model for star formation and dust emission in merging haloes

To characterize the halo population I will use the standard Press-Schechter approach (Press & Schechter 1974) in the extended formulation of Lacey & Cole (1993), which also includes a prescription for the halo mergers.

2.1. Star formation from halo mergers

I model the star formation within the framework of the halo model and derive the star formation rate as the rate of the baryonic mass that is accreted per unit time into new haloes.

According to Lacey & Cole (1993), the merger rate of a halo of mass M_1 with another of mass M_2 in a final halo of mass $M = M_1 + M_2$ is given by

$$\begin{aligned}\frac{dN_{\rm merg}}{dMdt}(M_1 \rightarrow M, t) &= \sqrt{\frac{2}{\pi}}\frac{1}{t}\left|\frac{d\ln\delta_{\rm cr}}{d\ln t}\right|\left|\frac{d\sigma}{dM}\right|\frac{\delta_{\rm cr}}{\sigma(M)^2} \\ &\times \frac{1}{[1-\sigma(M)^2/\sigma(M_1)^2]^{3/2}} \\ &\times \exp\left[-\frac{\delta_{\rm cr}^2}{2}\left(\frac{1}{\sigma(M)^2}-\frac{1}{\sigma(M_1)^2}\right)\right], \qquad (2.1)\end{aligned}$$

where $\delta_{\rm cr}$ is the critical density for spherical collapse and $\sigma(M)^2$ is the variance of the linear density field (see Appendix C for details about how to compute these quantities). As pointed out by Benson et al. (2005), the merger model is consistent only if the ratio between the masses of the merging haloes is not larger than $\sim 10 - 100$. Therefore in the following analysis I will include only *major mergers*, i.e. such that $0.1 \lesssim M_1/M_2 \lesssim 10$.

In each merging episode a given amount of gas is converted into stars. It is necessary to take into account the cooling time which, for a given temperature T and metallicity Z, can be written as

$$t_{\rm cool}(T, Z) = \frac{3}{2} \frac{\rho_{\rm gas}\, kT}{\mu\, \Lambda(T, Z)\, n_{\rm H}^2}, \tag{2.2}$$

where $\Lambda(T, Z)$ is the cooling function (in units of erg cm^3 s^{-1}) and μ is the mean molecular weight of the gas. The temperature of the gas is assumed to be equal to the virial temperature. The cooling functions are tabulated for different values of T and Z by Sutherland & Dopita (1993). For my estimate of the cooling time I choose a value $Z = Z_\odot$: observations of quasars and galaxies at $z \sim 6$ by Fan (2006) show that the metal content of such objects is close to the solar value, therefore this approximation is valid at least to this redshift. For even more distant objects the value of the metallicity is expected to be lower, but I will show that such objects will not contribute significantly to the effects that I am aiming to model. The cooling time sets a limit for the star formation, since only haloes with $t_{\rm cool} \leq t_{\rm Hub}$ can cool within the cosmological time. This excludes the very massive haloes and the haloes with a mass corresponding to a virial temperature lower than $T_{\rm vir} \simeq 10^4$ K.

Let us now consider two haloes of mass M_1 and M_2, merging to yield a halo of mass $M = M_1 + M_2$. In each episode a given amount of the halo mass is converted into stellar mass. I parametrize this in the following way

$$M_\star^1 = \frac{\Omega_{\rm b}}{\Omega_{\rm m}}\, \eta\, M_1 \frac{M_2}{M/2}. \tag{2.3}$$

The amount of stellar mass formed from the halo M_1 is therefore proportional to its mass and to the mass of the merging halo M_2, if this is sufficiently massive. In the same way, for the second halo

$$M_\star^2 = \frac{\Omega_{\rm b}}{\Omega_{\rm m}}\, \eta\, M_2 \frac{M_1}{M/2}. \tag{2.4}$$

The total stellar mass produced in this merging episode is then the sum

$$M_\star = M_\star^1 + M_\star^2 = 4\, \frac{\Omega_{\rm b}}{\Omega_{\rm m}}\, \eta\, \frac{M_1 \cdot M_2}{M}. \tag{2.5}$$

The parameter η is the star formation efficiency. I take this to be 5%, in order to match the observations of the cosmic star formation history, which will be presented in Section 3.3.
Using this simple parametrization I am able to derive the stellar mass produced in a merger process between two haloes of given mass.

2.2. Lifetime of the starburst phase

The approach described above allows me to compute the stellar mass produced in each merger episode. Since I am interested in deriving the rate at which gas is converted into stars and then connecting it to the luminosity of the sources, I introduce a characteristic timescale for star formation.

Several numerical simulations of merging disk galaxies (Mihos & Hernquist 1994, 1996; Springel & Hernquist 2005; Robertson et al. 2006) show that the star formation process that occurs during a merger consists of multiple starburst episodes. Tidal interactions between merging galaxies can trigger star formation in the two disks before the final coalescence, although this usually coincides with the strongest burst. An accurate analytical description of such a process is complicated and thus numerical techniques must be used to find a solution. In the following, I will introduce a phenomenological prescription for the star formation in the merging haloes, based on the results of the numerical simulations mentioned above. These works studied the merging of two equal mass gas-rich galaxies and predicted an evolution of the star formation rate with time characterized by several phases, as displayed in Figure 2.1:

1. a long underlying phase (red), with a low and constant star formation rate, which is independent of the major merging process and is the sum of the quiescent star formation rates in each disk prior to the encounter;

2. a second, more active phase (green), which corresponds to the first close passage of one galaxy around the other, when the tidal deformation experienced by each disk creates shocks and compression of the gas. This triggers a moderate burst of activity of about 200 $M_{\odot}$/yr, with a duration of the order of 3×10^8 years;

3. a strong starburst phase (blue), which occurs when the two galaxies finally merge, with a star formation rate higher than 600 $M_{\odot}$/yr over a very short timescale, lower than 10^8 years.

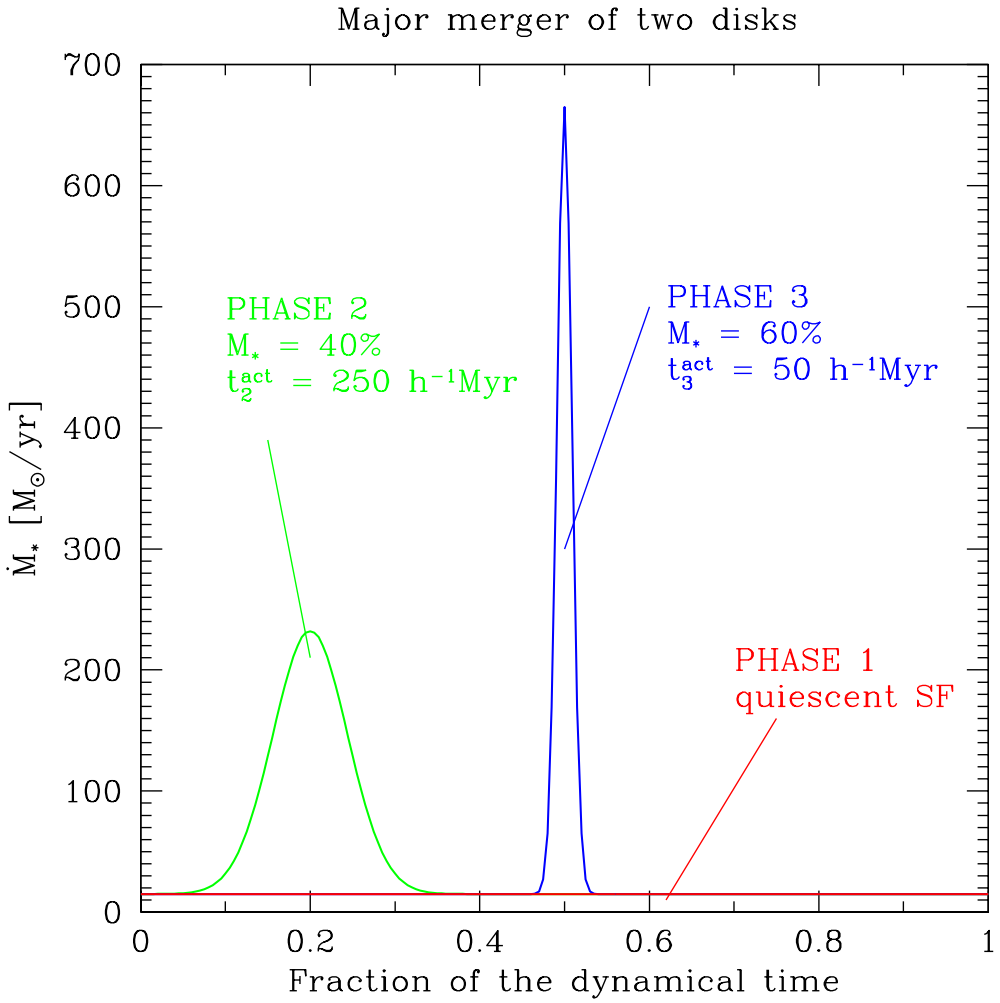

Figure 2.1: The star formation rate as a function of time during a merger of two gas-rich massive disk galaxies of equal mass ($M \simeq 10^{12}\, h^{-1} M_{\odot}$) used for the computations in this work and based on the results of numerical simulations, cited in the text. Different colours identify different phases of star formation activity.

I will take this model to be representative of the star formation process during mergers of massive gas-rich objects. The bulk of the objects that contribute to the merging activity are at rather high redshift ($z \gtrsim 0.3 - 0.5$), where the fraction of spirals and irregulars is higher than in our vicinity, where ellipticals

are already a significant part of the total.

As we have seen in Section 2.1, each merger between two haloes M_1 and M_2 produces a certain amount of stellar mass $M_\star(M_1, M, z)$. Such stellar mass will be created in the two active phases identified in Figure 2.1 in green and blue, according to the parameters summarized in the same plot. The first phase does not involve the stellar mass produced by the merger and hence will not be included in the model. Nevertheless, in Section 4.2.1 I will estimate the contribution of this stage to the correlation term of the angular power spectrum.

I therefore have $M_\star = M_\star^{(2)} + M_\star^{(3)}$, with $M_\star^{(2)} = 0.40\, M_\star$ and $M_\star^{(3)} = 0.60\, M_\star$. The percentages of stellar mass formed in each event are based on an average of the results presented in the literature and mentioned at the beginning of this section.

Introducing the active time of each phase, $t_{\rm act}^{(i)}$, it is easy to derive the corresponding star formation rate

$$\dot{M}_\star^{(i)} = \frac{M_\star^{(i)}}{t_{\rm act}^{(i)}}, \qquad i = 2, 3. \tag{2.6}$$

where $t_{\rm act}^{(2)} = 2.5 \times 10^8\, h^{-1}$yr and $t_{\rm act}^{(3)} = 5 \times 10^7\, h^{-1}$yr.

2.3. Infrared luminosity of the haloes

The star formation rate given in (2.6) is strongly correlated with the infrared luminosity of the source, through the Kennicutt relation (Kennicutt 1998)

$$\dot{M}_\star\, [M_\odot/{\rm yr}] = 1.71 \times 10^{-10}\, L_{\rm IR}\, [L_\odot], \tag{2.7}$$

where IR indicates the $[8 - 1000]$ μm band. The bulk of emission in this band peaks at about 100 μm and around 80% of it is due to low temperature dust (Lagache et al. 2005). Therefore in my estimate I can directly use this relation and apply it to obtain the luminosity due to low temperature dust in star-forming galaxies.

The number density of such bright objects for each population can be derived with the aforementioned model as

$$\frac{dN_{\rm bright}^{(i)}}{dV}(\dot{M}_\star, z) = \frac{dN_{\rm merg}}{dV\,dt}(M, z) \cdot t_{\rm act}^{(i)}, \tag{2.8}$$

where $\frac{dN_{\rm merg}}{dV\,dt}(M_1, M, z)$ is the number density of mergers per unit time, which can be obtained weighting Equation (2.1) over the mass function of the merging

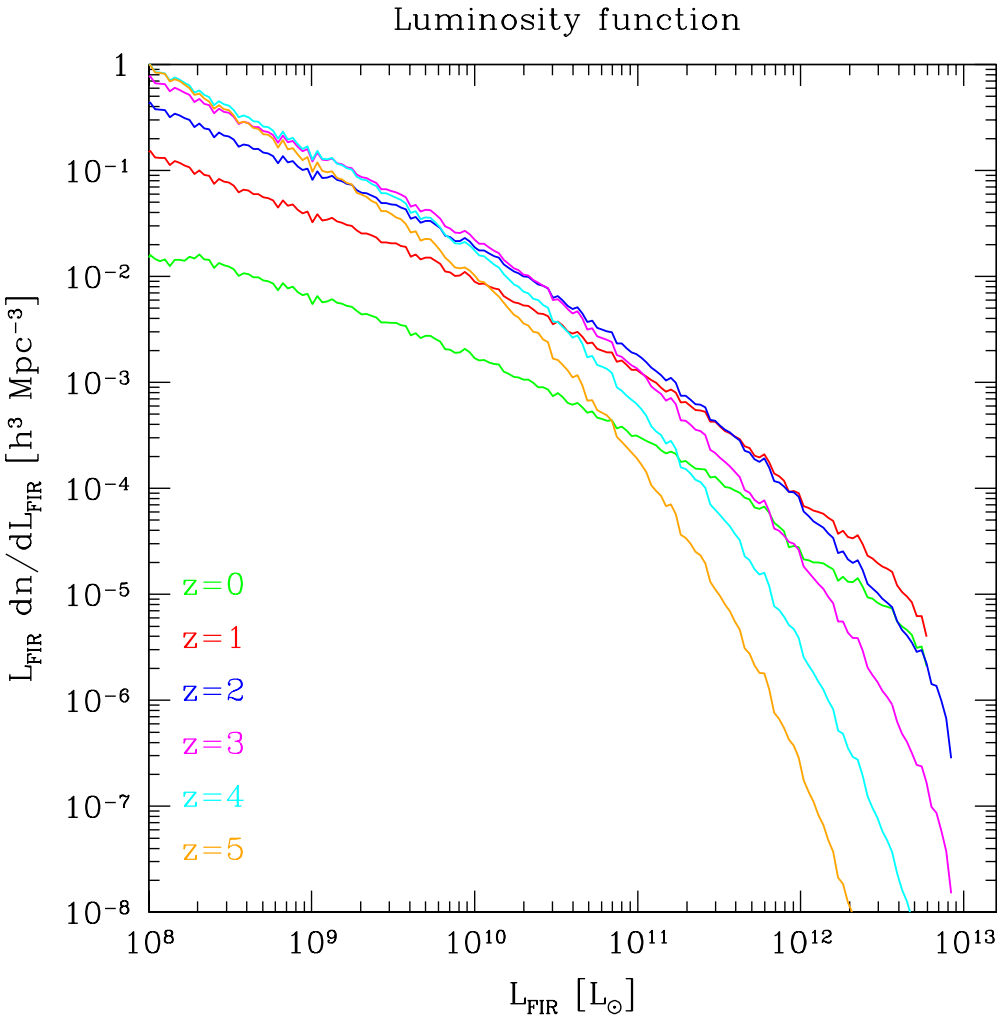

Figure 2.2: The shape of the far-infrared luminosity function of the merging haloes at different redshifts.

haloes

$$\frac{dN_{\rm merg}}{dV\,dt}(M,z) = \int dM_1 \int dM \frac{dn}{dM_1}\frac{dN_{\rm merg}}{dM\,dt}, \tag{2.9}$$

remembering that $M = M_1 + M_2$ and that $\dot{M}_\star$ depends on both the masses of the merging haloes.
The total number of bright objects at a given redshift will then be obtained by

summing over the populations

$$\frac{dN_{\rm bright}}{dV}(\dot{M}_\star, z) = \frac{dN^{(2)}_{\rm bright}}{dV}(\dot{M}_\star, z) + \frac{dN^{(3)}_{\rm bright}}{dV}(\dot{M}_\star, z). \tag{2.10}$$

Equation (2.10) is a differential number density of bright objects in the universe. This is a crucial quantity, especially if $\dot{M}_\star$ is replaced by the infrared luminosity by taking advantage of the Kennicutt relation. In this way I obtain a statistical determination of the sources responsible for dust emission, i.e. a luminosity function for these objects, which is shown in Figure 2.2. The sharp cutoff at $L_{\rm IR} \simeq 10^{13}\, L_\odot$ is due to the cooling time, which prevents the formation of the most massive (most luminous) objects.

2.4. A model for dust emission

A significant fraction of the stellar radiation emitted by galaxies is reprocessed by dust and reradiated in the infrared and sub-millimeter band. The dust in star-forming galaxies has a very complicated distribution in space and a broad range of temperatures, depending on the proximity of dust grains to the sources of ionizing, optical and short-wavelength infrared radiation. The emissivity of the dust depends strongly on its composition and on the size distribution of grains. There are no enough observational data to construct a reliable detailed model connecting the sub-millimeter spectra of the galaxies at redshift $z > 2$ with the star formation inside them. Several observations (Blain 1999; Blain et al. 2002; Chapman et al. 2005) show that in the majority of the brightest extragalactic infrared objects and in particular in SCUBA galaxies, the observed spectrum in the $100-3000$ μm band is well fitted by a single-temperature modified blackbody $\nu^\beta B_\nu(T_{\rm dust})$ with a temperature $T_{\rm dust} \simeq 30 - 50$ K and an emissivity index in the range $1 \leq \beta \leq 2$; there is little change in the properties of dust along the Hubble sequence, thus I expect this fit to be valid independently of the Hubble type. As it is obvious from the discussions in the papers of Reach et al. (1995) and Schlegel et al. (1998), a fit with β significantly smaller than 2 is attributable to multi-temperature dust or a difference in chemical composition.

For galaxies at high-redshift having similar rates of dust heating, the increase in the temperature of the cosmic microwave background will affect the dust temperature. Therefore if the dust temperature in an object at $z = 0$ is $T_{\rm dust}$,

for a similar object at redshift z it would increase as (Blain 1999)

$$T_{\rm dust}(z) = \left[T_{\rm dust}^{4+\beta} + T_{\rm cmb}^{4+\beta}\left((1+z)^{4+\beta} - 1\right)\right]^{1/(4+\beta)}, \tag{2.11}$$

where $T_{\rm cmb} = 2.725$ K is the temperature of the background today.

I will consider the observations by PLANCK, SPT and ACT at fixed frequencies, namely 147, 217, 274 and 353 GHz; the peak of the SED for the majority of the brightest SCUBA and infrared galaxies is around 3000 GHz. This means that the frequencies higher than the peak will begin to dominate these observing channels at redshifts $z \gtrsim 19$, 13, 10 and 8, respectively, so the flux observed in a given band will correspond to the flux emitted at a frequency higher than the peak. This has two consequencies. First, the contribution from high redshift objects will begin to decrease in the highest frequency bands of PLANCK, ACT and SPT. But in moderate frequency channels (147 and 217 GHz) these experiments continue to be sensitive to the first merging galaxies in the universe. Furthermore, for the high frequency channels the approximation of hot single-temperature dust emission will not be accurate, since in observations of the local bright objects the region of wavelengths shorter than 100 μm shows that the decline in flux has a power-law behaviour, rather than the exponential cutoff of the single-temperature model. This demonstrates that the dust in reality has a broad distribution of temperatures which makes the cutoff after the peak much less steep.

2.4.1. Dust emission in the CMB thermal bath at high redshift

The fit by a modified blackbody spectrum considered above is valid under the further assumption that the influence of the CMB radiation field on dust grains can be neglected. Such an approximation is good at low redshift, when the background temperature is low, but as the redshift increases the intensity of this radiation becomes non-negligible. Therefore it is necessary to introduce a correction in the assumed spectral energy distribution of infrared sources

$$L_\nu \propto \nu^\beta \left[B_\nu(T_{\rm dust}) - B_\nu(T_{\rm cmb})\right], \tag{2.12}$$

where the difference in square brackets represents the correction due to the presence of the CMB thermal bath. In the low frequency limit ($h\nu \ll kT_{\rm dust}$) the luminosity is proportional to the difference between the grain temperature and the temperature of the CMB. As a result, for the same optical and ultraviolet energy absorbed by the grain, its radiation in the high frequency band

will increase due to the existence of the CMB thermal bath and correspondingly will decrease in the low frequency part of the spectrum. This is plotted in Figure 2.3 for an object at $z = 10$ with infrared luminosity $L_{\rm IR} = 10^{10} L_{\odot}$.

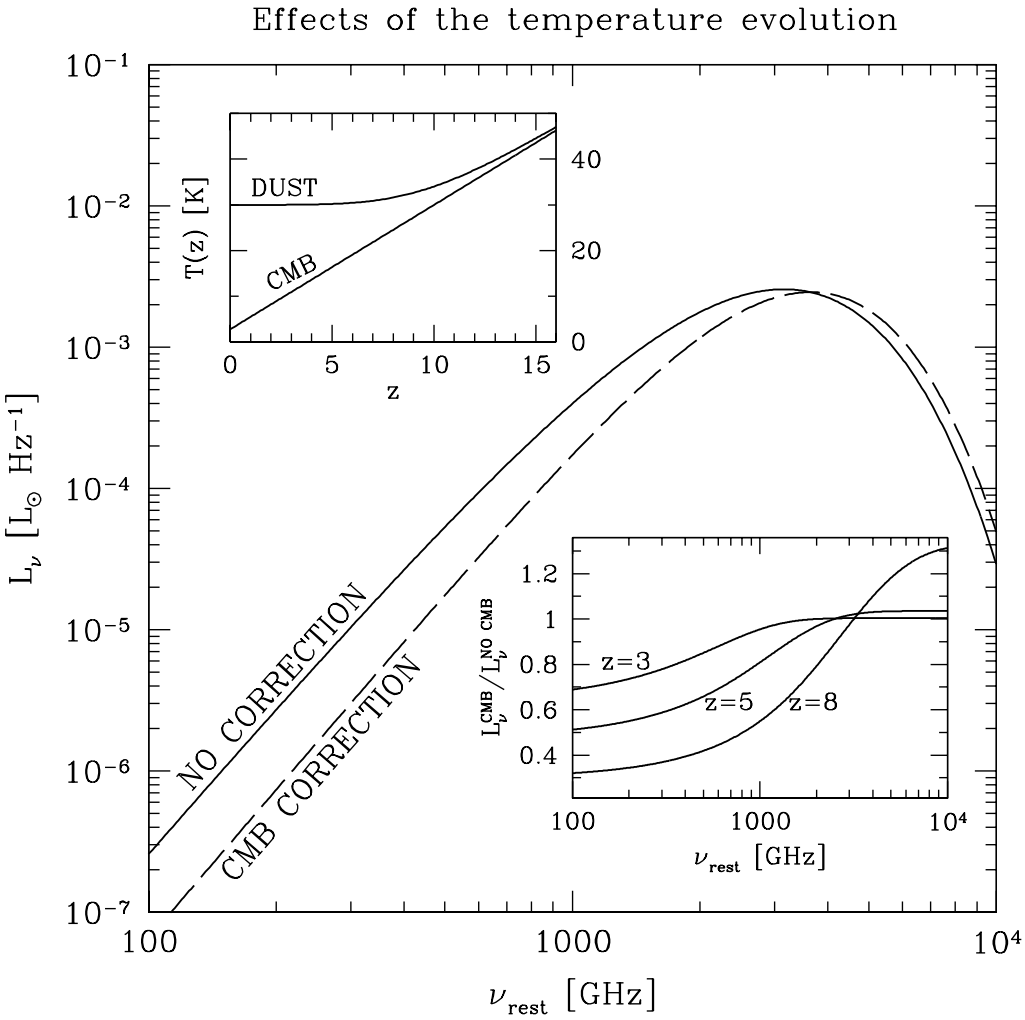

Figure 2.3: The effect of the correction in Equation (2.12) on the spectrum of star forming haloes at $z = 10$: the solid line is the spectrum with dust greybody only, the dashed line is the spectrum when including the correction due to the CMB. In the bottom insert the ratio between the two spectra at differrent redshifts is displayed to stress the importance of the correction with increasing redshift. The top insert shows the dust and CMB temperature evolution according to Equation (2.11).

3
Three observational tests

I identified the merger formalism presented in the previous chapter as the main process leading to star formation in galaxies. Within the framework provided by the standard ΛCMD Cosmology, this approach constitutes a model for the IR emission in the Universe that can be compared with three different observational constraints, as I show below.

The model is particularly sensitive to the two spectral parameters, the emissivity index β and the temperature $T_{\rm dust}$ of dust, which convert the bolometric luminosity into the spectral luminosity and hence fix the distribution of the infrared sources. Another important quantity, which will be discussed in this section, is the escape fraction of ionizing photons, which determines the fraction of ultraviolet radiation absorbed by dust and hence sets the relation between the star formation rate and the infrared luminosity. I will explain that the introduction of such a parameter is necessary to satisfy the limits on the intensity of the infrared background set by the COBE-FIRAS data. Several observational tests can be performed to calibrate the free parameters of the model.

3.1. SCUBA source counts

The merging halo model provides the source counts for the sub-millimeter sources. Comparison of my counts with SCUBA observations (Coppin et al.

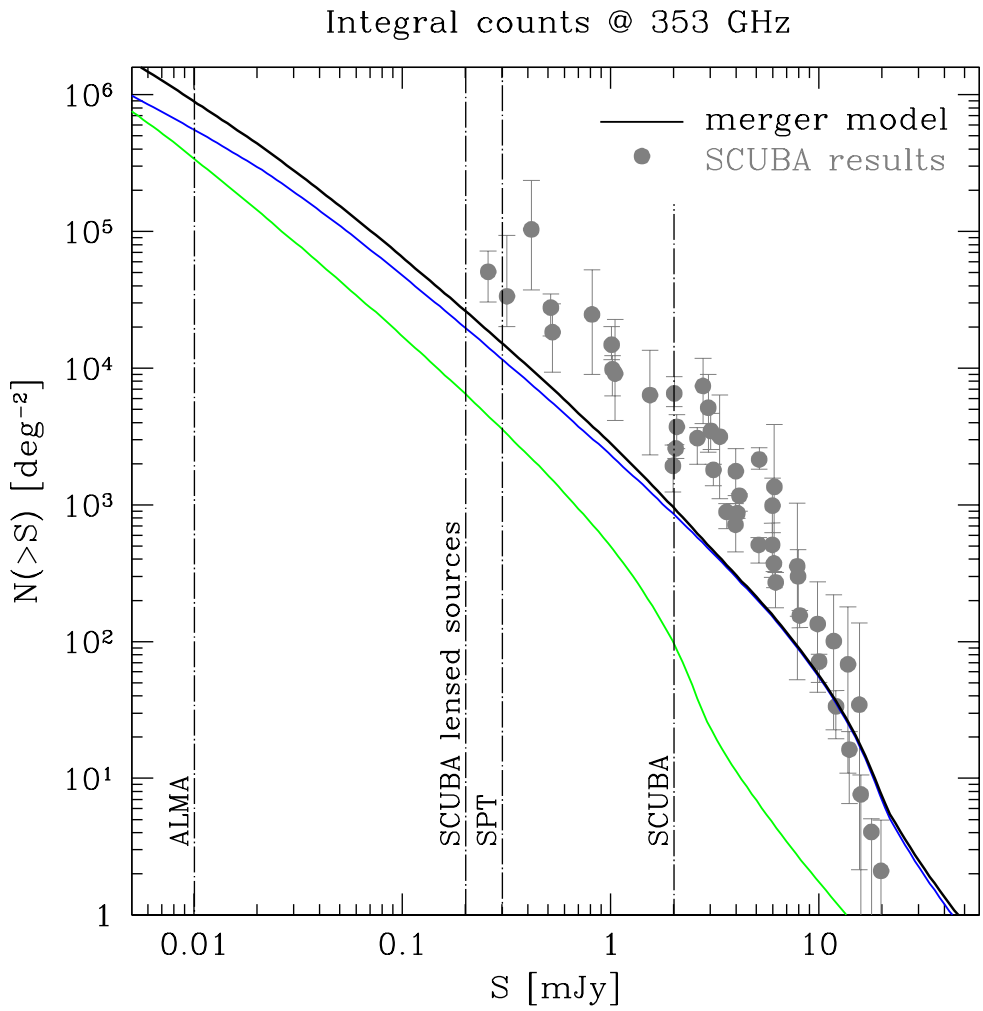

Figure 3.1: The integral counts predicted by the model (black solid line) at 353 GHz (850 μm), compared with the compilation of Coppin et al. (2006) for SCUBA sources (dots). The vertical lines represents the sensitivity limits of SCUBA (Coppin et al. 2006; Knudsen et al. 2006), SPT and ALMA (expected in $\sim$ 3 hours integration; Ruhl et al. 2004; Tarenghi & Wilson 2005). Different colours refer to the populations generated by the two bursts of star formation, as shown in Figure 2.1 (green and blue). I assume $T_{\rm dust} = 30$ K (with the CMB correction discussed in Section 2.4.1), $\beta = 1.5$ and a mass-dependent escape fraction, which will be discussed in Section 3.2.1.

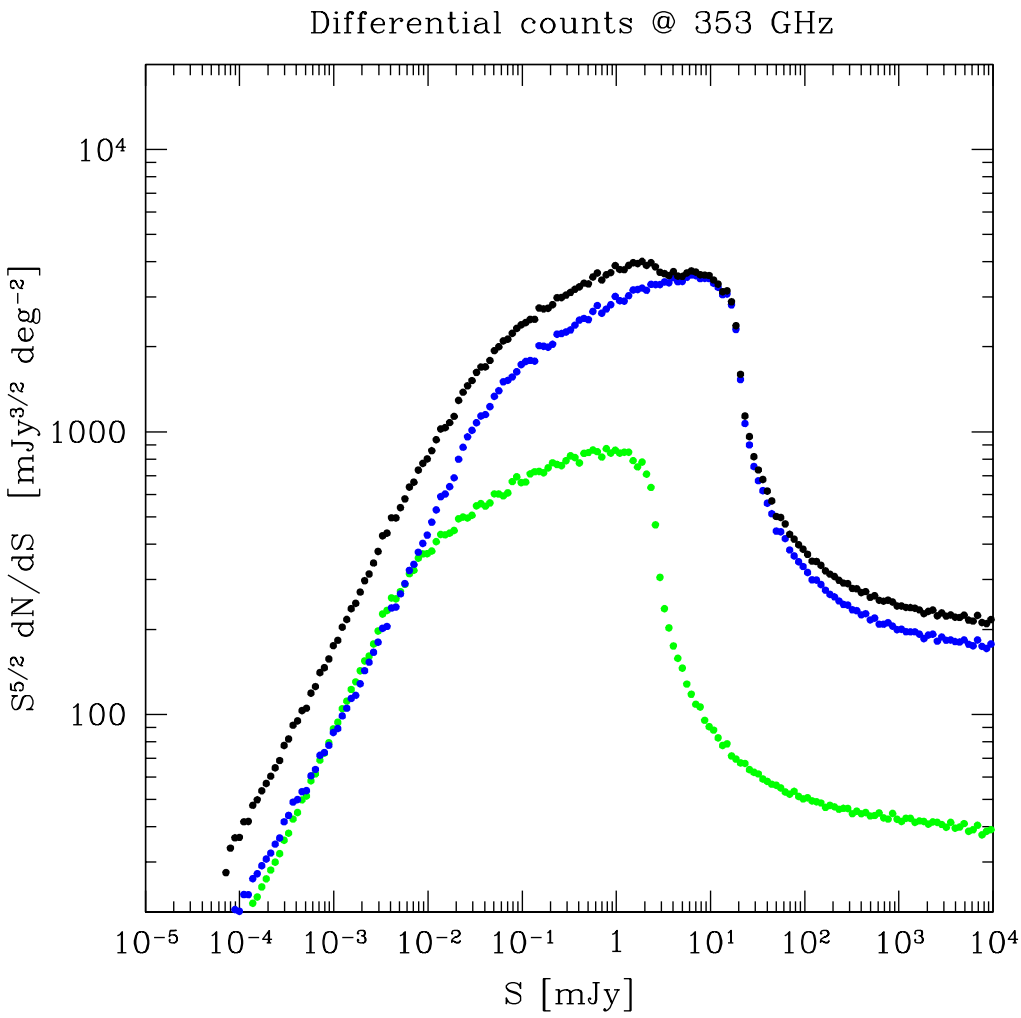

Figure 3.2: The same as in Figure 3.1, but for the differential counts at 353 GHz. The short active phase (blue) is the most important and dominates the source counts at the high-flux limit. At the low fluxes the contribution from the two bursts is pratically equal.

2006) at 850 μm (353 GHz) shows that, in the region above the SCUBA sensitivity limit at 0.2 mJy, the curve is rather sensitive to the dust emission spectral parameters. In Figure 3.1 I plot the integral source counts resulting from the model. I will show in Section 4.3.1 the variation of the curves for different values of the temperature and emissivity index: the closest result to the SCUBA

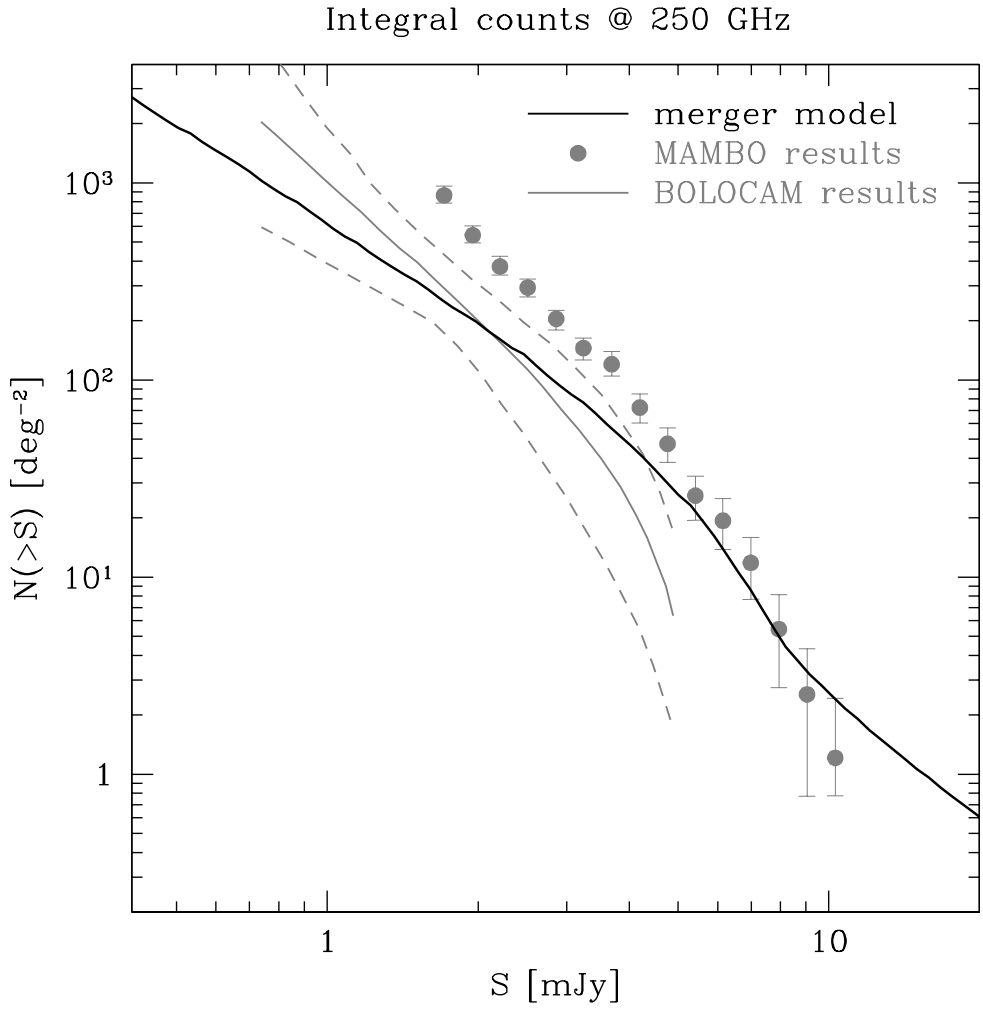

Figure 3.3: The integral counts predicted by the merging model at 250 GHz compared with the results of MAMBO (Bertoldi et al. 2007) and BOLOCAM (Laurent et al. 2005) at the same frequency. The points for BOLOCAM, originally presented at 1.1 mm (273 GHz), have been rescaled to 250 GHz.

counts is obtained for $T_{\rm dust} = 30$ K and $\beta = 1.5$. These spectral parameters are consistent with those found from the observations both in the local (Dunne & Eales 2001) and in the high redshift universe (Chapman et al. 2005), so I will use them hereafter.

Figure 3.2 shows the differential source counts predicted by the model. As in

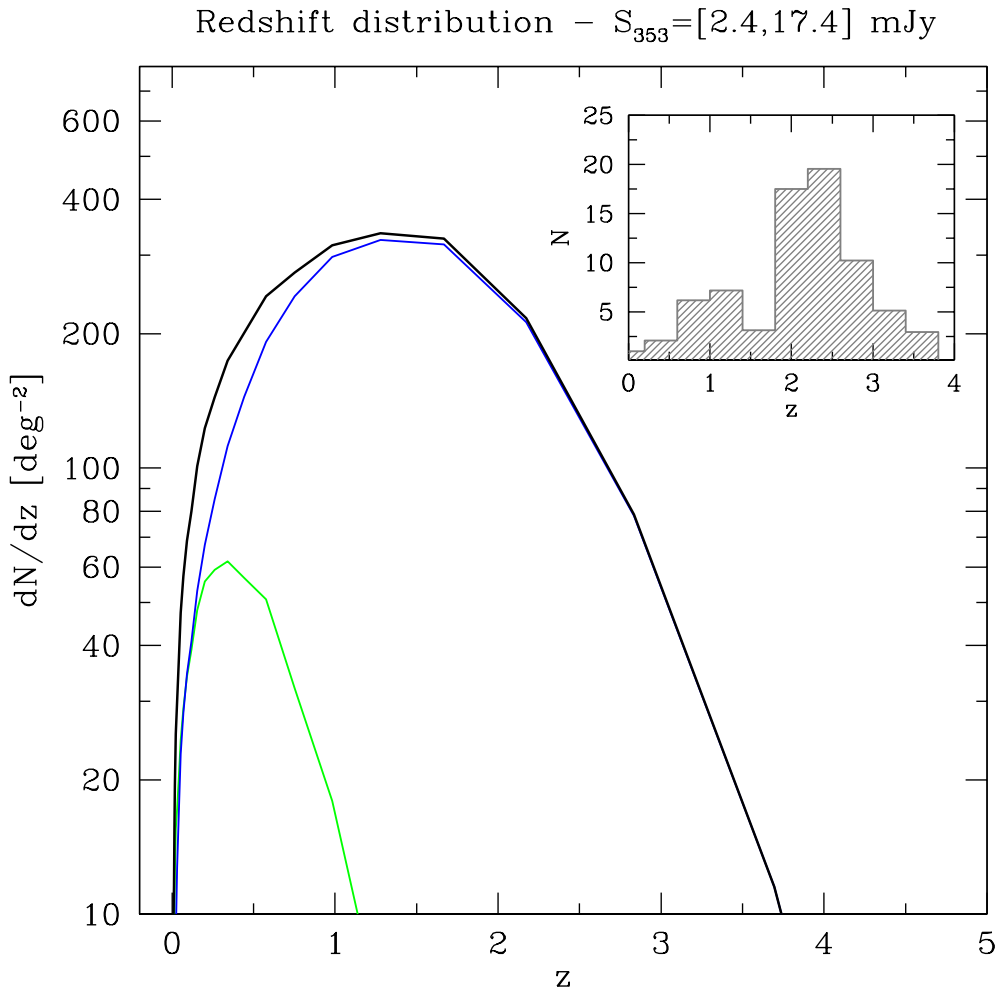

Figure 3.4: The redshift distribution of the sources at 353 GHz according to the model (solid line) for the same flux range of Chapman et al. (2005) and compared with their sample in the insert. Green and blue curves represent, as in Figure 3.1, the contribution of the two star formation phases: also in this case the short phase is dominating and can be detected at much higher redshift.

the plot of integral counts, I show in different colours the contributions of the two active phases of star formation, presented in Figure 2.1. From these plots, it is evident that the short burst phase (blue) dominates the number counts,

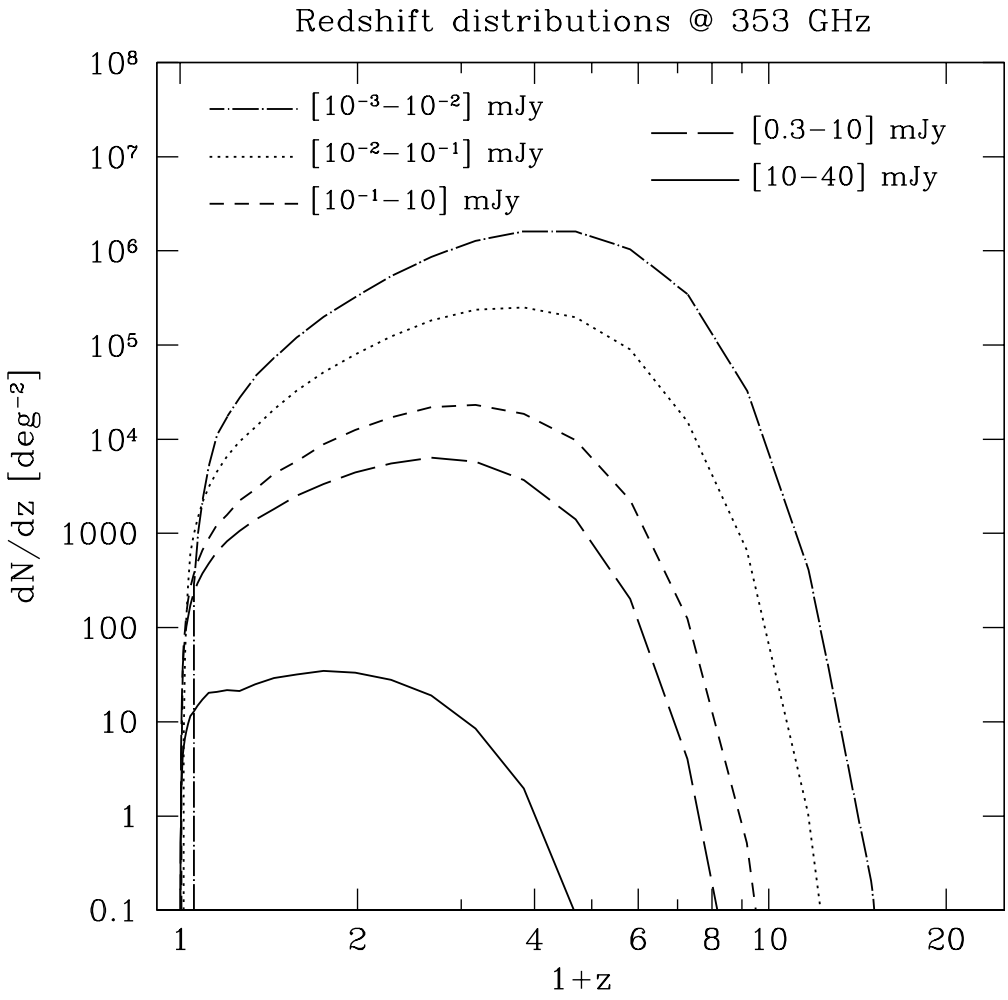

Figure 3.5: The redshift distribution of the sources at the same frequency for different flux ranges: the $[0.3-10]$ mJy interval (long-dashed line) could be relevant for SPT observations, the sources in the range $[10^{-2}-10^{-1}]$ mJy (dotted line) contributes 30% of the sub-millimeter background intensity at 353 GHz.

in particular at the highest fluxes, since it involves a comparable amount of stellar mass over a much shorter characteristic time. The rapid decrease of the differential counts curve in the range $[10-40]$ mJy reflects the rapid change in the merging rate occuring at $z \gtrsim 0.7$ and possibly has the same nature as the

rapid cosmological evolution of AGN.

As an additional test of these fits, I plot the distribution of the sources with redshift. In Figure 3.4 I compare with the observations of Chapman et al. (2005), in the same flux range $[2.4 - 17.4]$ mJy at 353 GHz. The two distributions are significantly different, in particular my model predicts a peak around $z \sim 1.5$ while optical identifications of SCUBA sources give a peak at $z \sim 2.5$. This is an intrinsic limitation of the merging models, which predicts the formation of the most massive (and thus brightest) objects at redshifts lower than the redshift range of SCUBA sources. The short burst phase (blue line in the plot) plays the most important role, since it allows the detection of bright sources at much greater distances. Figure 3.5 shows several redshift distributions at the same frequency, for different flux ranges.

Note, however, that the source number counts predicted by the model are slightly biased downwards when compared with SCUBA low flux data inferred from lensing measurements. I have found that, for the small sky area surveyed by SCUBA and the typical angular correlation scales for sub-millimeter sources, the source counts should show a typical dispersion much greater than the Poissonian estimate. In particular, I have found that typical fluctuations of the order of $20 - 25\%$ of the *real* underlying number source count should be given when trying to estimate this quantity in areas comparable to that covered by SCUBA.

Observations and source counts in the submillimeter band have been also obtained by the MAMBO (Bertoldi et al. 2007) and BOLOCAM (Laurent et al. 2005) teams at 1.2 mm (250 GHz) and 1.1 mm (273 GHz), respectively. I compared their data with our predictions in Figure 3.3: I rescaled the BOLOCAM points to 250 GHz using the greybody spectrum described in Section 2.4. The total sky area covered by these two instruments is comparable to that of SCUBA. The data of these three experiments are all consistent with each other.

Most of the present and future experiments have a limited angular resolution (around 1 arcmin), which will not permit the resolution of two merging galaxies. The characteristic physical separation of two objects at their first passage is of the order of 100 kpc (corresponding to 12 arcsec at $z \sim 2$) and of 10 kpc during the final coalescence (1.2 arcsec). But the impressive sensitivity and angular resolution of ALMA, which is expected to reach a value lower than 1 arcsec in the frequency bands discussed here (Tarenghi & Wilson 2005), should enable both the identification of merging galaxies as double or asymmetric sources and the distinction between the two phases of star formation activity. Furthermore, ALMA will be able to demonstrate the difference between the typical merging starburst activity and the strong nuclear brightening due to the presence of a

hidden AGN.

3.2. Intensity of the cosmic infrared background

Another test that can be performed to calibrate this model is to compute the mean brightness of the cosmic infrared background (CIB) due to the point sources and to compare it with the observations at the same frequency. Fixsen et al. (1998), on the basis of the observations with COBE-FIRAS, presented the following fit for the intensity of the far-infrared background in the spectral range $[150 - 2400]$ GHz

$$I_\nu^{\rm CIB} = (1.3 \pm 0.4) \times 10^{-5} (\nu/\nu_0)^{0.64 \pm 0.12} B_\nu (18.5 \pm 1.2 \text{ K}), \tag{3.1}$$

where B_ν is the Planck function and ν_0 corresponds to $100\,\mu$m.
In the model I estimate the contribution of merging galaxies to the infrared background integrating the source counts over the flux

$$I_\nu^{\rm CIB} = \int S_\nu \frac{dN}{dS_\nu} dS_\nu. \tag{3.2}$$

The model predicts a large number of sources even at very small fluxes ($S_{353} \sim 10^{-5}$ mJy) and the slope of the differential counts in the range $[10^{-3} - 10^{-5}]$ mJy is so steep that these sources do not contribute much to the infrared background intensity. The bulk of it comes from the sources with flux in the range $[10^{-2} - 10]$ mJy. However this is strongly related to the assumed value of the escape fraction of photons which strongly diminishes the contribution of less massive objects.

3.2.1. Escape fraction

There is a natural process that decreases the contribution of star-forming galaxies to the intensity of the sub-millimeter background, namely the escape fraction of ionizing photons. Dust inside the haloes absorbs UV and optical photons and then re-emits them in the infrared band. However, assuming that all the ionizing radiation produced inside the galaxies is absorbed by the medium (i.e. by dust), so that the escape fraction is close to zero, is not completely correct, expecially for less massive objects, for which the escape fraction could be greater than zero.
I model the escape fraction as a function of the halo mass

$$f_{\rm esc}(M) = 0.8\, e^{-M/M_{\rm s}}, \tag{3.3}$$

where $M_{\rm s}$ is the scaling mass, allowing an escape fraction of up to 80% for small-mass objects. To satisfy the limits imposed by the intensity of the infrared background a value $M_{\rm s} = 10^{10}\,h^{-1}M_{\odot}$ is required.

The idea of a mass-dependent escape fraction was used in the works of Ricotti & Shull (2000) and Kitayama et al. (2004), which dealt with the reionization of the universe. Here I am more concerned with the presence of dust which absorbs ultraviolet photons and then influences the calibration of the Kennicutt relation, which assumes that almost all photons produced by young stars are absorbed by dust and re-emitted in the infrared band. In this sense, I need to compare the infrared and ultraviolet luminosities of observed galaxies to derive an estimate of the escape fraction in these objects.
For example, very recent observations by Buat et al. (2007) using SPITZER and GALEX allow us to estimate an escape fraction of the order of $1 - 2\%$ for bright galaxies in the local universe. A very tight correlation between the $L_{\rm TIR}/L_{\rm FUV}$ ratio[1] and metallicity has been found by Cortese et al. (2006) in a sample of nearby normal star-forming galaxies: the infrared to ultraviolet ratio increases with metallicity, thus leading to a higher escape fraction for low metallicity objects. Earlier observations by Heckman et al. (1998) seem to confirm this trend even for starburst galaxies, with escape fractions of the order of $30 - 50\%$ for very metal poor objects. The metallicity is also known to correlate very well with stellar mass, as shown by Tremonti et al. (2004) and Erb et al. (2006) for the local and the high-redshift universe, respectively. In the merger model presented here stellar mass inside every halo is directly related to the mass of the halo itself. Then it is natural to expect a higher metallicity in more massive systems and therefore also a lower escape fraction. These simple arguments demonstrate that modelling this quantity as a function of mass is, at least qualitatively, well justified.

As mentioned before, the Kennicutt relation implicitly assumes that almost all the ultraviolet photons produced by young stars are absorbed and reradiated by dust in the infrared, i.e. that $f_{\rm esc} = 0$. When considering non-zero values of $f_{\rm esc}$, I need to introduce a correction in the Kennicutt relation

$$\dot{M}_{\star}\,[M_{\odot}/{\rm yr}] = \frac{1.71 \times 10^{-10}}{1 - f_{\rm esc}}\,L_{\rm IR}\,[L_{\odot}]. \tag{3.4}$$

In this way, less massive objects are unable to retain all their ionizing radiation, dust absorption will be less efficient and this results in a lower infrared luminosity for a given star formation rate. I will return to this point in Section 4.3.3, discussing several alternative parametrizations and their effect on

[1] TIR indicates the $[1 - 1000]$ μm band

the CMB fluctuations.
As shown in Figure 3.6, with such a correction, the model prediction for the intensity of the cosmic infrared background is within the 1σ limits of the fit in Equation (3.1). On the other hand, with an escape fraction independent of mass and redshift and close to the 2% value of Buat et al. (2007), our model predicts an intensity for the sub-millimeter background which exceeds the COBE-FIRAS value but remains within the 2σ errorbars.

About 30% of the background intensity at 353 GHz comes from sources in the flux range $S_{353} = [0.01 - 0.1]$ mJy. The redshift distribution of such sources is displayed by the dotted line in Figure 3.5 and it is characterized by a broad peak around $z \simeq 2.5 - 3$.

3.3. The Madau plot for cosmic star formation history

The very simple parametrization which I use to model the star formation process within the framework of the halo model can be verified computing the cosmic star formation density as a function of redshift (i.e. the *Madau plot*, Madau et al. 1996, 1998; Hopkins 2004; Hopkins & Beacom 2006) and comparing it with the observations.

I average the star formation rate over all haloes M_1 which are merging with other haloes to produce a final mass M

$$\dot{\rho}_\star(z) = \int dM_1 \int dM \frac{dN_{\rm merg}}{dMdt} \frac{dn}{dM_1} M_\star(M_1, M_2, z), \tag{3.5}$$

where $\frac{dN_{\rm merg}}{dMdt}$ is defined in Equation (2.1) and $M_\star(M_1, M_2, z)$ is the number of stars produced in each merger episode.

The evolution of cosmic star formation rate density is compared with recent observations, obtained at different wavelengths, in Figure 3.7. It is clear that my model slightly overestimates the cosmic star formation rate, especially at higher redshift ($z \gtrsim 5$), where my points are outside the observational errorbars. This could be due again to the limitations of the merging model which, though very accurate at the lower redshifts, fails to reproduce the merger trees at high redshift.

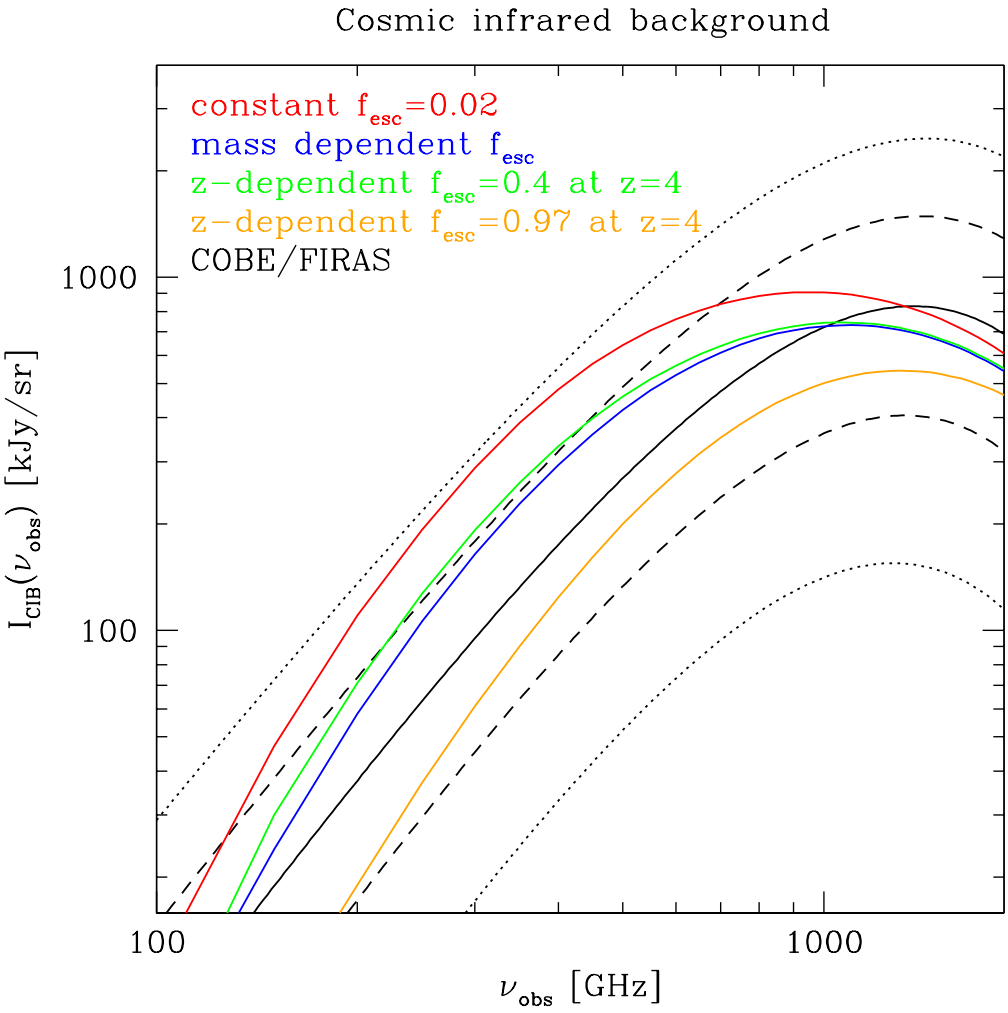

Figure 3.6: The spectrum of the cosmic infrared background predicted by our model with a mass-dependent escape fraction (blue), Equation (3.3), compared with the fit to the COBE-FIRAS observations (black) by Fixsen et al. (1998), Equation (3.1): dashed and dotted lines are the $\pm 1\sigma$ and $\pm 2\sigma$ uncertainty levels, respectively. Red, green and orange lines corresponds to three alternative parametrizations for the escape fraction, see Section 4.3.3 for details.

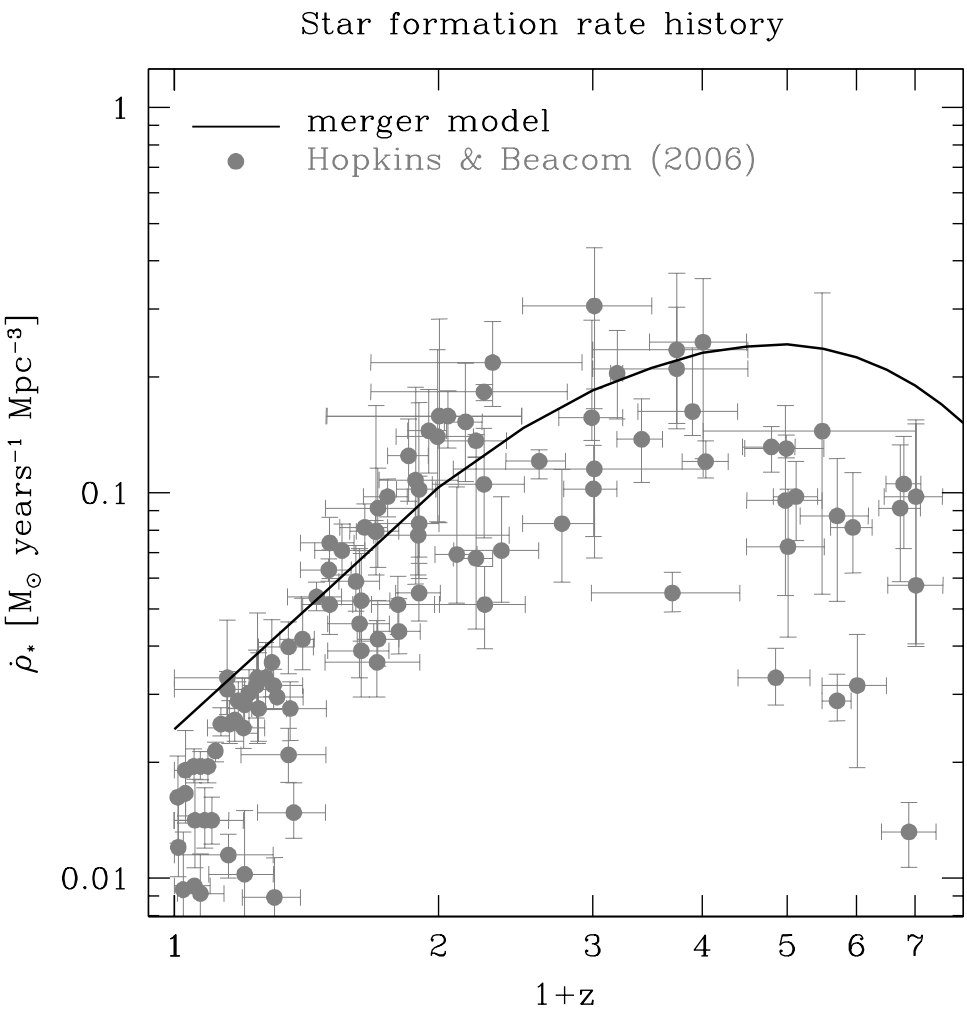

Figure 3.7: The evolution of the star formation rate according to the merger model (solid line), compared with the compilation of Hopkins & Beacom (2006) of numerous observations at different wavelengths (dots).

4

Dust emission as CMB foreground

Using a compromise model that is consistent with the measurements of the cosmic star formation rate that does not exceed the SCUBA number counts and that is close to the 1σ limit of the sub-millimeter background provided by COBE-FIRAS, I can make predictions for the fluctuations in the CMB connected with the foreground sub-millimeter emission from star forming galaxies.

4.1. Angular fluctuations from the star-forming objects

The angular distribution of the emission of these star-forming sources will be characterised by their spatial distribution at different cosmic epochs. These sources will be located in the highest density regions in the universe, and their spatial clustering properties are well determined for a given cosmological scenario. Since most of the contribution comes from sources located at high redshift, their clustering properties turn out to be particularly relevant at angular scales of a few arcminutes. The shot noise associated with the Poissonian character of the source distribution will be relevant only at smaller angular scales. In Appendix A I provide a detailed computation of the statistical properties of the angular intensity fluctuations generated by the population of star-forming objects at high redshift. I find that, when probing sufficiently large scales, the

change of brightness can be written, to linear order in the perturbations, as an integral along the line of sight

$$\Delta I_\nu = \text{const} \quad + \quad \int_0^{r_{\rm LSS}} dr \left[\frac{\mathbf{v}\cdot\mathbf{n}}{c}\, a(r)\, \bar{n}(r)\, \frac{L_{\nu(1+z[r])}}{4\pi} + 2\,\frac{\dot{\phi}}{c}\, \bar{I}_\nu^{\rm dust}(r) \right] + \quad \int_0^{r_{\rm LSS}} dr\, a(r)\, \delta n(\mathbf{r})\, \frac{\mathbf{L}_{\nu(\mathbf{1}+\mathbf{z}[\mathbf{r}])}}{\mathbf{4}\pi}\, \mathbf{a^3}(\mathbf{r}) + \mathcal{O}(\delta^{\mathbf{2}}), \tag{4.1}$$

where r is the comoving distance, $a(r)$ the scale factor and $n(r)$ the number density of sources. The first term in the rhs is constant and introduces no anisotropy. The first integral contains the Doppler contribution, due to the peculiar velocity $\mathbf{v}$ of the sources, and the Integrated Sachs Wolfe (ISW) blueshift, due to time-varying potential $\dot{\phi}$, that the emitted photons experience as they travel towards the observer. These two contributions are found to be negligible when compared to the second integral, which provides the contribution introduced by the varying spatial distribution of sources. This term can be separated in the contribution from the so-called *Poisson* term, accounting for the Poissonian nature of the objects, and from the *correlation* term, accounting for dependence of the source number density on the environment density.

4.2. Results

In this section I present the angular power spectrum resulting from the distribution of dusty sources in the universe. As shown in Appendix A, such a power spectrum is the sum of two terms, the Poisson $C_l^{\rm P}$ and the correlation $C_l^{\rm C}$

$$\langle \Delta I_\nu(\mathbf{n}_1) \Delta I_\nu(\mathbf{n}_2) \rangle = \sum_l \frac{2l+1}{4\pi} \left(C_l^{\rm P} + C_l^{\rm C} \right) P_l(\mathbf{n}_1 \cdot \mathbf{n}_2), \tag{4.2}$$

where l is the multipole index and P_l is the Legendre polynomial of order l. The Poisson contribution to the angular power spectrum can be obtained from the source number counts (e.g. Scott & White 1999)

$$C_l^{\rm P}(\nu) = \int_0^{S_{\rm cut}} S_\nu^2 \frac{dN}{dS_\nu} dS_\nu \tag{4.3}$$

where all the sources brighter of $S_{\rm cut}$ are supposed to be removed. I present the results for $S_{\rm cut} = 100$ mJy at 353 GHz, unless otherwise specified.

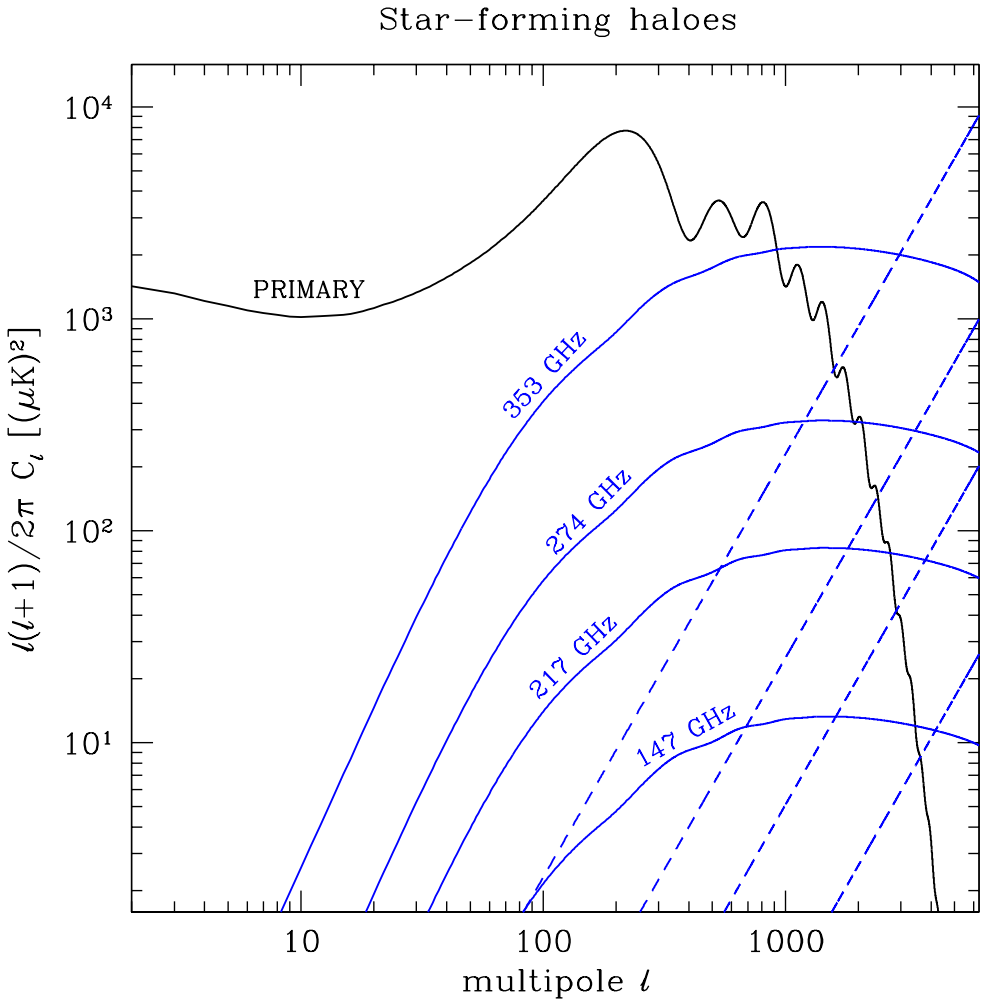

Figure 4.1: The Poisson (blue dashed line) and correlation (blue solid line) term of dust emission inside star-forming haloes, compared with the primordial CMB signal (black), at the four frequencies of the future CMB experiments (PLANCK, SPT and ACT): 353, 274, 217 and 147 GHz. Sources brighter than 100 mJy at 353 GHz have been removed in the computation of Poisson term.

The power spectra generated according to Equation (4.3) and by (A.22) for the correlation term are shown in Figure 4.1 at the four different frequencies of the future CMB experiments. The correlation term peaks in a broad range

$l = [200 - 3000]$. The Poisson signal is smaller than the correlation one for $l \lesssim 3000$ and becomes dominant only at the very large multipoles. Such multipoles, corresponding to angular scales of the order of a arcminute, are within the resolution limits of ACT and SPT. This plot shows that even at 147 GHz the fluctuations due to the dust emission in merging galaxies are one of the most important detectable extragalactic foregrounds. At higher frequencies it becomes dominant and at 353 GHz it should exceed the contribution from higher peaks (beginning from the fourth). As is well known, at 217 GHz the signal of the SZ clusters is negligibly small and this makes it much easier to observe the contribution from star-forming haloes.

Since Poisson power is generated mainly by very bright sources ($S \gtrsim 1$ mJy), future experiments should be able to detect such sources in the maps and eventually to remove them. In this way the correlation term can be detected also at very small scales, since it is slightly affected by rare bright sources and obtains the bulk of its power from the more abundant and less bright sources. I estimate this in Figure 4.2 at the 345 GHz SPT channel. This instrument is expected to have a sensitivity of about 0.3 mJy, and this should allow one to excise the brightest sources and hence increase the weight of the correlation term versus the Poissonian one. In the same plot I also compare the predictions of the model with the result that would be obtained if only the sources detectable by SCUBA were considered. The Poisson term would be at the same level, since it is generated mainly by the bright objects. The correlation would be strongly reduced, since SCUBA is not able to detect sources with flux lower than 0.2 mJy, missing the abundant dim sources which contribute significantly to the correlation power.

The analysis of the differential contribution to the signal from sources at different redshift (Figure 4.3) reveals that the bulk of the correlation is generated by star forming haloes in the redshift range $z \simeq 2 - 4$, with a slight dependence on the multipole l.

4.2.1. Contribution from normal spiral galaxies

Another contribution comes from the infrared emission of normal spiral galaxies, like the Milky Way. I decribe the distribution of such objects in space with the Press-Schechter mass function, weighted with the halo occupation number which gives the number of (blue) galaxies in a halo of given mass. Sheth &

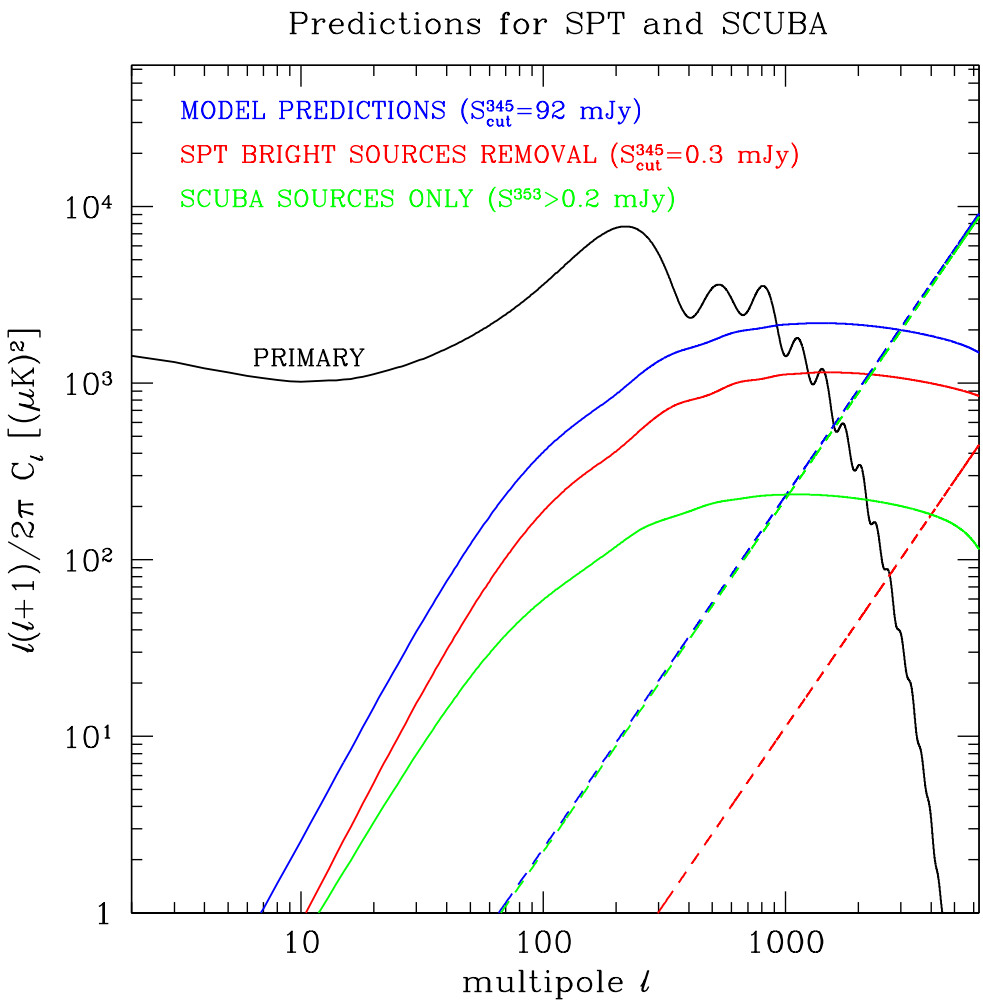

Figure 4.2: The angular power spectrum of star-forming haloes at 345 GHz: the red line is the predicted level of the fluctuations after the removal of the sources brighter than $\sim$ 0.3 mJy (corresponding to SPT sensitivity, Ruhl et al. 2004): compared with the model (blue) the Poisson term is reduced by more than one order of magnitude and the correlation term, which is much less dependent on bright sources, dominates up to higher multipoles. The green line is the predicted power spectrum considering only the sources detectable by SCUBA (with lensing technique) at 353 GHz (i.e. with flux greater than 0.2 mJy): the contribution of such sources to the correlation term is practically insignificant, while they make all the Poisson power.

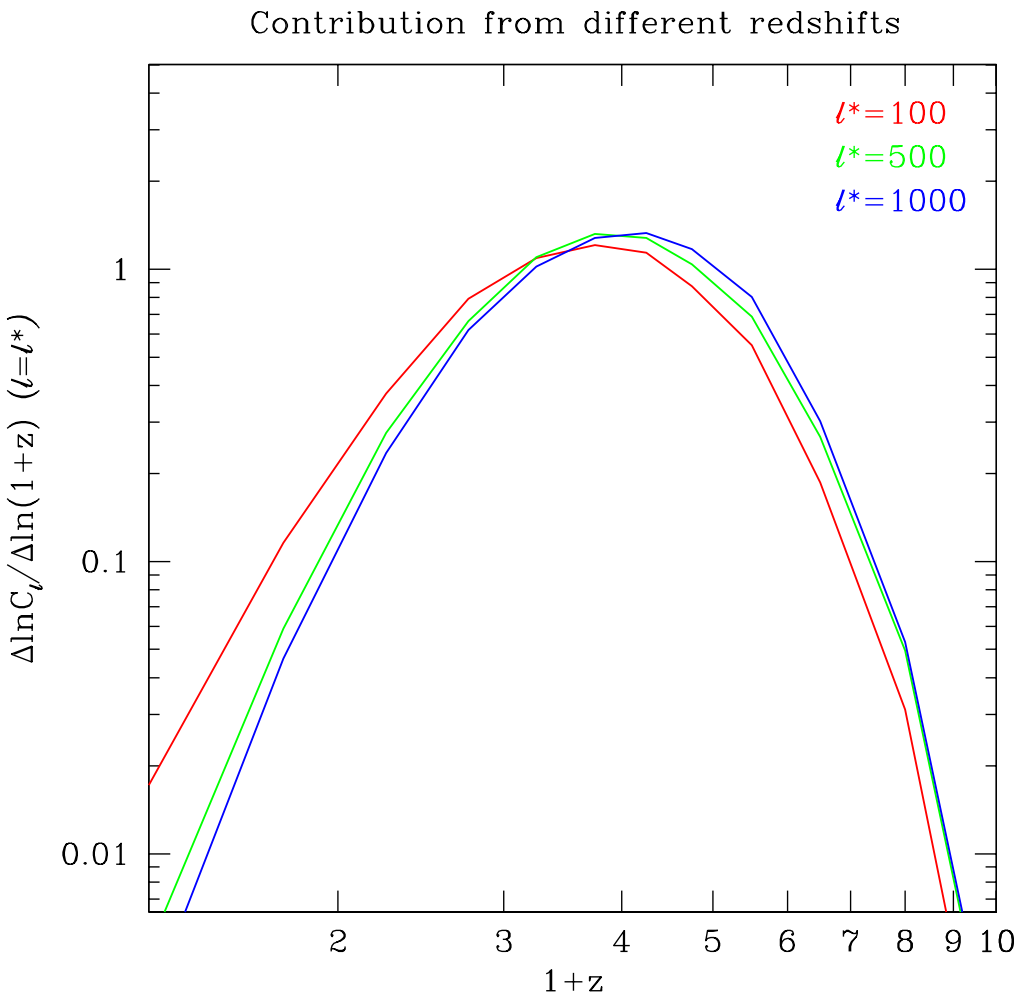

Figure 4.3: The differential contribution to the correlation term at 353 GHz as a function of redshift, for different angular scales: $l = 100$ (green), $l = 500$ (red) and $l = 1000$ (blue).

Diaferio (2001) propose the following form for such a quantity

$$N_{\rm gal}(M) = \left(\frac{M}{M_{\rm gal}}\right)^{\alpha} + 0.5 \exp\left\{-4\left[\log_{10}(M/10^{11.75})\right]^2\right\}, \qquad (4.4)$$

where M is the mass of the halo and with $M_{\rm gal} = 7 \times 10^{13}\, h^{-1} M_{\odot}$ and $\alpha = 0.9$. This fit is calibrated on the results of semi-analytical models and does not take

into account the dependence on redshift.
The correlation term resulting from this simple estimate is shown in Figure 4.4 (dotted curve) and turns out to be more than two orders of magnitude smaller than the signal due to the star-forming haloes.

4.2.2. Comparison with galactic foregrounds sources

In Figure 4.4 I present the well-known model of Tegmark et al. (2000) for the main galactic foregrounds at 217 GHz (since at this frequency the contribution from the thermal SZ is zero): the most intensive signal comes from the dust emission in our galaxy (long-dashed line), but it decreases rapidly at larger l, where the effect described here becomes dominant. The contribution from free-free emission (dotted line) and synchrotron radiation (short-dashed line) have similar dependence on l, but with much less power and should not affect the detection of the correlation term of dust in star-forming regions.
I also include the expected uncertainty of the noise level for the PLANCK HFI detectors. At 217 GHz the expected resolution is 5 arcmin, with a sensitivity $\Delta T/T = 4.8 \times 10^{-6}$. ACT and SPT telescopes are expected to give even better values of both resolution and sensitivity and hence a much lower level of noise. This should allow the detection of the dusty sources in the power spectrum.

4.2.3. Comparison with previous works

An estimate of the expected angular power spectrum of the cosmic infrared background was given by Haiman & Knox (2000). The model that they were using is different from the one presented here: it assumes a Press-Schechter distributed population of sources with a mass and redshift dependent dust content and temperature related to the stellar field. My model instead considers the distribution of *merging* objects, derived from the Lacey & Cole (1993) approach, and thus directly probes the star forming haloes. Given these different approaches, I compare my result at 353 GHz with their "hot dust" model and find a rather good agreement: the correlation term at $l = 1000$ is a factor ~ 1.4 (in ΔT) lower than their estimate.

Song et al. (2003) performed detailed computations for the FIR background, modelling the dust emission from star-forming galaxies within the framework of the halo model, but not considering merging. They presented the angular power spectra for the 545 GHz channel of PLANCK assuming a sky coverage corresponding to the cleanest 10% and including the unsubtracted Galactic dust. Their results are essentially in agreement with Haiman & Knox (2000).

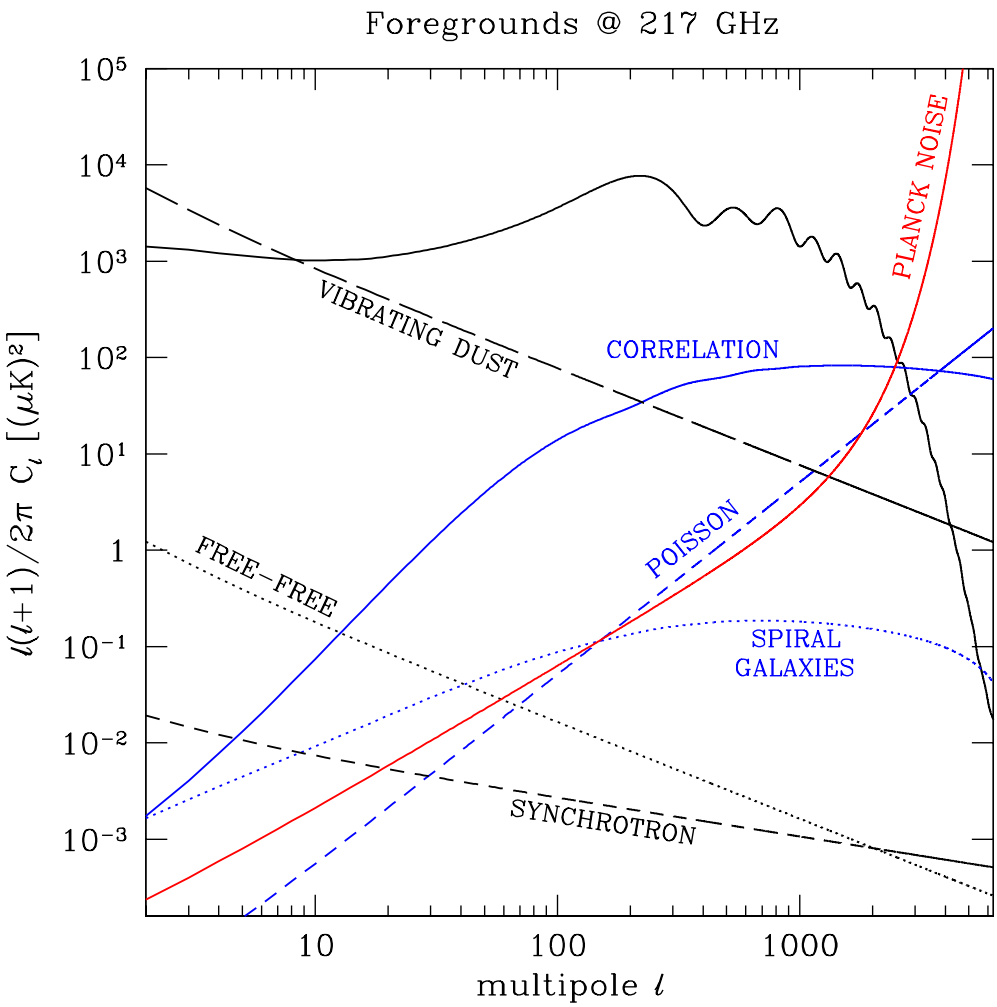

Figure 4.4: The effect of foregrounds according to the model of Tegmark et al. (2000), at 217 GHz: the long-dashed line refers to vibrating dust, free-free emission is plotted with the dotted-line and synchrotron radiation with the short-dashed line. The uncertainty on the noise level at 217 GHz for PLANCK is the red solid line, for a sky coverage $f_{\rm sky} = 85\%$. Solid and dashed blue curves represent my results for star-forming haloes, the dotted curve is the correlation term from spiral galaxies (see Section 4.2.1).

More recently, González-Nuevo et al. (2005) presented their predictions for the angular power spectrum of extragalactic point sources, based on the theoretical model of Granato et al. (2004). Comparing with their result at 353 GHz I find that at $l = 1000$ their correlation and Poisson terms are higher by a factor ~ 2.8 and ~ 1.6, respectively, than my predictions.

Toffolatti et al. (2005) presented an estimate of the power spectrum of the ACBAR sources at 150 GHz. My estimate for the Poisson term at the same frequency (and for the same flux limit $S_{\rm cut}^{150} = 24$ mJy) is roughly a factor 1.6 lower; I have a similar deficit when comparing with SCUBA observations.

From these comparisons, it is clear that the contribution to the background fluctuations from the sub-millimeter sources in my model is lower than predicted by other authors, but in general their results are confirmed.

4.3. Sensitivity to the parameters

The model presented in this thesis is sensitive to several parameters. As I pointed out in Chapter 3, it may be feasible to calibrate these parameters with the existing observations. The main purpose of this work is to make predictions for the level of foreground of dusty sources in the universe and to show that this signal will be important for upcoming experiments.
However, this component should open an additional way to study the population of the most distant star-forming galaxies, which are already enriched by dust. The amplitude of the signal could provide a very useful tool to understand the physical nature of the objects. For example, the amount of dust could be derived if estimates are obtained about the actual value of the escape fraction, since these two quantities are related. Multifrequency observations will permit one to separate the contribution of distant dusty haloes from other background/foreground sources due to their characteristic spectrum, and could lead to a more precise estimate of the spectral properties of dust emission, in particular the temperature. The extremely high resolution of ALMA will make it possible even to individually detect very distant objects and to provide hints about their dust emission, in particular if information about their redshift is also retrieved (by observing, for instance, the emission in the fine-structure lines of the most abundant ions which were detected by COBE-FIRAS in the sub-millimeter spectrum of our galaxy and which were discussed in Basu et al. (2004)). Measuring the spectrum of the additional fluctuations in the CMB at different multipoles may also set constraints on the star formation scenario and confirm that the star formation at high redshift begins in strongly overdense

regions which will eventually evolve into clusters and superclusters of galaxies at $z \sim 0.5 - 0.7$ and that the first star-forming haloes very rapidly create a high abundance of metals and dust.
In this section I will explore the parameter space and present several results for the angular power spectrum as a function of different parameters.

4.3.1. Spectral parameters

The shape of the correlation term is fixed once the merger model is established, since it determines the distribution of star-forming haloes as a function of their luminosity. However, the merger model is connected only to the total infrared luminosity through the Kennicutt relation. To obtain the value of the anisotropy in a specific frequency channel, one has to assume some kind of spectral distribution for the sources. In Section 2.4 I assumed a greybody distribution depending on the emissivity index β and on the dust temperature $T_{\rm dust}$. Based on the comparison with the SCUBA source counts (Figure 4.5), I chose $\beta = 1.5$ and $T_{\rm dust} = 30$ K. These values are in agreement with the observational constraints, which give a wide range of values both for the emissivity index ($1.0 \leq \beta \leq 2.0$) and the dust temperature ($30\ {\rm K} \leq T_{\rm dust} \leq 50\ {\rm K}$). As shown in Figure 4.6, the amplitudes of the correlation and Poisson term are sensitive to the choice of the spectral parameters and display a variation over one order of magnitude in the range of possible values. It is clear, from these plots, that the two spectral parameters show a degeneracy. Multifrequency observations may allow one to reduce the extent of such degeneracy, as shown in the following.

4.3.2. Frequency dependence

As explained in Section 2.4, the contribution from high redshift objects in the highest frequency bands of future experiments is expected to be low, due to the shift at wavelengths shorter than the 100 μm peak in the emission spectrum. On the other hand, moderate frequency channels will be very sensitive even to extremely distant objects, since their emission will occur at wavelengths longer than the peak. This is shown in Figure 4.7, where the correlation term, normalized to the signal at 100 GHz, is compared for different frequencies: while this ratio stays almost constant at 147, 217 and 274 GHz, it decreases at 353 GHz, towards the higher multipoles, corresponding to the smallest angular scales and hence to the most distant objects, whose emissivity at these frequencies is far beyond the peak, on the Wien tail of the spectrum.

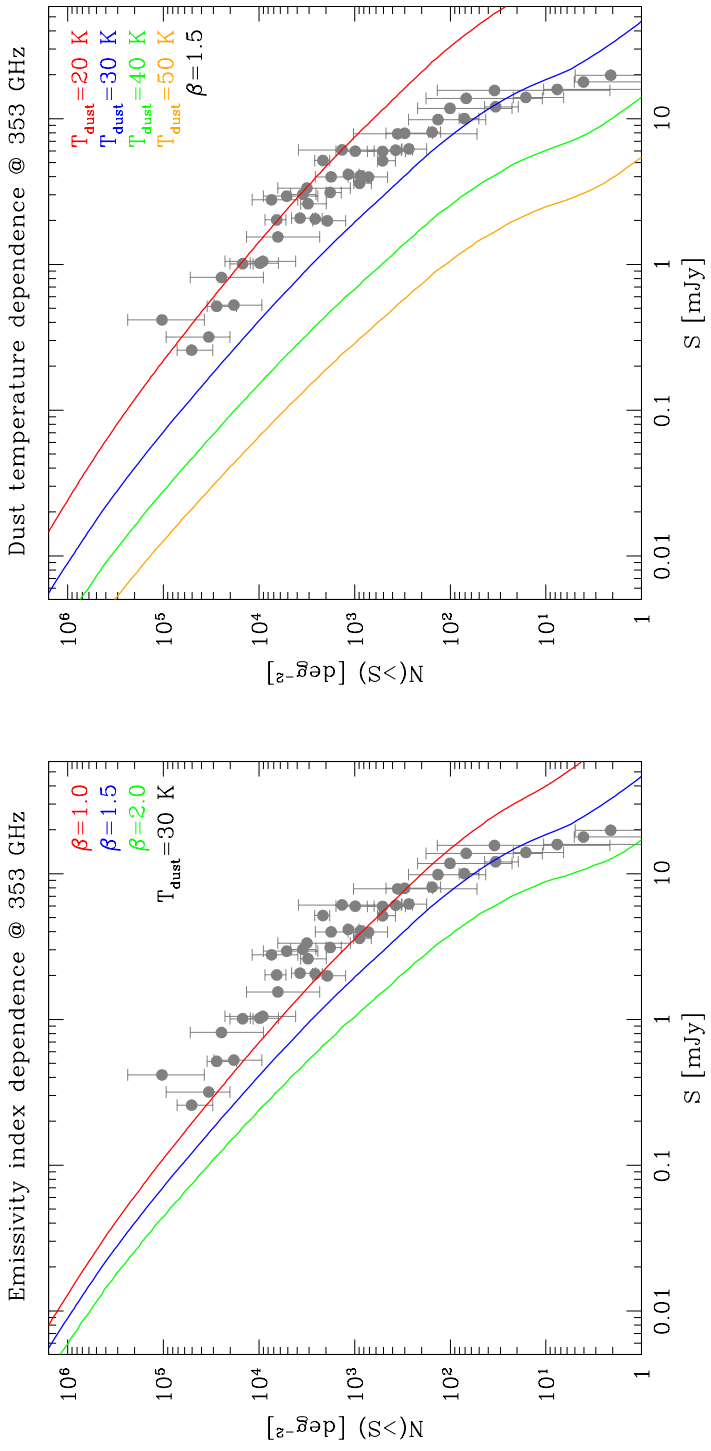

Figure 4.5: Sensitivity of the results for the integral source counts at 353 GHz to the choice of the spectral parameters: emissivity index (*left*, for fixed value of the dust temperature, 30 K) and dust temperature (*right*, for fixed value of the emissivity index, 1.5). Grey dots are the SCUBA observations, as in Figure 3.1. The curves in blue represent the choice which I use for all the results presented in this chapter. The plausible range of dust temperatures derived from the observations (Dunne & Eales 2001; Chapman et al. 2005) is 30-50 K.

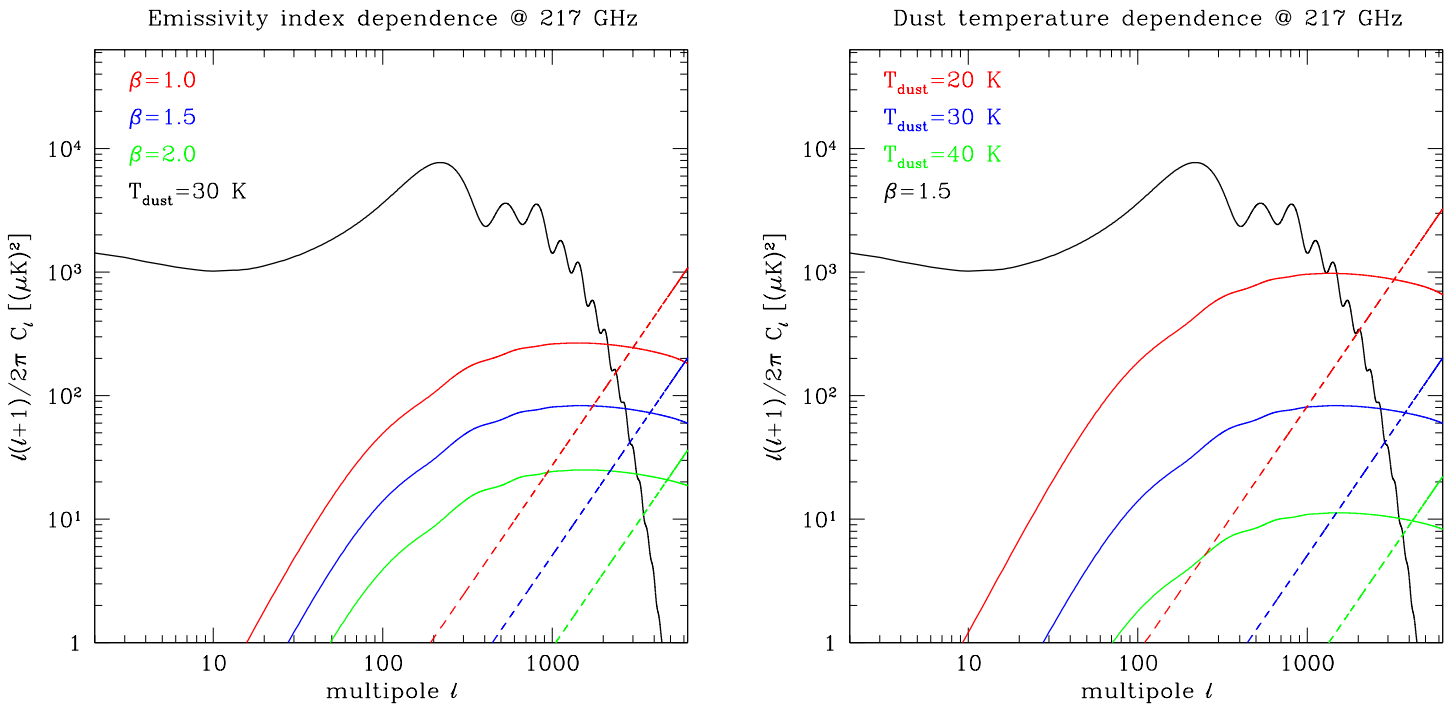

Figure 4.6: Sensitivity of the Poisson and correlation term at 217 GHz to the choice of the free parameters for the dust spectrum: emissivity index β (*left*, for fixed value of the dust temperature, 30 K) and dust temperature $T_{\rm dust}$ (*right*, for fixed value of the emissivity index, 1.5). The curves in blue represent the choice which I use for all the results presented in this chapter.

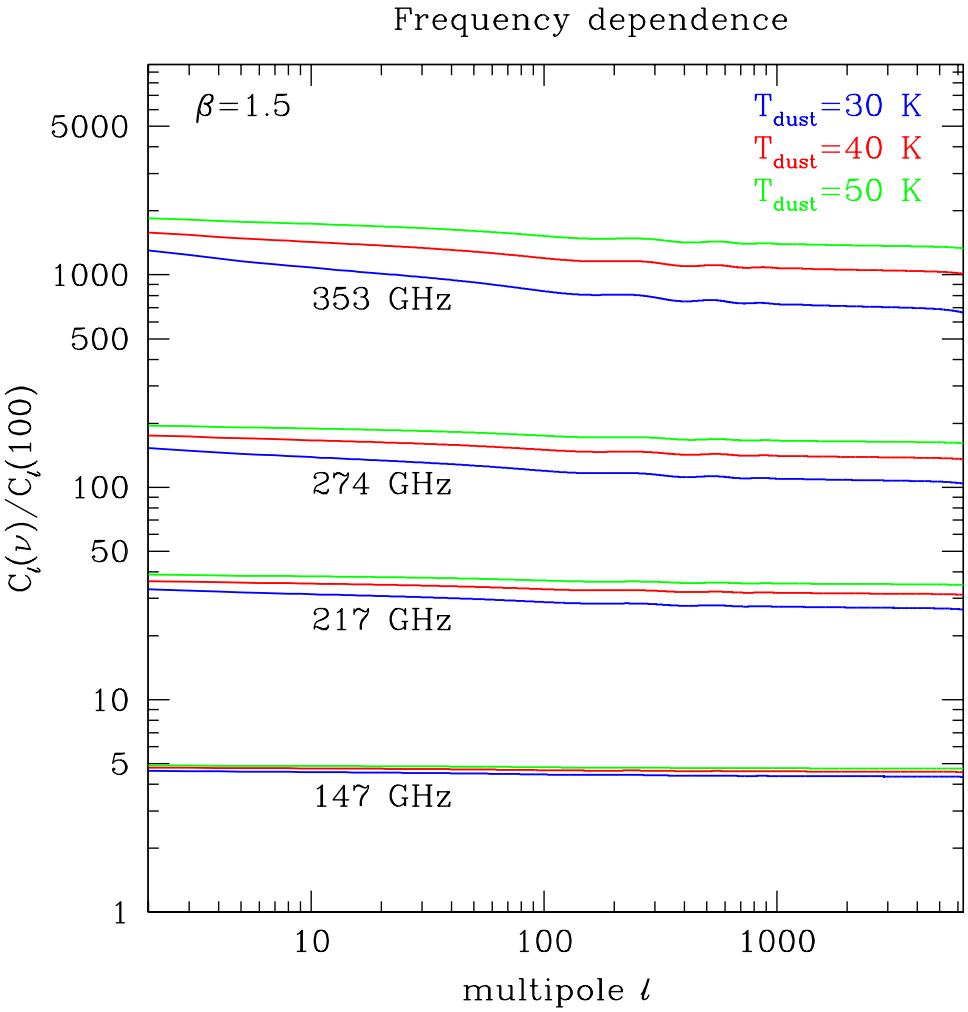

Figure 4.7: The ratio of the correlation signal at different frequencies to the signal at 100 GHz, for different values of the dust temperature.

The level of such a decrease at higher frequencies is somewhat temperature dependent. Higher dust temperatures shift the position of the peak in the spectrum towards higher frequencies and shift the position of the sources beyond the peak towards higher redshift. This effect could be useful to measure the dust temperature of extremely distant objects, breaking the degeneracy between β and $T_{\rm dust}$ pointed out above, since the value of β has no influence on the position of the peak in the spectrum.

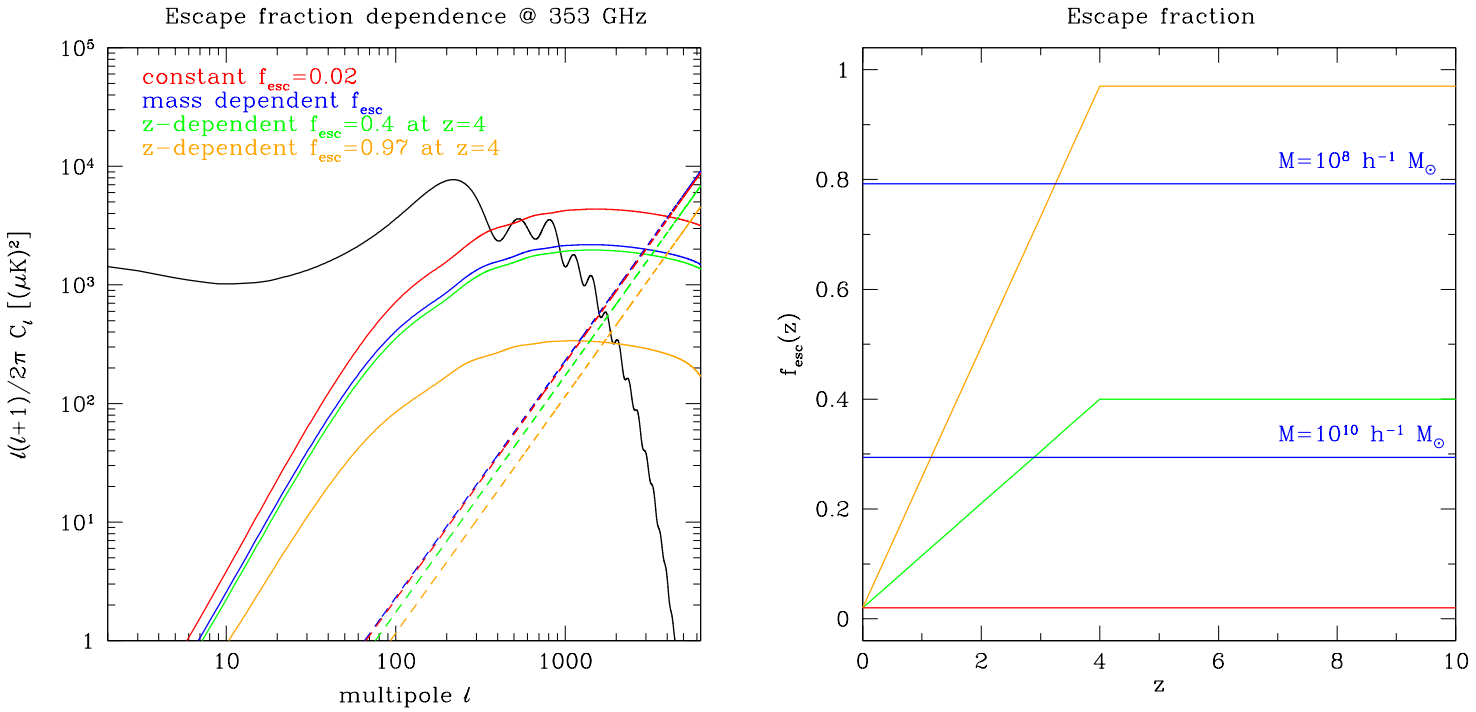

Figure 4.8: *Left:* the dependence of the correlation (solid) and Poisson (dashed) term on different parametrization for the escape fraction with redshift (*right*) at 353 GHz: low and constant (red), low and redshift dependent (green), high and redshift dependent (orange); blue lines correspond to the mass-dependent escape fraction adopted in the compromise model and show constant redshift evolution for given mass.

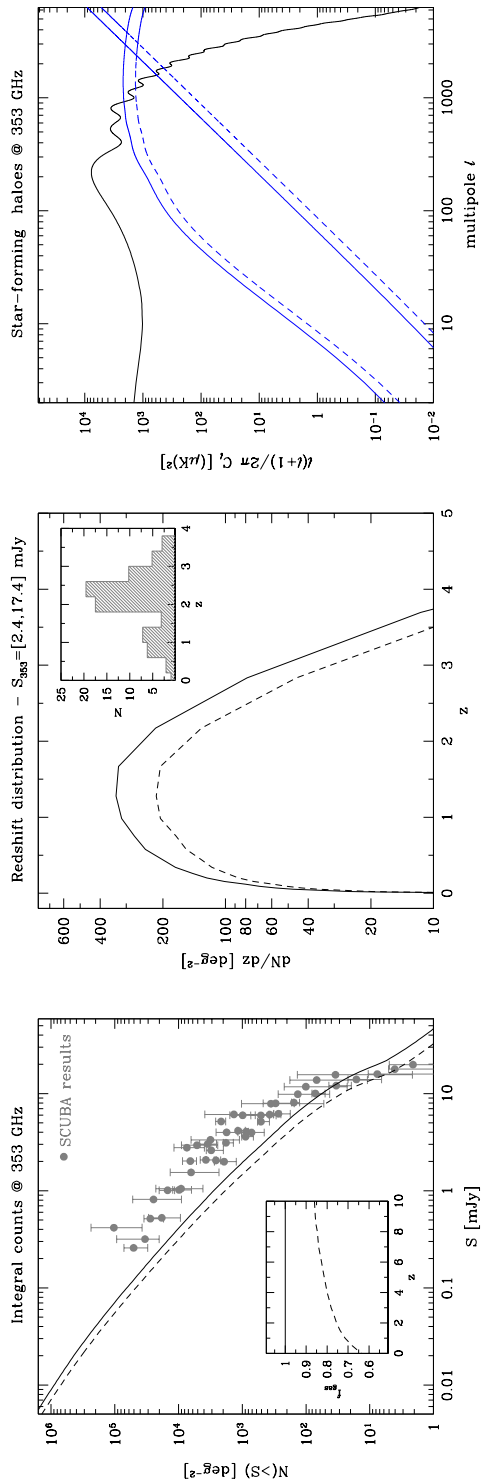

Figure 4.9: The dependence of the results on the gas fraction. Solid lines refer to the model predictions with $f_{\rm gas} = 1$, dashed lines correspond to the correction in Equation (4.5), displayed in the insert in the left panel.

4.3.3. Escape fraction

As mentioned in Section 3.2.1, I introduce an escape fraction for the ionizing photons in order to satisfy the limits of COBE-FIRAS on the intensity of the infrared background. In the compromise model, which provides all the main results of this work, the escape fraction is modelled as a function of the halo mass (Equation 3.3). Here I present some other possibilities and show how these would affect the results on the fluctuations.
GALEX and SPITZER recently obtained several estimates for the escape fraction in nearby luminous galaxies ($L_{IR} \gtrsim 10^{11}\, L_{\odot}$, see e.g. Buat et al. 2007). The published data do not give precise information about the value of the escape fraction at high redshift ($z \sim 3-5$) from where most of the contribution to the correlation term comes. Similarly, up to now there is no clear idea about the dependence of the escape fraction on galaxy mass. I present here three further parametrizations: a constant and low escape fraction of 2%, an escape fraction growing with redshift from 2% at $z = 0$ to 40% at $z = 4$ and another one from 2% to 97%.
The correlation and Poisson terms at 353 GHz, corresponding to these parametrizations are plotted in the left panel of Figure 4.8: the blue line is the compromise model with the mass dependent escape fraction, the red line is the constant $f_{\rm esc} = 0.02$: the correlation term in this case in much stronger because the luminosity of the sources is weakly limited by the correction. The two Poisson terms are, on the other hand, very similar, since in the mass-dependent model the most massive (and bright) objects that build up the Poisson power are also weakly affected by the correction. The green and orange lines are the two models with redshift dependent escape fractions: the correlation term is strongly reduced in the case of $f_{\rm esc}(z = 4) = 0.97$, while the Poisson term, which is generated mainly by low redshift sources, is less affected.

4.3.4. Gas fraction

An additional parameter of the model is the gas fraction inside haloes at different redshift. This quantity establishes the amount of gas that is available at each epoch for the formation of new stars. As explained in Section 2.1, so far I have assumed that all the baryons inside the haloes are in gas form. This approximation is good at high redshift, when the number of stars is small, but it breaks down as more and more baryons are locked into stars. A simple way

to describe this effect is to write the gas fraction at each redshift as

$$f_{\rm gas}(z) = 1 - \frac{\rho_\star(z)}{\rho_{\rm b}(z)} = 1 - \frac{\int_0^{t(z)} \dot{\rho}_\star dt}{\frac{\Omega_{\rm b}}{\Omega_{\rm m}} \int M \frac{dn}{dM} dM}, \tag{4.5}$$

where $\rho_{\rm b}$ is the density of cold baryons inside haloes (the integral in the denominator is limited to those masses which are able to cool) and $\rho_\star(z)$ is the stellar density, obtained integrating Equation (3.5) in time. In this way the contribution of massive objects and the level of the angular fluctuations is reduced about 30% (Figure 4.9).

4.4. Intergalactic dust

To conclude this chapter, I consider the effect of the intergalactic dust, that is expelled from galaxies by strong winds and AGN activity. This dust is heated by the ultraviolet background and by the CMB. Here I will adopt the well-know two components model (silicate and graphite), which can explain the interstellar dust properties in the Galaxy and the Magellanic Clouds reasonably well. Although there is no evidence that the intergalactic dust has the same properties of the dust in our vicinity, I assume this as a working hypothesis. Size distributions and optical properties are taken from Weingartner & Draine (2001).

4.4.1. Equilibrium temperature

The dust uniformly distributed in space, heated up by ultraviolet background and CMB, will attain an equilibrium temperature $T_{\rm IGM}$, given by the balance equation

$$\int da \, \frac{dn}{da} \, \sigma_\nu \, I_\nu^{\rm EBL} \, d\nu = \int da \, \frac{dn}{da} \, \sigma_\nu \, B_\nu(T_{\rm IGM}) \, d\nu. \tag{4.6}$$

The lhs represents the absorbed radiation, which is proportional to the cross section for absorption σ_ν, and $I_\nu^{\rm EBL} = I_\nu^{\rm UV} + I_\nu^{\rm CMB}$ is the illuminating field of the extragalactic sources. The rhs is the thermal emission term, which depends likewise on σ_ν.

For the ultraviolet background I take the model of Kitayama et al. (2001), in which the radiation field is assumed to be isotropic and to be the sum of two contributions, QSOs and stars

$$I_\nu^{\rm UV} \propto I_\nu^{\rm QSO} + I_\nu^\star \propto \mathcal{A}\nu^{-\alpha} + \mathcal{B}\frac{\nu^3}{\exp(h\nu/kT_{\rm eff}) - 1}, \tag{4.7}$$

with $\mathcal{A}$ and $\mathcal{B}$ constant. I adopt a spectral index $\alpha = 1$ and an effective temperature $T_{\rm eff} = 10^4$ K.
The resulting equilibrium temperature is shown in Figure 4.10: dust temperature increase upto $z \sim 5$, then decrease and at $z \gtrsim 7$ attains the equilibrium with CMB.

4.4.2. Radiative transfer

The interaction between a dust particle and a CMB photon can occur through two processes: scattering and absorption/emission. By *scattering* I understand the absorption of one CMB photon and immediate re-emission of the same photon with the same frequency (the best example is Rayleigh scattering on the dust particles). By *absorption* I understand the absorption of a CMB photon and the emission, some time later, of a different photon with a different (larger) wavelength. The energy difference is converted into thermal energy of the dust particle. When implementing these mechanisms in the radiative transfer equation, it turns out that they leave a very similar imprint on the CMB, but with very different amplitudes. Indeed, for an axially symmetric black body intensity field given by

$$B_\nu(T,\mu) = B_\nu(T_0)\left[1 + a\mu + b\left(\frac{3\mu^2-1}{2}\right) + \sum_{l=3}^{\infty} C_l\, P_l(\mu)\right], \tag{4.8}$$

Zeldovich & Syunyaev (1980) found that its relative change after absorption and scattering on dust particles at rest with the observer reads:

$$\frac{\Delta I_\nu(\mu)}{I_\nu^0}\Big|_{\rm abs} = -\tau_{\rm abs}\left[a\mu + b\left(\frac{3\mu^2-1}{2}\right) + \sum_{l=3}^{\infty} C_l\, P_l(\mu)\right] \tag{4.9}$$

$$\frac{\Delta I_\nu(\mu)}{I_\nu^0}\Big|_{\rm sca} = -\tau_{\rm sca}\left[a\mu + 0.9b\left(\frac{3\mu^2-1}{2}\right) + \sum_{l=3}^{\infty} C_l\, P_l(\mu)\right], \tag{4.10}$$

where $\mu \equiv \cos\theta$ and P_l are the Legendre polynomia, a and b are the expansion coefficient for the dipole and quadrupole, respectively. The last two equations show that two different physical processes give rise to similar changes in the intensity field. However, since $\tau_{\rm abs} \gg \tau_{\rm sca}$ for intergalactic dust, the signatures of scattering will be neglected when compared to those of absorption, and henceforth only this process will be taken into consideration.
Equation (4.9) demonstrates that the absorption of sub-millimeter photons leads to a diminishing of the primordial angular fluctuations.

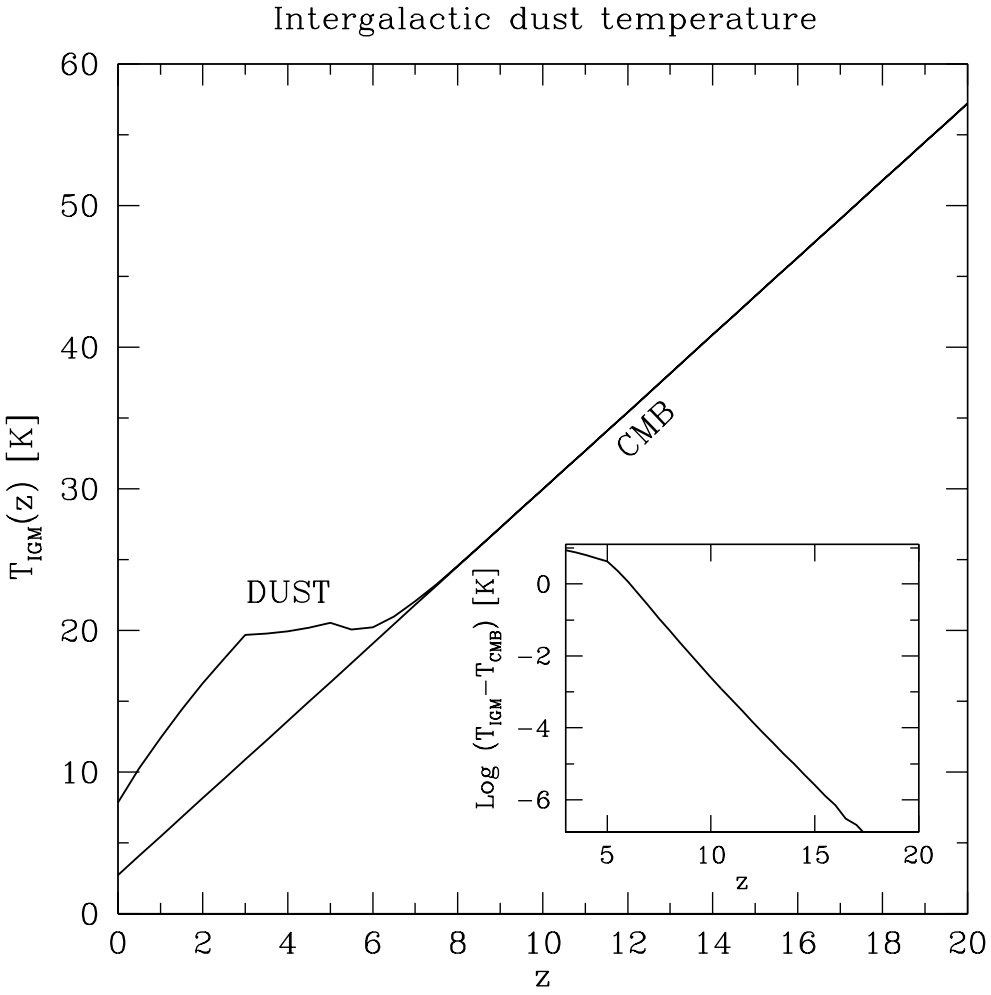

Figure 4.10: Temperature of the intergalactic dust and of the cosmic microwave background. The insert displays the difference between the two temperatures in logarithmic scale.

4.4.3. Average density and optical depth

Following the approach of Inoue & Kamaya (2004, hereafter IK04), in which the amount of intergalactic dust is constrained by extinction and reddening of distant Type Ia supernovae and by the thermal history of intergalactic medium, I derive the mean abundance of dust as a function of redshift. The starting

point is the cosmic mean metallicity evolution which can be computed, once the star formation history is specified, as

$$\rho_Z(z) = y_Z \int_z^\infty \dot{\rho}_\star(z') \left| \frac{dt}{dz'} \right| dz', \tag{4.11}$$

where y_Z is the produced metal mass fraction per unit of star-forming mass. I will assume a constant value $y_Z = 0.024$ (Madau et al. 1996). For the evolution of $\dot{\rho}_\star$ I use the result obtained from the merging model, presented in Section 3.3. The amount of intergalactic dust is set by the parameter χ, defined as the ratio between dust mass and total metal mass. Its value is quite uncertain: based on the observations of the cosmic star formation history an upper value of $\chi \simeq 0.1$ can be assumed. The dust grain density in the IGM is then written

$$\rho_{\rm dust}(z) = \chi\, \rho_Z(z). \tag{4.12}$$

The same quantity can be estimated following another line of reasoning and considering the well-known object M82. This is a nearby starburst galaxy in the M81 group. It has quite high luminosity ($5{\times}10^{10} L_\odot$), most of which is emitted in the infrared. It is interacting with the spiral galaxy M81 and the dwarf starburst galaxy NGC 3077. M82 is a so-called superwind galaxy in which the central starburst drives a mass outflow perpendicular to the plane of the galaxy. According to the observations of Alton et al. (1999), this galaxy has a star formation rate of $10\, M_\odot$/yr with a dust production rate of $0.015\ M_\odot$/yr. The lifetime of the starburst is estimate to be 5×10^7 years thus leading a total dust output of about $10^6 M_\odot$. Assuming this galaxy to be the archetype of the starburst galaxy I can calculate the dust production efficiency as the ratio of the dust production rate to the star formation rate $\eta_{\rm dust} = \dot{M}_{\rm dust}/\dot{M} = 1.5 \times 10^{-3}$. The dynamical timescale of the dust outflow in M82 is an order of magnitude smaller than the lifetime of the starburst: the dust which has been built up in the disk has subsequently been expelled during the last 10% of the starburst phase.
Assuming this mechanism, it is possible to calculate the dust density in the IGM as

$$\rho_{\rm dust}(z) = \int_z^\infty \dot{\rho}_\star(z')\, \eta_{\rm dust} \left| \frac{dt}{dz'} \right| dz', \tag{4.13}$$

where $\eta_{\rm dust}$ is assumed constant and $\dot{\rho}_\star$ is cosmic star formation rate given in Equation (3.5).

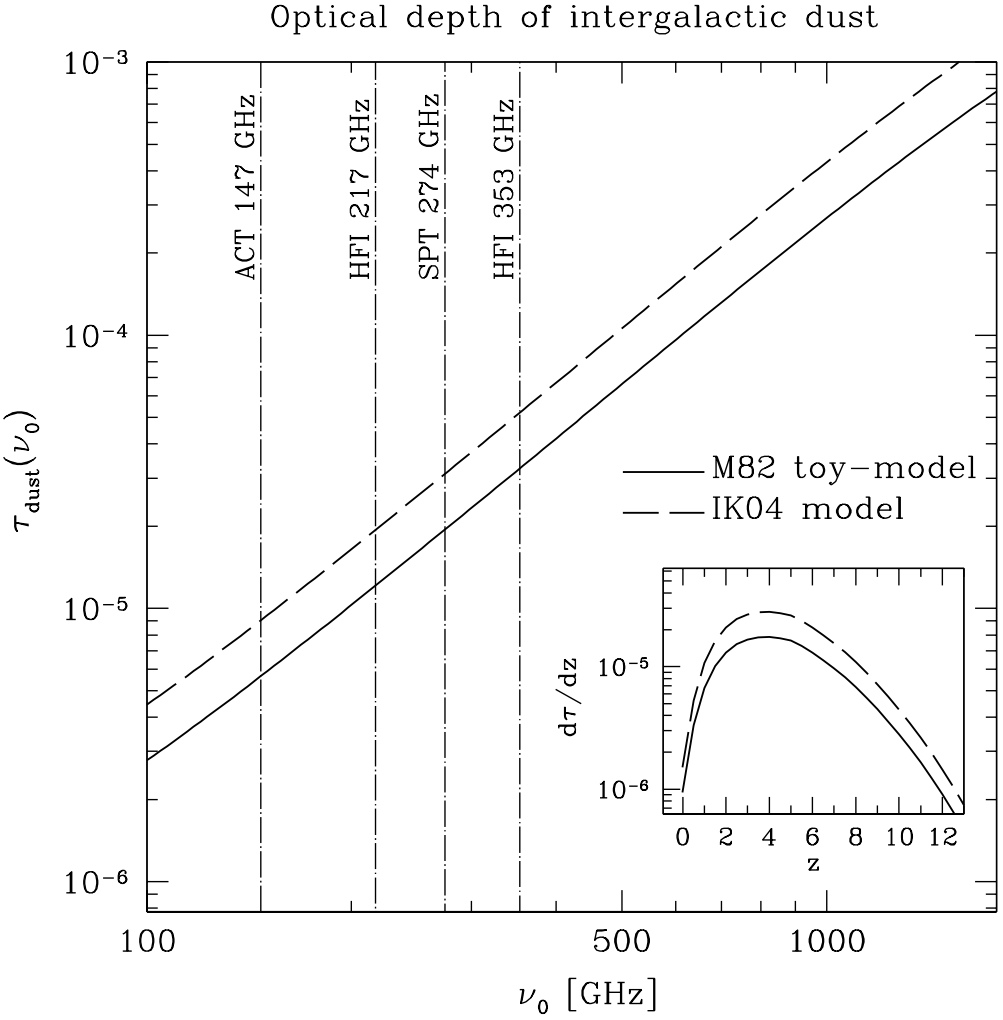

Figure 4.11: Optical depth of intergalactic dust in the optically thin limit, computed according to the two models described in the text: M82 toy-model (solid line) and IK04 model (dashed lines). Vertical lines show the observing frequencies of PLANCK HFI, ACT and SPT detectors. The contribution from different redshift at 217 GHz is shown in the insert.

The optical depth for absorption generated by this uniform distribution of dust is obtained integrating along the line of sight

$$\tau_{\rm dust}(\nu_0) = \mathcal{A}(z) \int_0^\infty da \left(\frac{dn_{\rm gr}}{da} \sigma^{\rm gr}_{\nu_0(1+z)} + \frac{dn_{\rm sil}}{da} \sigma^{\rm sil}_{\nu_0(1+z)} \right) \frac{dl}{dz} dz, \qquad (4.14)$$

where σ_ν is the absorption cross section, $\nu_0 = \nu/(1+z)$ is the observing frequency and $\mathcal{A}$(z) is the normalization of the size distribution. In our Galaxy this normalization is related to the hydrogen number density in the insterstellar medium. Here I normalize to the intergalactic dust density, Equations (4.12) and (4.13). The result is shown in Figure 4.11: the two estimates, based on completely independent observational data, give similar numerical values.

4.4.4. The signature of intergalactic dust in the power spectrum

As shown above, the dust uniformly distributed in space is heated up by the ultraviolet background and by the CMB. The equilibrium temperature of this component is much lower than for the dust inside the sources, and is close to the temperature of the background for $z \gtrsim 6$. At lower redshifts, though, the dust temperature is significantly higher than the CMB temperature, and this translates into an effective injection of photons to the background. However, here I am concerned about the angular intensity fluctuations generated by an uniform dust distribution. If the dust emission takes place only at $z = 0$, then it is clear that the effect of photon injection will be restricted to the intensity monopole. But since I am considering the presence of dust at higher redshifts, an observer today will be able to see dust emission coming from different regions in the Universe corresponding to different, causally disconnected universes at the epoch the photons were injected in the CMB background. The dust overall density and peculiar velocities with respect to the CMB frame might be slightly different from one region to another, and this effect should introduce intensity fluctuations in the very large angular scales.

However, in the small angle range, where most of upcoming high-sensitivity CMB experiments are going to be working, the effect is the opposite: CMB photons will be absorbed by dust particles, and then re-emitted isotropically (according to my model of uniform dust distribution). This will reflect in an effective blurring of the intrinsic CMB angular intensity anisotropies at scales where dust is uniform, i.e., at the scales smaller than the horizon size at photon absorption-emission epoch. This can be modelled by introducing an absorption optical depth in the radiative transfer equation, and, as shown by Basu et al. (2004), leaves a distinct change in the CMB angular power spectrum: $\delta C_l \simeq -2\tau_{\rm dust}(\nu) C_l$ (high l), where C_l is the primordial CMB signal and $\tau_{\rm dust}$ is defined in Equation (4.14). This appears clear in Figure 4.12, where the effect is shown at 353 GHz.

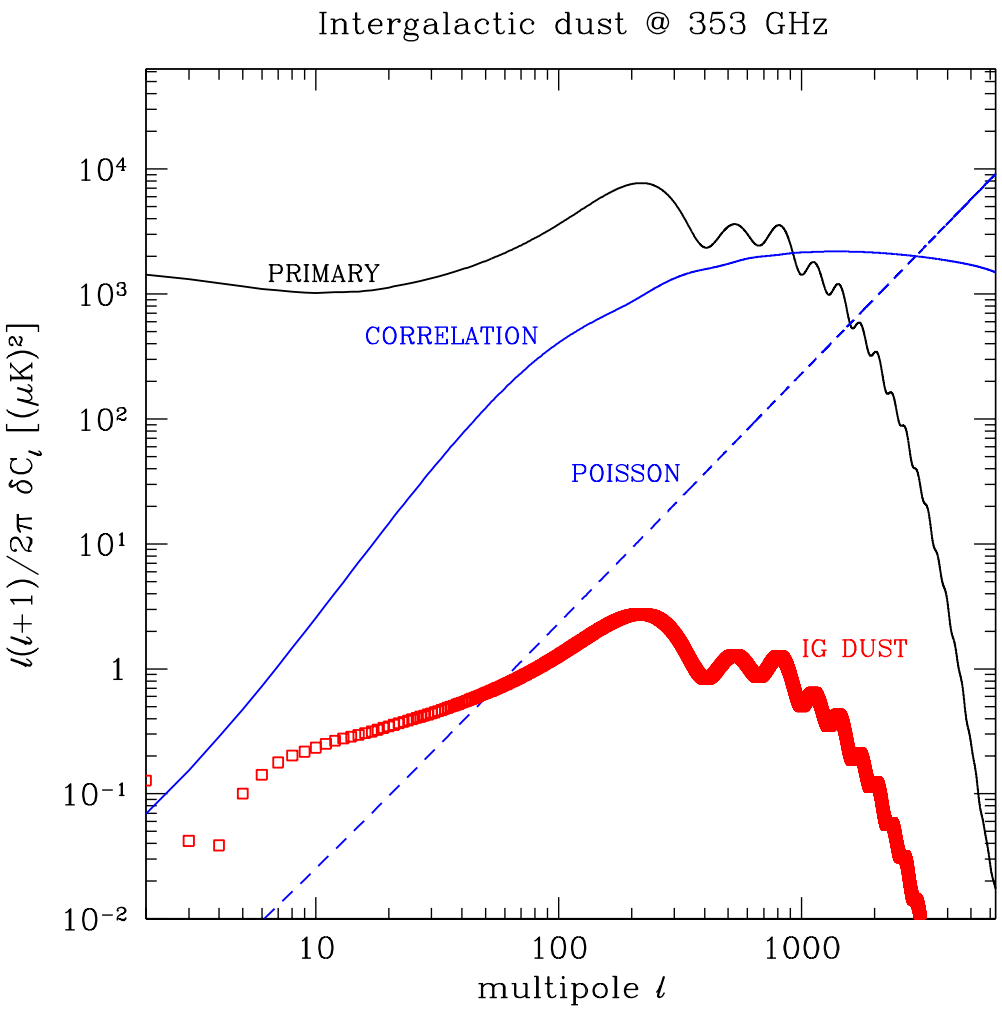

Figure 4.12: The change in the power spectrum induced by the diffuse intergalactic dust at 353 GHz. Red squares represent the difference $\delta C_l = C_l^{\rm dust} - C_l$. Blue lines are the two terms from dust in haloes, black line is the primordial signal.

Comparing the results for dust in haloes and intergalactic dust, I can conclude that the former dominates at higher l, where the power of the primordial signal falls rapidly due to Silk damping, and the latter it is more important at lower multipoles, $l = [10 - 200]$.

5

Carbon monoxide line emission as CMB foreground

In Chapter 2, I modelled the star formation in a merger episode and characterized the distribution of the merging systems using the extended Press-Schechter formalism of Lacey & Cole (1993). In each merging episode a given amount of gas is converted into stars, proportionally to the mass of the haloes involved in the process, with a given efficiency η. I took this to be 5%, in order to match the observations of the cosmic star formation history (Hopkins & Beacom 2006). The lifetime of the starburst phase was then introduced following the results of the several numerical simulations available in literature (e.g. Mihos & Hernquist 1994, 1996; Springel & Hernquist 2005; Robertson et al. 2006): there are two star formation bursts, corresponding to the first close passage of one galaxy around the other and to the final coalescence, with a typical duration of ~ 300 and $\lesssim 100$ Myr, respectively. A third phase, identified as the star formation activity already present in the two galaxy before the interaction, was not included in the model, since it is not directly triggered by the merging. This simple parametrization allowed me to the derive a statistical description of the merging events as a function of their star formation rates.

Comparing the typical timescale of the bright phase (~ 100 Myr) with the characteristic evolution time for old stars, which is about 1 Myr, one can easily prove that these objects are rapidly enriched with metals already at high red-

shift. The line emission from molecules, atoms and ions might be an additional source of foreground for CMB oservations. This is the main argument that motivate the work presented in this chapter.

5.1. Line luminosities from a sample of objects

In the previous chapters, I applied the merging model to describe a population of far-infrared haloes, therefore I used the Kennicutt relation for that band (Kennicutt 1998). Here I aim to describe the luminosity in the line for a set of molecular and atomic transitions which occur in the observing band of the CMB experiments. I will follow a similar approach, assuming that line luminosity scales with the star formation rate

$$L_{\rm line}[L_\odot] = \mathcal{R} \cdot \dot{M}_\star \, [M_\odot/{\rm yr}] \tag{5.1}$$

The constant $\mathcal{R}$ which connects the two quantities depends on several parameters and it is not easy to determine it. To get a rough estimate of its value for different lines I will select a sample of objects and retrieve data on their line luminosity from the literature.
For the CO transitions I will consider a low- and a high-redshift sample. The first is derived from the list of Baan et al. (2008) which contains more than a hundred sources, observed with different instruments: I have selected in this list only the galaxies with optical size smaller than the beam size of the observation. This is to avoid an underestimate of the flux due to incomplete coverage of the source. More detailed studies have been done on well-known local objects like M82 (Weiß et al. 2005b) and NGC4038/39 (also known as The Antennae, Gao et al. 2001; Bayet et al. 2006). These are however extended sources and one has to be very careful with the observational results, since these depend on the actual region covered by the instrument. In the case of M82, Weiß et al. (2005b) presented an accurate model of the CO emission from this galaxy which takes into account both the central and the outer regions. The combined emission is a reliable estimate of what would be observed if M82 was shifted to cosmological distances, therefore I will use it to calibrate the $\mathcal{R}$ ratio for most of the results presented in this chapter. The relatively small mass of M82 ($M \sim 10^{10}\,M_\odot$, Mayya et al. 2006) is typical for the objects which contribute to the bulk of the correlation term estimated here ($M = 10^9 - 10^{11}\,M_\odot$ for redshift $z = 3 - 5$). The data of the low-redshift sample are presented in Table 5.1.

The high-redshift sample contains many sub-millimeter galaxies. These are very massive and luminous systems, powered by intense starburst and/or AGN

Object name	d_L [Mpc]	SFR [$M_\odot$/yr]	CO 1-0 [$L_\odot$]	CO 2-1 [$L_\odot$]	CO 3-2 [$L_\odot$]	CO 4-3 [$L_\odot$]	CO 5-4 [$L_\odot$]	CO 6-5 [$L_\odot$]	CO 7-6 [$L_\odot$]
M82	3.63	10.1	3.7×10^4 a	2.8×10^5 a	7.1×10^5 a	9.8×10^5 a	9.7×10^5 a	9.6×10^5 a	9.0×10^5 a
			$\mathbf{3.7 \times 10^3}$	$\mathbf{2.8 \times 10^4}$	$\mathbf{7.0 \times 10^4}$	$\mathbf{9.7 \times 10^4}$	$\mathbf{9.6 \times 10^4}$	$\mathbf{9.5 \times 10^4}$	$\mathbf{8.9 \times 10^4}$
Antennae	21.8	11.8	1.8×10^5 b						
			$\mathbf{1.5 \times 10^4}$						
Milky Way	-	3.0		8.5×10^4 c	1.2×10^5 c	1.3×10^5 c	9.5×10^4 c		
				$\mathbf{2.8 \times 10^4}$	$\mathbf{4.0 \times 10^4}$	$\mathbf{4.3 \times 10^4}$	$\mathbf{3.2 \times 10^4}$		
IRAS 01077-1707	145	72.9	2.9×10^5 d						
			$\mathbf{4.0 \times 10^3}$						
IRAS 01364-1042	207	98.4	2.3×10^5 d						
			$\mathbf{2.3 \times 10^3}$						
IRAS 04454-4838	220	105	1.6×10^5 d						
			$\mathbf{1.5 \times 10^3}$						
IRAS 08520-6850	205	98.4	1.3×10^5 d						
			$\mathbf{1.3 \times 10^3}$						
IRAS 09111-1007	243	171	3.8×10^5 d						
			$\mathbf{2.2 \times 10^3}$						
IRAS 14348-1447	388	341	6.9×10^5 d						
			$\mathbf{2.0 \times 10^3}$						
IRAS 14378-3651	315	242	2.7×10^5 d						
			$\mathbf{1.1 \times 10^3}$						
IRAS 18293-3413	80.6	110	5.3×10^5 d	2.2×10^6 d					
			$\mathbf{4.8 \times 10^3}$	$\mathbf{2.0 \times 10^4}$					
IRAS 19115-2124	216	127	5.1×10^5 d						
			$\mathbf{4.0 \times 10^3}$						
IRAS 20550+1656	136	127	1.7×10^5 d	4.8×10^5 d					
			$\mathbf{1.3 \times 10^3}$	$\mathbf{3.8 \times 10^3}$					
IRAS 22491-1808	350	220	3.0×10^5 d						
			$\mathbf{1.4 \times 10^3}$						

Table 5.1: Luminosities and $\mathcal{R}$ ratios (in boldface) of the CO lines for the local and low-redshift sample of galaxies. The star formation rates are obtained applying the Kennicutt (1998) relation to the far-infrared ($8 - 1000\,\mu$m) luminosity given in the *IRAS revised bright galaxies sample* (Sanders et al. 2003). For our Galaxy we use the value of star formation rate given by Cox (2000). References: (a) Weiß et al. (2005b), (b) Gao et al. (2001), (c) Wright et al. (1991), (d) Baan et al. (2008).

Object name	z	SFR $[M_\odot/\mathrm{yr}]$	CO 1-0 $[L_\odot]$	CO 2-1 $[L_\odot]$	CO 3-2 $[L_\odot]$	CO 4-3 $[L_\odot]$	CO 5-4 $[L_\odot]$	CO 6-5 $[L_\odot]$	CO 7-6 $[L_\odot]$
SMM J16359⋆	2.52	500 a			6.0×10^6 b-d	1.1×10^7 b	1.7×10^7 b	1.6×10^7 b	
					$\mathbf{1.2 \times 10^4}$	$\mathbf{2.2 \times 10^4}$	$\mathbf{3.4 \times 10^4}$	$\mathbf{3.2 \times 10^4}$	
SMM J02396⋆•	1.06	975 e		7.9×10^6 f					
				$\mathbf{8.1 \times 10^3}$					
SMM J13120•	3.41	810 g	1.0×10^7 g			1.7×10^8 f			
			$\mathbf{1.2 \times 10^4}$			$\mathbf{2.1 \times 10^5}$			
SMM J16366	2.45	1455 i			7.7×10^7 f,h				3.3×10^8 h
					$\mathbf{5.3 \times 10^4}$				$\mathbf{2.3 \times 10^5}$
SMM J16371•	2.38	877 i			4.0×10^7 f				
					$\mathbf{4.6 \times 10^4}$				
SMM J22174	3.10	1800 e			5.1×10^7 f				
					$\mathbf{2.8 \times 10^4}$				
SMM J04431⋆•	2.51	450 e			1.4×10^7 h,j				2.4×10^7 h
					$\mathbf{3.1 \times 10^4}$				$\mathbf{5.3 \times 10^4}$
SMM J09431⋆•	3.35	1200 g	$< 2.5 \times 10^6$ g			8.9×10^7 h,j			
			$< \mathbf{2.1 \times 10^3}$			$\mathbf{7.4 \times 10^4}$			
SMM J16368•	2.38	897 i			9.3×10^7 h,j				3.7×10^8 h,j
					$\mathbf{1.0 \times 10^5}$				$\mathbf{4.1 \times 10^5}$
SMM J02399⋆•	2.80	500 k			6.6×10^7 k,l				
					$\mathbf{1.3 \times 10^5}$				
SMM J14011⋆	2.56	360 e			2.4×10^7 l,m				6.9×10^7 m
					$\mathbf{6.7 \times 10^4}$				$\mathbf{1.9 \times 10^5}$
SMM J123549•	2.20	1163 n			5.6×10^7 h			1.6×10^8 h	
					$\mathbf{4.8 \times 10^4}$			$\mathbf{1.4 \times 10^5}$	
ERO J16450	1.44	1539 o	3.2×10^6 o	1.5×10^7 d			3.6×10^7 p		
			$\mathbf{2.1 \times 10^3}$	$\mathbf{9.7 \times 10^3}$			$\mathbf{2.3 \times 10^4}$		

Table 5.2: Luminosities and $\mathcal{R}$ ratios (in boldface) of the CO lines for the high-redshift sample of submillimeter galaxies. Luminosities of the lensed sources (marked with ⋆) are corrected with the magnification factors given in Greve et al. (2005) and Solomon & Vanden Bout (2005). The presence of an AGN is indicated by the symbol •. References: (a) Kneib et al. (2004), (b) Weiß et al. (2005a), (c) Sheth et al. (2004), (d) Kneib et al. (2005), (e) Solomon & Vanden Bout (2005), (f) Greve et al. (2005), (g) Hainline et al. (2006), (h) Tacconi et al. (2006), (i) Kovács et al. (2006), (j) Neri et al. (2003), (k) Genzel et al. (2003), (l) Frayer et al. (1999), (m) Downes & Solomon (2003), (n) Takata et al. (2006), (o) Greve et al. (2003), (p) Andreani et al. (2000).

Object name	z	SFR $[M_\odot/\mathrm{yr}]$	CO 1-0 $[L_\odot]$	CO 2-1 $[L_\odot]$	CO 3-2 $[L_\odot]$	CO 4-3 $[L_\odot]$	CO 5-4 $[L_\odot]$	CO 6-5 $[L_\odot]$	CO 7-6 $[L_\odot]$
MS 1512⋆	2.73	15 a			5.9×10^5 b				
					$\mathbf{4.0 \times 10^4}$				
Q 0957⋆	1.41	900 a		7.6×10^6 c					
				$\mathbf{8.5 \times 10^3}$					
IRAS F10214⋆	2.29	540 a			2.2×10^7 d-g			4.2×10^7 f	
					$\mathbf{4.0 \times 10^4}$			$\mathbf{7,7 \times 10^4}$	
CLOVERLEAF⋆	2.56	810 a			4.8×10^7 h-k	1.2×10^8 j	1.7×10^8 j		4.6×10^8 j
					$\mathbf{5.9 \times 10^4}$	$\mathbf{1.5 \times 10^5}$	$\mathbf{2.1 \times 10^5}$		$\mathbf{5.7 \times 10^5}$
RX J0911⋆	2.80	345 a			7.1×10^6 l				
					$\mathbf{2.1 \times 10^4}$				
SMM J04135⋆	2.84	3600 a			2.3×10^8 l				
					$\mathbf{6.4 \times 10^4}$				
MG 0751⋆	3.20	435 a			3.2×10^7 m				
					$\mathbf{7.2 \times 10^4}$				
PSS J2322⋆	4.11	1800 a	2.6×10^6 n	2.5×10^7 n	2.3×10^8 o		2.5×10^8 o		
			$\mathbf{1.4 \times 10^3}$	$\mathbf{1.4 \times 10^4}$	$\mathbf{1.3 \times 10^5}$		$\mathbf{1.4 \times 10^5}$		
BRI 0952⋆	4.43	360 a					4.3×10^7 p		
							$\mathbf{1.5 \times 10^5}$		
B3 J2330	3.09	1950 a				1.1×10^8 q			
						$\mathbf{5.6 \times 10^4}$			
TN J0121	3.52	1050 a				1.3×10^8 r			
						$\mathbf{1.2 \times 10^5}$			
6C 1909	3.54	1470 a				1.7×10^8 s			
						$\mathbf{1.2 \times 10^5}$			

Table 5.3: Same as Table 5.2, for the high-redshift sample of QSO and radiogalaxies. References: (a) Solomon & Vanden Bout (2005), (b) Baker et al. (2004), (c) Planesas et al. (1999), (d) Brown & Vanden Bout (1991), (e) Solomon et al. (1992b), (f) Solomon et al. (1992a), (g) Downes et al. (1995), (h) Barvainis et al. (1994), (i) Wilner et al. (1995), (j) Barvainis et al. (1997), (k) Weiß et al. (2003), (l) Hainline et al. (2004), (m) Barvainis et al. (2002), (n) Carilli et al. (2002), (o) Cox et al. (2002), (p) Guilloteau et al. (1999), (q) De Breuck et al. (2003a), (r) De Breuck et al. (2003b), (s) Papadopoulos et al. (2000).

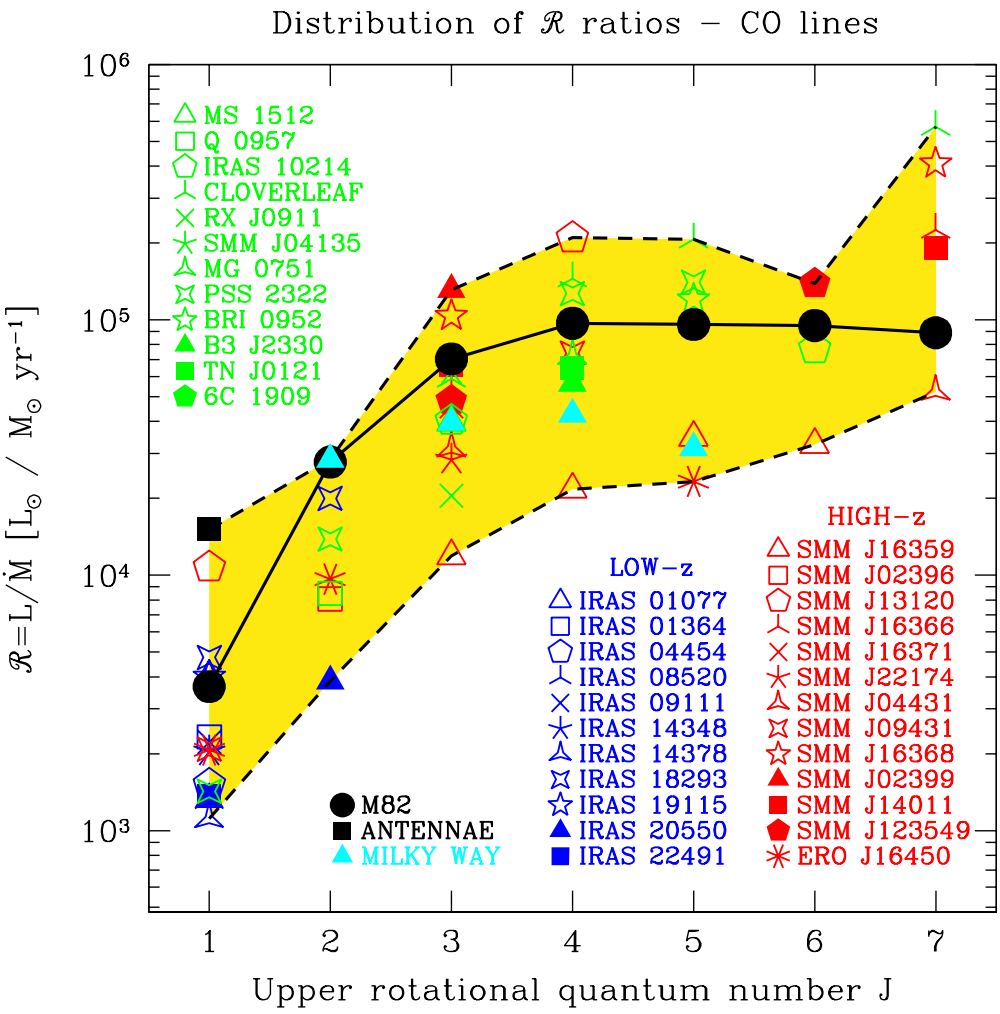

Figure 5.1: The distribution of the $\mathcal{R} = L/\dot{M}$ ratios as a function of the upper rotational quantum number of the CO transitions. Three different samples are considered: low-redshift IRAS galaxies (blue points), high-redshift sub-millimeter galaxies (red points) and high-redshift radiogalaxies and QSOs (Greve et al. 2005; Solomon & Vanden Bout 2005, green points). M82 and the Antennae are shown in black. Our Galaxy (Wright et al. 1991; Cox 2000) is represented with the cyan triangles. See Tables 5.1-5.3 for details. Black solid line is SED for M82, for which I have data for the full set of lines. Dashed lines represent the lower and upper limits for $\mathcal{R}$ in the sample.

and emit the bulk of their radiation in the infrared band. This activity is triggered by merging episodes which provide with large amount of gas and results in high values of the star formation rate. I retrieved from the literature the line luminosity for several objects, including QSOs and radiogalaxies (Table 5.2 and 5.3): these observations were carried out with interferometric technique, therefore they are more sensitive to bright small spots and not to the continuum emission. Comparing the average $\mathcal{R}$ of this sample with the one obtained for M82, I found that there is no big difference, though the CO spectral energy distribution for the high-redshift objects tends to peak at higher values of the rotational quantum number J. This may derive from differences in the temperature and in the density of the gas. Furthermore, in the high redshift objects, the presence of the non-negligible radiation field of the CMB contributes to increase the excitation level of the CO molecule.

All these observational data are summarized in Figure 5.1: here I plot the $\mathcal{R} = L/\dot{M}$ ratio as a function of the upper rotational quantum number of the transition; a higher value of $\mathcal{R}$ corresponds to a higher luminosity of the galaxy per unit star formation rate and therefore to a higher amplitude in the fluctuations. I include the two samples of objects described above: local objects (black points), low-redshift IRAS galaxies (blue), high-redshift sub-millimeter galaxies (red), QSO and radiogalaxies (green). The spectral energy distribution of M82, for which we have the full set of line, is overplotted in black solid lines. I also show here the values for our Galaxy (cyan triangles), as observed by COBE-FIRAS (Wright et al. 1991), assuming a star formation rate of 3 $M_{\odot}$/yr (Cox 2000). From this dataset I can extract an estimate of the lower and upper value of $\mathcal{R}$ in every transition: this is shown in dashed lines in the same figure. Notice that local merging objects, which are intrinsically weaker than the QSO, are close to the upper limit, meaning that they have a higher luminosity per unit star formation rate. M82 and the Antennae, for example, are extremely bright in the first two transitions, compared with the other objects. There is rather large scatter in the distribution of this points at different J. This might be due to the uncertainties in the CO properties or more probably in the value of $\dot{M}$ measured in these objects.

The observations of bright distant quasars and galaxies show that they often have carbon and oxygen abundance close or even higher than the solar value (Fan 2006). It is clear that in the high-redshift universe the average abundance of metals is much lower than in the regions with intense star formation, where it can increase extremely rapidly. The Magellanic clouds (LMC and SMC) have significantly lower chemical abundance than our Galaxy, nevertheless the luminosities of the CO lines are comparable. This problem is of particular

interest for the first line of the CO, since this is heavily saturated and therefore its brightness depends weakly on the chemical abundance. On the other hand, higher-J lines are usually optically thin and therefore their brightness strongly depends on the chemical abundance.

5.2. The angular power spectrum

In the Appendix B I present a detailed derivation of the expressions which I use to compute the angular power spectrum generated by the emission in these lines. Here I shall briefly outline the main results. First of all, I should remark that the measured signal $\tilde{I}_\nu(\hat{\mathbf{n}})$ is actually a convolution of the underlying signal $I_\nu(\mathbf{r} = r\hat{\mathbf{n}})$ with an experimental window function $\mathcal{B}(\mathbf{r})$.

$$\tilde{I}_\nu(\mathbf{r}) = \int d\mathbf{r}' \mathcal{B}(\mathbf{r} - \mathbf{r}')\, I_\nu(\mathbf{r}'). \tag{5.2}$$

This window function $\mathcal{B}$ simply accounts for the finite angular and spectral resolutions of the observing device. The variance of the signal can be expressed as a function of the measured power spectrum ($|\tilde{I}_{\nu,\mathbf{k}}|^2$)

$$\langle \tilde{I}_\nu^2 \rangle = \int \frac{d\mathbf{k}}{(2\pi)^3} |\tilde{I}_{\nu,\mathbf{k}}|^2 = \int \frac{d\mathbf{k}}{(2\pi)^3} |\mathcal{B}_\mathbf{k}|^2 P_s(k) |\bar{I}_\nu|^2, \tag{5.3}$$

where $\bar{I}_\nu$ denotes the volume weighted intensity amplitude for a given source, and $P_s(k)$ is the power spectrum describing the spatial distribution of the sources. This integral reflects the contribution of anisotropy (given by the power spectrum $P_s(k)$) to each k scale range, and this depends on the size and distribution of the sources. If these are randomly (Poisson) distributed in space, then $P_s(k) = 1/n$, with n the average source number density. This means that *all* scales contribute with the same amount of anisotropy (as given by the k-independent power spectrum P_s), down to a minimal linear scale (maximum k) corresponding to either the size of the source or the resolution element of the instrument. If the source size is taken arbitrarily small, and the angular resolution is fixed, then the variance or measured anisotropy will increase if the instrument is sensitive to smaller and smaller scales *in the radial direction*, i.e., it will scale as $k_{\rm max} \sim 1/(\Delta z) \sim 1/(\Delta\nu)_{\rm inst}$, with z denoting the linear scale along the radial direction. More generally, if soures are Poisson distributed, any improvement in the spectral/angular resolution that makes the experiment sensitive to smaller scales (that are still larger that the typical source size) will yield an increase in the measured power.

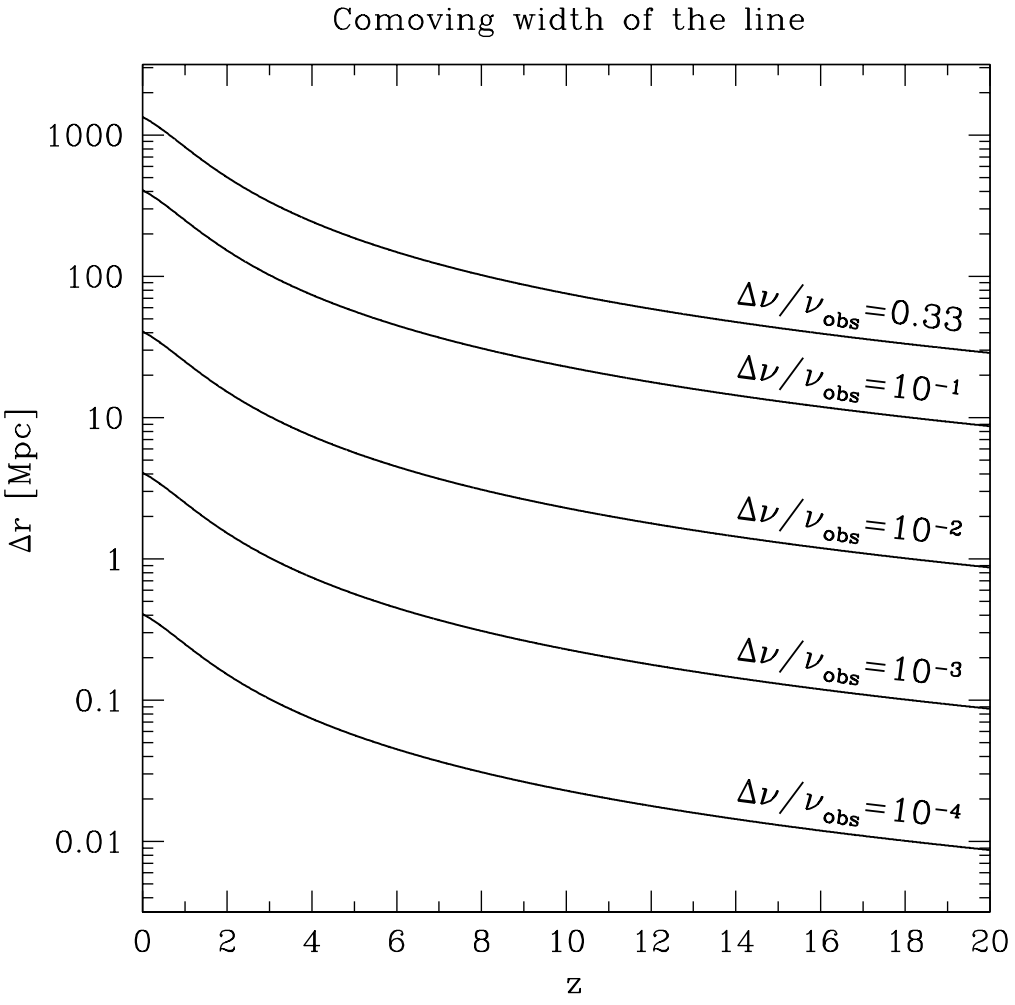

Figure 5.2: The actual comoving width of the slice (in Mpc) as a function of redshift, probed by different values of the spectral resolution $\Delta\nu/\nu_{\rm obs}$.

However in the Universe sources tend to be clustered in regions of $L_c \sim$ 25-45 h^{-1} Mpc (comoving size) that eventually will become superclusters of galaxies. The distribution of these regions will introduce further anisotropy, but only at scales that are actually larger than L_c. If the frequency/angular resolution of the experiment is at some point able to resolve this scale, then further improving such resolution will make no difference. This can be reworded in Fourier space as follows. If sources are distributed such that their power spec-

trum is proportional to that of the underlying density field ($P_s(k) \propto P_m(k)$), then for some large k the contribution of the power spectrum to the integral of eq.(5.3) will be negligible (since for large k we have that $P_m(k) \to 0$). In this scenario, increasing the spectral resolution will not change the integral over $P_s(k)$. These two distinct regimes will be addressed in detail below.

After projecting the power spectrum on the sphere, the expressions for the Poisson (C_l^P) and correlation (C_l^C) angular power spectra are found (see Appendix). Their relation to the angular correlation function reads

$$\langle \tilde{I}_\nu(\hat{\mathbf{n}}_1)\tilde{I}_\nu(\hat{\mathbf{n}}_2)\rangle = \sum_l \frac{2l+1}{4\pi}\left(C_l^{\mathrm{P}} + C_l^{\mathrm{C}}\right) P_l(\hat{\mathbf{n}}_1 \cdot \hat{\mathbf{n}}_2), \tag{5.4}$$

with $P_l(\hat{\mathbf{n}}_1 \cdot \hat{\mathbf{n}}_2)$ the Legendre polynomia of order l .

In this approach the resolution is expressed in terms of a comoving width Δr probed at a given redshift by a certain $\Delta\nu/\nu_{\mathrm{obs}}$. It is straightforward to derive the relation

$$\Delta r = \frac{\Delta r}{\Delta z}\frac{\Delta z}{\Delta \nu}\Delta\nu = \frac{cH_0^{-1}}{E(z)}\frac{\Delta\nu}{\nu_{\mathrm{obs}}}, \tag{5.5}$$

where $\Delta\nu/\nu_{\mathrm{obs}}$ refers to the observing frequency and $E(z) = [\Omega_{\mathrm{m}}(1+z)^3+\Omega_\Lambda]^{1/2}$. From this equation, it is clear that for a fixed spectral resolution, the actual comoving width decreases with increasing redshift, as it is shown in Figure 5.2.

5.3. Results for the CO lines

5.3.1. Source counts and background intensity

In Figure 5.3 I present the differential source counts in the CO lines, predicted by the model at 30, 70 and 100 GHz, for a spectral resolution $\Delta\nu/\nu_{\mathrm{obs}} = 10^{-3}$ and using M82 to calibrate the $\mathcal{R}$ ratio. The vertical lines in each plot shows the sensitivity of ALMA to lines emission (5σ value, for 3 hours integration. Tarenghi & Wilson 2005): this values is approximately constant at these frequencies.
The flux in the line is computed as

$$\begin{aligned} S_\nu &= \frac{\int d\nu_{\mathrm{obs}}\,\phi_{\mathrm{instr}}\dfrac{L_\nu}{4\pi r^2(1+z)}}{\int d\nu_{\mathrm{obs}}\phi_{\mathrm{instr}}} = \int d\nu_{\mathrm{obs}}\,\phi_{\mathrm{instr}}\frac{L_{\mathrm{bol}}\phi_{\mathrm{th},\nu}}{4\pi r^2(1+z)} = \\ &= \frac{1}{4\pi r^2(1+z)}\frac{L_{\mathrm{bol}}}{(\Delta\nu)_{\mathrm{instr}}} = \frac{\tilde{L}_\nu}{4\pi r^2}\left(\frac{\Delta\nu}{\nu_{\mathrm{obs}}}\right)^{-1}_{\mathrm{instr}}, \end{aligned} \tag{5.6}$$

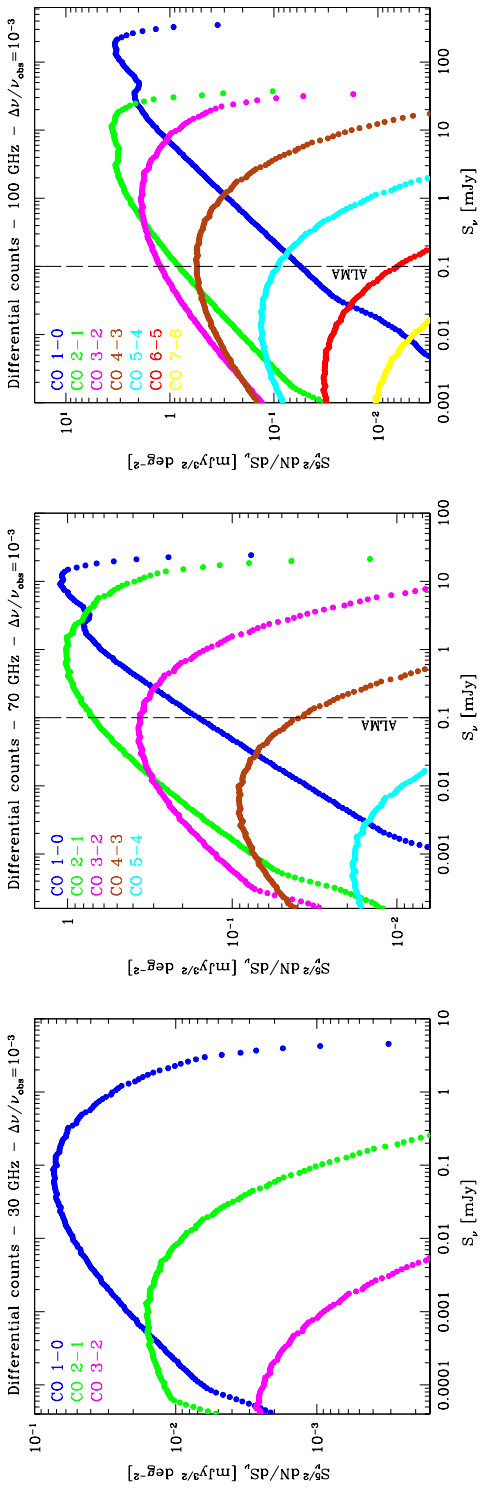

Figure 5.3: The predicted differential source counts for the CO lines at 30, 70 and 100 GHz, for a spectral resolution $\Delta\nu/\nu_{\rm obs} = 10^{-3}$ and using the $\mathcal{R}$ from M82. The vertical lines is the expected sensitivity of ALMA to the line emission, computed for the same spectral resolution and an integration time of 3 hours.

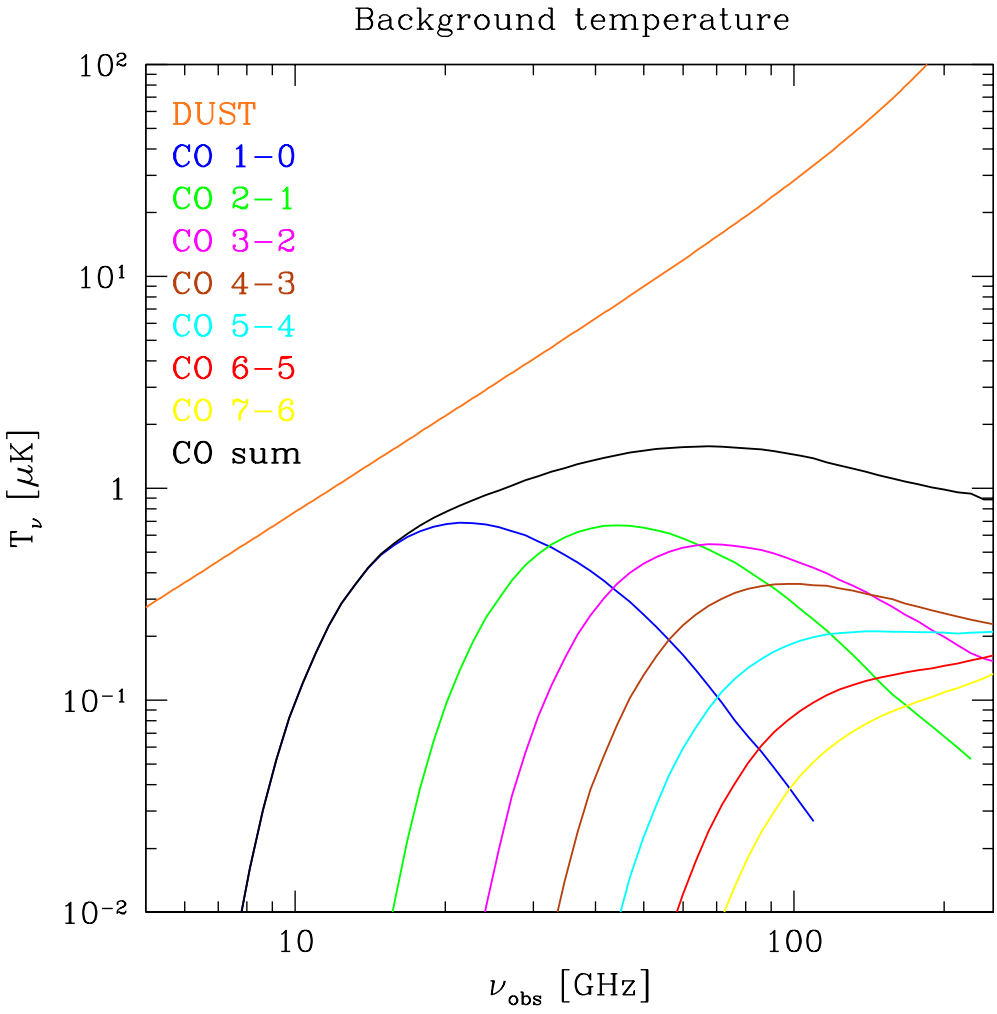

Figure 5.4: The contribution to the cosmic microwave background radiation (in temperature units) from the different CO lines and of their sum (black line), compared with the signal from dust (orange).

where $\tilde{L}_\nu = L_{\rm bol}/\nu$ and $L_{\rm bol}$ is the bolometric luminosity of the line. This expression shows the explicit dependence of the measured flux on the spectral resolution of the instrument. The amount of sources at a given frequency is also dependent on the spectral resolution, just because increasing the value of $\Delta\nu/\nu_{\rm obs}$ corresponds to probe larger volumes of the universe.

Given the source number counts, I can compute contribution of each line to

the cosmic microwave background temperature (Figure 5.4). The total emission of the CO lines is practically constant with frequency in the very broad $20 - 200$ GHz range. Its value is close to 1 μK and it is thousand times weaker than the present day uncertainties in the temperature of monopole according to COBE-FIRAS results (Fixsen & Mather 2002). The first CO line peaks at frequency $\sim 15 - 20$ GHz, corresponding to an emission redshift $z \simeq= 5 - 7$. The dust emission from merging galaxies contributes two or three times more at frequencies around $15 - 20$ GHz, increasing then upto a value of 100 μK at 200 GHz.

At 30 GHz, most of the contribution to the background in the first CO (1-0) transition is due to low-flux sources ($S_\nu = 10^{-4} - 10^{-2}$ mJy), which cannot be detected directly. But since their contribution to the correlated angular fluctuations is high, observations of the C_l's with different spectral resolutions provide one with a powerful tool to study the properties of the high-redshift population of CO-emitting galaxies and its evolution in time. I will discuss this in the next section.

5.3.2. Power spectrum of angular fluctuations

In this section I present the angular power spectra arising from the line emission of CO in the star-forming regions. Such a power spectrum is the sum of a Poisson term $C_l^{\rm P}$ and a correlation term $C_l^{\rm C}$.

The emission lines from carbon monoxide are associated with the rotational transitions between different states J. Their emission rest frequencies lie in the range $100 - 800$ GHz making them of particular interests for the low frequency experiments. Unfortunately, there are few observations of this molecule in the sample which we have selected: I was able to retrieve the full data set only for M82. I will use this latter object to calibrate the $\mathcal{R}$ ratio in most of my computations (see Table 5.1 for details), but I will show also the expected upper and lower limits in the amplitude of the signal, according to the values presented in Figure 5.1. The correlation terms of the angular power spectrum for each CO line are shown in Figure 5.5 at the three frequencies of PLANCK's LFI instrument and for the corresponding spectral resolution $\Delta\nu/\nu_{\rm obs} = 0.2$. As exptected, the signal at low frequencies is dominated by the lines corresponding to the first two transitions ($2 - 1$ and $1 - 0$), while higher states are important only at higher frequencies. This might appear paradoxical, since the SED of CO peaks at higher J. One has to bear in mind, however, that the power spectra are presented in temperature units and normalized to the CMB blackbody.

Another interesting aspect is that the emission from the first two transitions

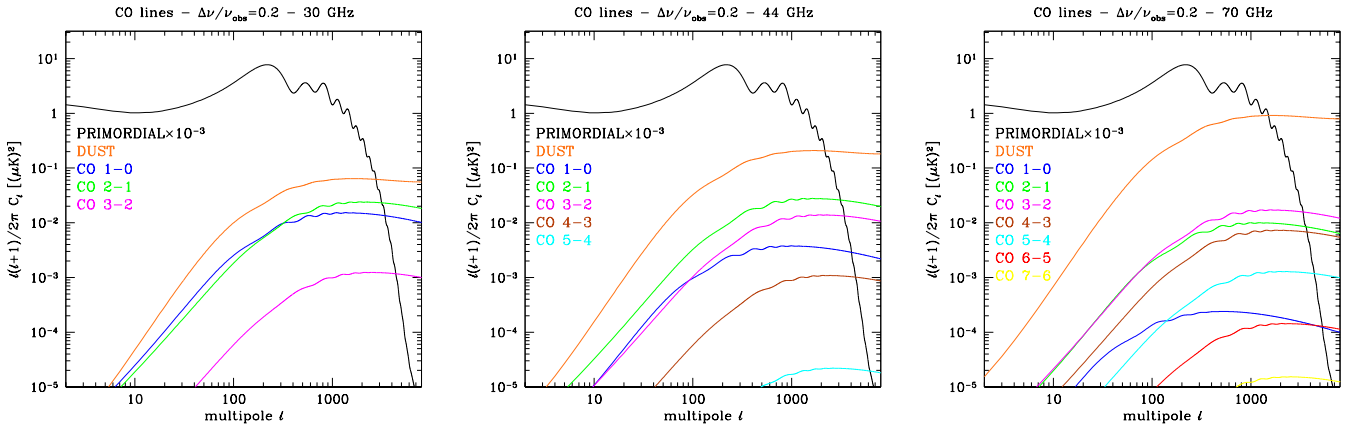

Figure 5.5: The correlation signal for the CO emission lines at the LFI frequencies and for a spectral resolution $\Delta\nu/\nu_{\rm obs} = 0.2$, using the $\mathcal{R}$ ratio from M82. The black line is the primordial signal of the CMB, the orange line is the signal from dust in merging star-forming galaxies (see Chapter 4). Other colors identifies the lines as indicated by the labels. The primordial signal (black solid line) has been divided by 1000.

of the CO might be slightly amplified by the contribution from CN, HCN, HNC and HCO^+. These molecules form in the same environment of CO and has a very similar structure. Their resonant frequencies are very close (within $\sim 20\%$) to the 115 and 230 GHz transitions of CO. Their signal is then summed to the CO, with a slight shift in frequency and redshift, which leads to a smoothing effect. The luminosity of such lines in nearby objects is typically $\sim 10\%$ of the CO lines (Baan et al. 2008).

As previously discussed, in the literature there are also several observations of high-redshift sub-millimeter galaxies. These objects are thought to be the result of very massive and gas-rich mergers, with very high star formation rates, of the order of 10^3 $M_\odot$/yr. According to Alexander et al. (2005a,b) around 40% of the sum-millimeter galaxies (SMG) population hosts an AGN, but these contribute only to 10-20% of the total energy output in the far-infrared (Pope et al. 2008). Tables 5.1-5.3 summarize the data collected from the literature about CO emission in these objects: the line luminosity in these objects is extremely high, even for the higher J transitions, but given also the high value of the star formation rates the resulting $\mathcal{R}$ does not change too much. In addition, these very luminous objects are also very rare and therefore they do not contribute significantly to the correlation term, which is due mainly to the most abundandant less bright objects.

5.3.2.1. Dependence on the spectral resolution

As shown in Section 5.2, the spectral resolution of the instrument is extremely relevant in the determination of the amplitude of this signal. This is one of the most interesting results of this work: I demonstrated analytically (Appendix B) that for smaller values of $\Delta\nu/\nu_{\rm obs}$ the amplitude of the correlation term is expected to grow until some threshold value, beyond which it reaches a convergence level and stays constant for even smaller $\Delta\nu/\nu_{\rm obs}$-s. This can easily be seen in Figure 5.6 for the CO (1-0) line: the amplitude of the correlation term gains more than one order of magnitude as the relative spectral width is decreased to 10^{-3}, but practically shows no change if this value is further reduced to 10^{-4}. On the other hand, the Poisson term (showed in dashed lines in the same figure) grows lineary with decreasing values of $\Delta\nu/\nu_{\rm obs}$: therefore the relative importance of the two terms changes as a function of the spectral resolution.

One should keep in mind, however, that the actual amplitude of the Poisson term considerably depends on the ability of the observing intruments to isolate and remove the bright individual sources. The bulk of the power in the

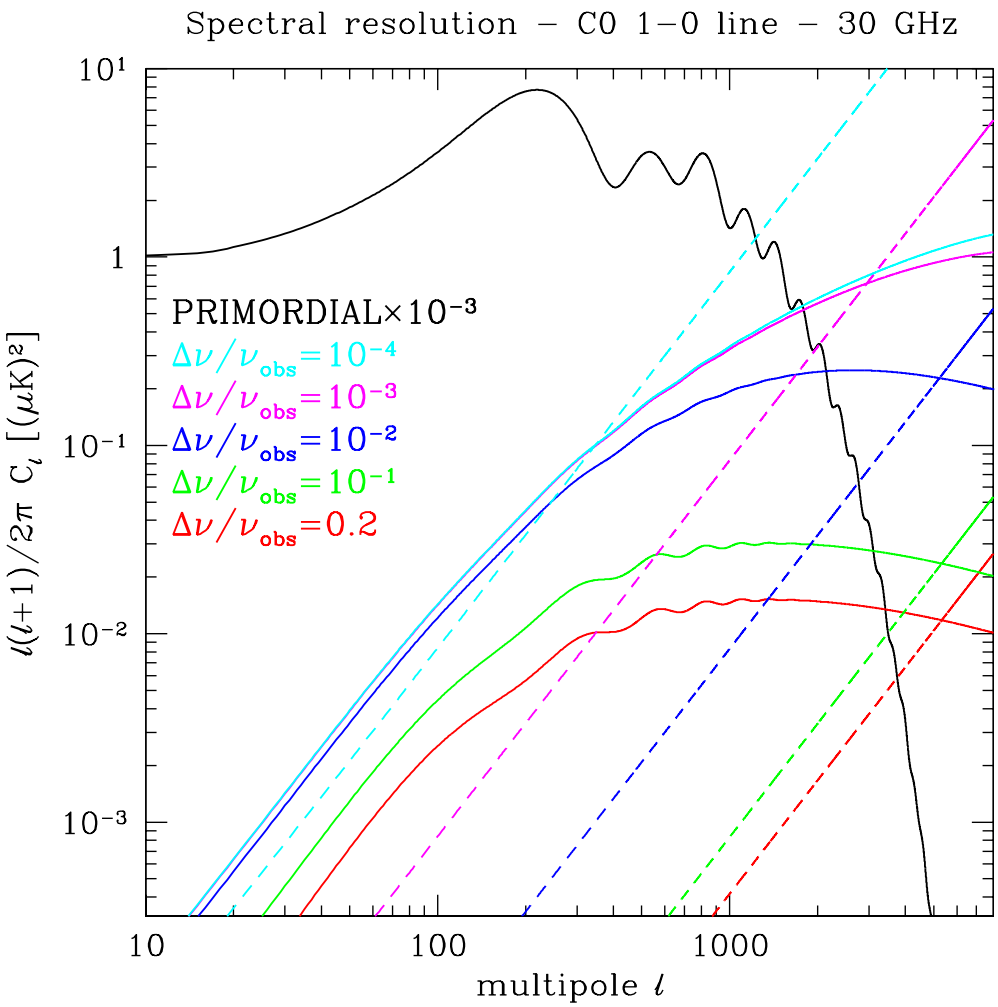

Figure 5.6: The change in amplitude of the correlation (solid line) and Poisson (dashed line) signal for the CO (1-0) line for different values of the spectral resolution $\Delta\nu/\nu_{\rm obs}$, at 30 GHz. The upper magenta and cyan solid lines are almost superimposed, meaning that for these resolutions the correlation signal already reached a constant value. The Poisson term, on the other hand, grows linearly with decreasing values of the spectral resolution. The primordial signal (black solid line) has been divided by 1000.

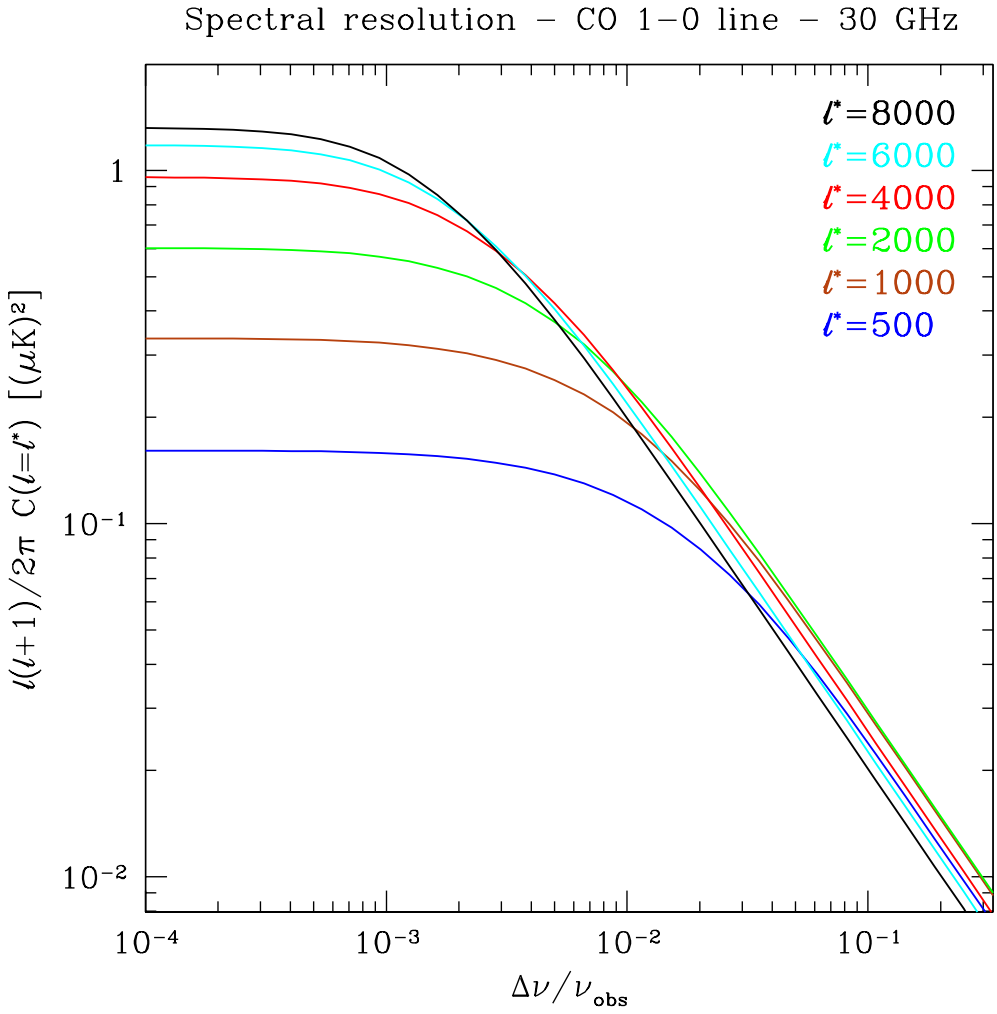

Figure 5.7: The dependence of the amplitude of the correlation signal on the spectral resolution of the observing instruments, for the CO (1-0) line at 30 GHz and for several values of the multipole index l.

amplitude of the Poisson term, infact, is generate by rare and bright sources. Such sources can be removed from the maps observing the same region with high enough angular resolution. This has practically no effect on the amplitude of the correlation term, which is generated by the abundant low-flux sources. This is clear from Table 5.4, where we compute the contribution to C_l^C and C_l^P of the CO (1-0) line at 30 GHz from different flux decades: with a 1-mJy

S_ν [mJy]	% of C_l^C	% of C_l^P
$S_\nu < 10^{-4}$	9	0
$10^{-4} \leq S_\nu < 10^{-3}$	23	1
$10^{-3} \leq S_\nu < 10^{-2}$	30	4
$10^{-2} \leq S_\nu < 10^{-1}$	26	25
$10^{-1} \leq S_\nu < 1$	11	53
$S_\nu > 1$	1	17

Table 5.4: Contribution to the amplitude of the correlation and Poisson terms of the CO (1-0) line from different intervals of flux of individual sources. The observing frequency is 30 GHz and the spectral resolution is 10^{-3}. The correlation term (C_l^C) gets the bulk of the power from the low-flux sources ($10^{-3}-10^{-2}$), while the Poisson (C_l^P) is mostly generated by sources brighter than 0.1 mJy.

flux cut-off one can drastically decrease the Poisson amplitude of 70%, while decreasing the correlation of 10% only.

The amplitude of the correlation term as a function of the spectral resolution is explored in more detail in Figure 5.7 for the same line: here I plot the value of the correlation term at different multipoles l (in the range $l = 500 - 8000$, corresponding to angular scales $\theta \simeq 20 - 1$ arcminutes). The signal grows uniformly and then reaches a plateau around a value $\Delta\nu/\nu_{\rm obs} \sim 10^{-3}$. The position of this convergency point depends both on the redshift of the line and on the multipole l: in general larger scales (smaller l) and higher redshift lines seem to converge earlier, i.e. for larger value of $\Delta\nu/\nu_{\rm obs}$.

5.3.2.2. Dependence on the observing channel

In this section I explore the amplitude of the signal in different observing frequencies. I consider the range of frequency $5 - 300$ GHz, which will be covered by several future experiments like SKA, PLANCK, ACT, SPT and ALMA. In Figure 5.8 I plot the ratio of the correlation signal to the primordial CMB signal at the fixed multipole $l = 2000$: here it appears clearly how the low frequency range ($\nu \lesssim 100$ GHz) is dominated by the CO emission, while at a higher frequency, the signal from dust is much stronger and dominates over the signal from the CII 158 μm line, which will be discussed in Section 5.4. The black solid line represents the sum from the CO lines, computed assuming that the cross-terms are negligible. This shows that in the frequency range $30 - 60$ GHz, the contribution from the first two CO lines might be the most

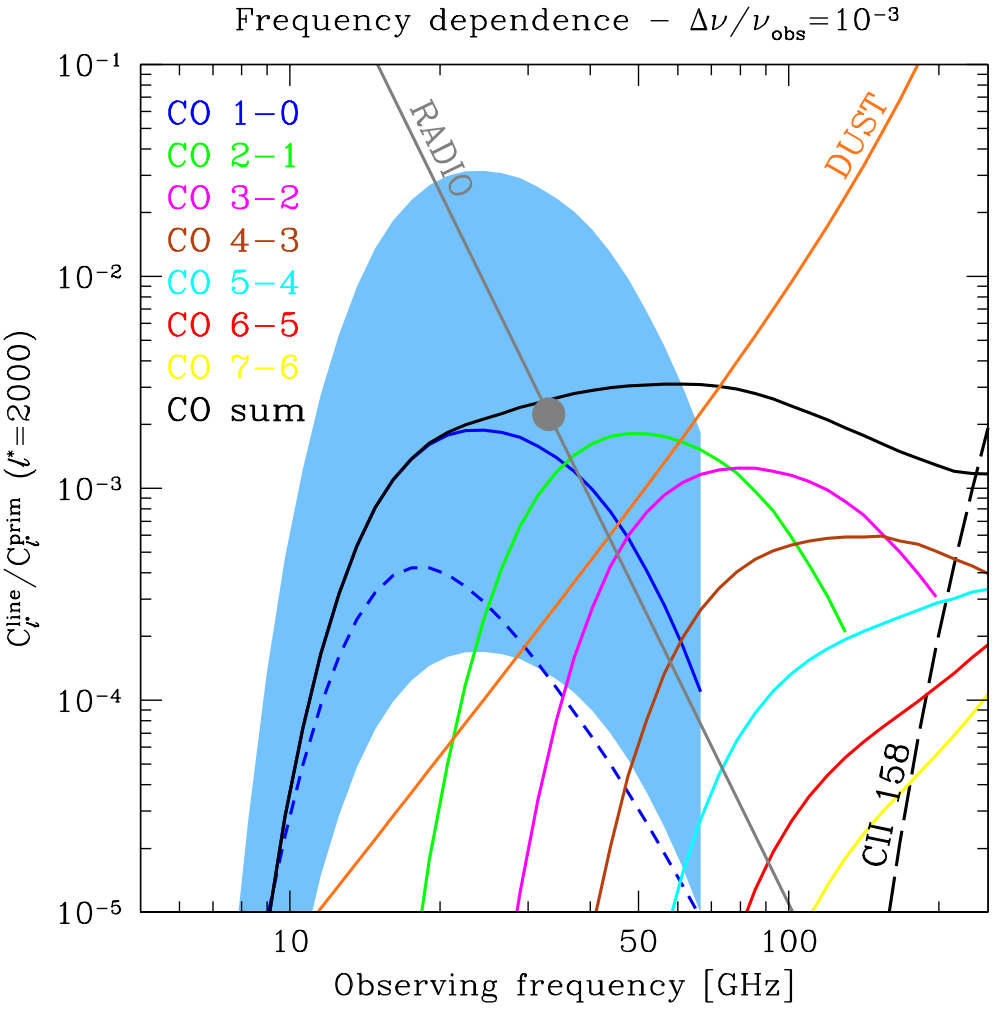

Figure 5.8: The ratio of the correlation signal from CO emission to the primordial CMB signal at $l = 2000$ as a function of frequency. The black solid line is the sum of the correlation from the CO lines, computed assuming the $\mathcal{R}$ ratio for M82. The dashed line is obtained with the model based on simple Press-Schechter distribution (see discussion at the end of Section 5.3.2.2). The contribution from dust emission in merging galaxies is showed with the orange line. The gray point is the Poisson at 33 GHz from radio sources, estimated from the de Zotti et al. (2005) model, assuming a cutoff of 10^{-4} Jy. The frequency dependence of this signal (gray line) has been computed assuming $S_\nu \propto \nu^{-\alpha}$ with $\alpha = 0.4$ (Toffolatti et al. 2005). The blue shaded regions around the curve for CO (1-0) represents the range of uncertainties in the correlation signal, according to the different value of $\mathcal{R}$ for the sample of objects in Figure 5.1 and Tables 5.1-5.3.

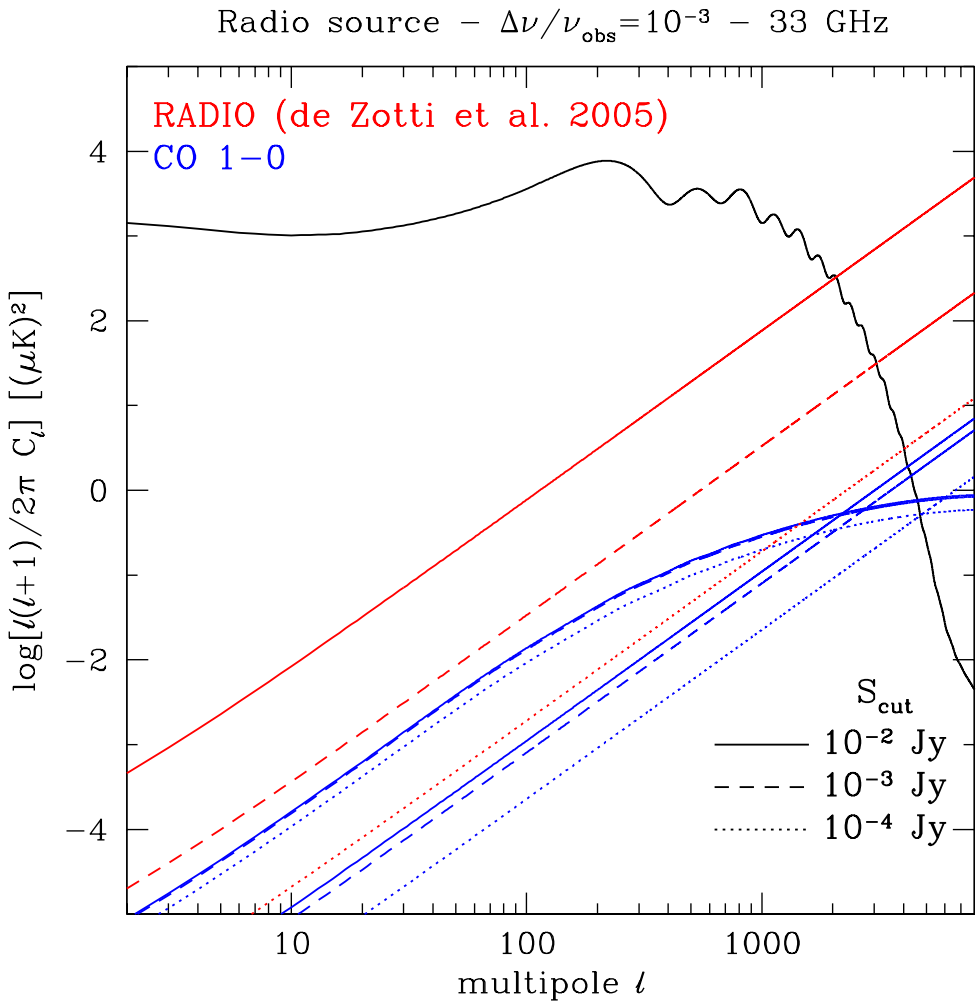

Figure 5.9: The contribution of the radio sources to the power spectrum at 33 GHz (red), compared with the CO (1-0) line (blue). Different flux cutoffs $S_{\rm cut}$ are applied: 10^{-2} Jy (solid lines), 10^{-3} Jy (dashed lines) and 10^{-4} Jy (dotted lines). The signal due to radio sources is very sensitive to this value, while the power in the CO is much less affected, being generated by sources with fluxes much lower than $S_{\rm cut}$.

important extragalactic foreground for the observations of the primordial angular fluctuations by present-day and future experiments. The blue shaded region around the curve corresponding to the first transition encloses the range

of possible values for the signal in this line. The upper limit of this curve is calibrated on the Antennae: this local merging has a very bright CO (1-0) line and a star formation rate comparable to M82. This result in a higher value of the $\mathcal{R}$ ratio and in a higher amplitude of the signal. As a lower limit, I used the IRAS 14378 galaxy. Similar ranges of uncertainty can be drawn around the other lines, according to the limits presented in Figure 5.1.

The contribution from dust emission in star-forming galaxies falls rapidly towards lower frequencies, where the CO signal seems to dominate. However, in this range, the foregrounds from compact radio sources (including AGN, quasars, BL Lac objects, afterglows of gamma ray bursts etc., see e.g. de Zotti et al. 2005) is very relevant. Unfortunately, the clustering properties of such sources are very poorly known, though several authors showed that the Poisson power is likely to be largely dominant over the correlation one (Toffolatti et al. 1998; González-Nuevo et al. 2005). The Poisson power, however, can be strongly reduced if the bright sources are excised from the map according to some flux cutoff. I show this in Figure 5.9: here I consider the radio source counts at 33 GHz, from the model of de Zotti et al. (2005). Integrating the counts I can estimate the Poisson contribution to the power spectrum. I compute it for several values of the flux cutoff and I find that the signal from the radio sources can be reduced to the level of the CO (1-0) line emission if a $S_{\rm cut} \simeq 10^{-3} - 10^{-4}$ Jy is applied. The same cut does not affect the CO contribution significantly, since at this frequency both its Poisson and correlation term are generated by much weaker sources. There are two important caveats that have to be considered here. First: the main limitation to such cleaning procedure is the confusion noise. To reduce the radio signal to the CO level we need to apply a flux cutoff of the order of $10^{-3} - 10^{-4}$ Jy. According to the counts curve of de Zotti et al. (2005) this corresponds to a density of $\sim 20 - 200$ sources per square degree. Therefore the confusion noise should not be an issue, even at very low fluxes. Second: as we mentioned above, the correlation term of the radio sources is considered negligible compared to the Poisson power. This is true, however, if the sources are not subtracted down to very low values of the flux (Toffolatti et al. 1998). In this case the contribution of correlation from weak, unresolved objects might become important and it is necessary to have an accurate modelling of their clustering.

To conclude this section, I recompute the correlation term for the CO (1-0) line using an alternative approach, based on a simple Press-Schechter distribution of the star-forming haloes emitting in CO lines. This gives a parallel constrain that can be compared with the estimates of the merging model. in particular at the lower frequencies corresponding to the higher redshifts.

Let us assume first that the star formation rate in haloes scale with their mass

$$\dot{M}_\star = \mathcal{C}(z) \cdot M, \tag{5.7}$$

the factor (z) is obtained normalizing to the cosmic star formation rate density $\dot{\rho}_\star(z)$

$$\dot{\rho}_\star(z) = \int dM \frac{dn}{dM} \mathcal{C}(z) M. \tag{5.8}$$

The integration must be limited to the haloes which are actually able to form stars. I use the fit to $\dot{\rho}_\star$ proposed by Hernquist & Springel (2003) as derived from a set of cosmological simulations up to very high redshifts. These simulation were performed with a value of $\sigma_8 = 0.9$, which is sensibly higher than the value adopted in this thesis ($\sigma_8 = 0.74$). Therefore I rescale their fit taking into account this difference, before computing the normalization in Equation 5.8. The dashed line in Figure 5.8 shows the result obtained using this simple model: the estimate is a factor of a few below the one obtained with the merging approach. The dependence of this normalization on the actual value of σ_8 might open interesting possibilities of estimating the value of such a parameter from the amplitude of the signal.

5.4. Angular fluctuations from fine-structure lines of atom and ions

As I mentioned in the introduction, the first generation of stars enriched the interstellar medium with significant amounts of metals, mainly carbon, oxygen and nitrogen. The fine-structure transitions of these species are characterized by higher resonant frequencies with respect to the CO molecule. Therefore, their emission lines are more relevant for the high-frequency instruments, like PLANCK HFI, SPT, ACT and ALMA.

In a earlier paper, Suginohara et al. (1999) presented estimations of the collisional emission in fine-structure lines of these species. Assuming a fraction of 10^{-2} of the solar abundance for those species, and that roughly half of them are in environments with super-critical densities, they found that this emission should introduce an average distortion at the level of 10^{-6}, whereas at scales of 1 h^{-1}Mpc the relative intensity fluctuations should be a factor of 10 larger.

In this section I compute the signal due to the clustering of the sources responsible for the line emission. I will repeat the approach used for the CO lines. To calibrate the $\mathcal{R}$ ratio for the fine-structure transitions of atoms and ions I

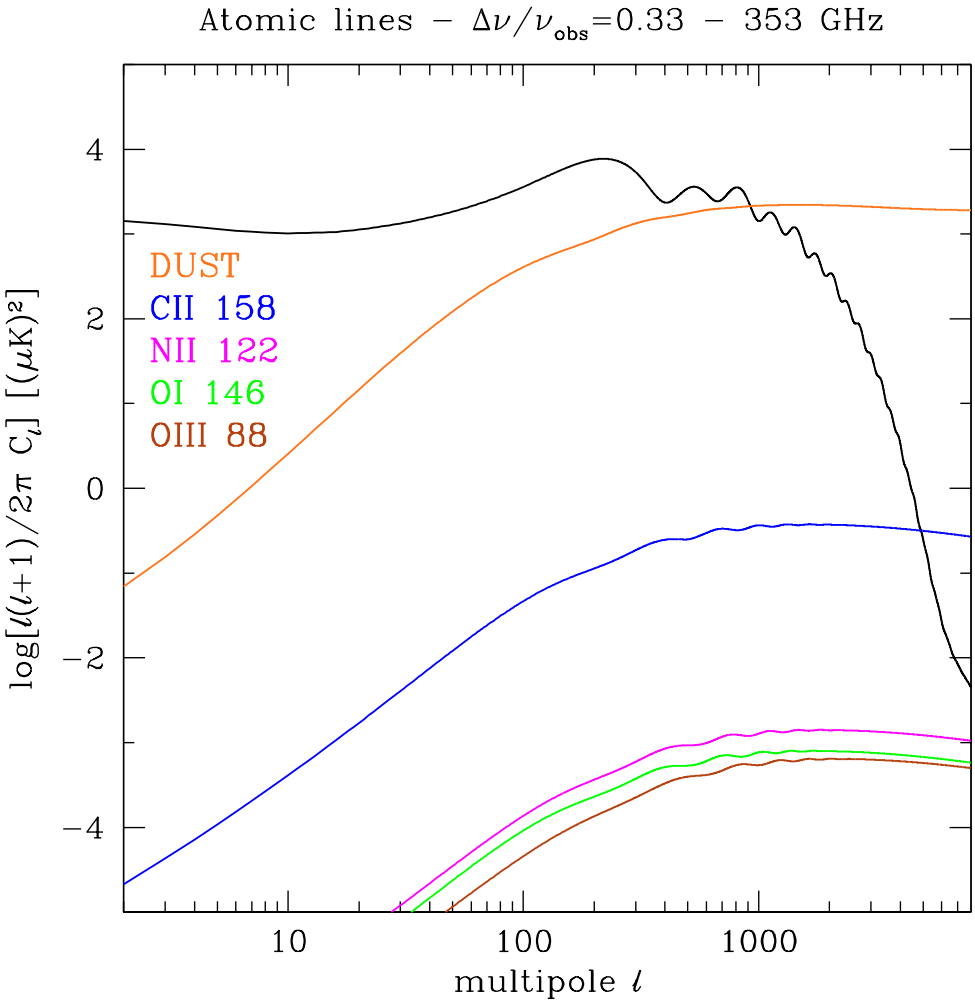

Figure 5.10: The correlation signal of the most significant atomic emission lines, for a spectral resolution $\Delta\nu/\nu_{\rm obs} = 0.33$ at 353 GHz, corresponding to one of the PLANCK HFI's detectors. The black line is the primordial signal of the CMB, the orange line is the signal from dusty merging star-forming galaxies. Other colors identifies the lines as indicated by the labels (the number refers to the rest wavelength in μm). See Table 5.5 for details.

use the results of Malhotra et al. (2001), who have observed 60 star-forming galaxies with ISO-LWS. They especially selected the objects with angular size smaller than the instrument beam, therefore the line fluxes presented in their

Species	Wavelength [μm]	Average $\mathcal{R}$
CII	158	$\mathbf{6.0 \times 10^6}$
OI	145	$\mathbf{3.3 \times 10^5}$
NII	122	$\mathbf{7.9 \times 10^5}$
OIII	88	$\mathbf{2.3 \times 10^6}$
OI	63	$\mathbf{3.8 \times 10^6}$
NIII	57	$\mathbf{2.4 \times 10^6}$
OIII	52	$\mathbf{3.0 \times 10^6}$

Table 5.5: Average $\mathcal{R}$ for the 7 transitions of the sample from Malhotra et al. (2001).

paper refers to the total line emission from such galaxies. As for the low-redshift sample of CO lines, we obtain the FIR luminosities of these objects from the *IRAS revised bright galaxies sample* (Sanders et al. 2003). For each of the 7 species presented in their work, I compute the geometric average of the $\mathcal{R}$ ratio in the sample as

$$\bar{\mathcal{R}} = \left[\prod_{i=1}^{N} \mathcal{R}_i\right]^{1/N} . \tag{5.9}$$

The resulting numbers are listed in Table 5.5.

In Figure 5.10 I show the correlation signal of these lines at 353 GHz and for a spectral resolution $\Delta\nu/\nu_{\rm obs} = 0.33$, close to the performance of one of PLANCK HFI's channels. In the same Figure I show also the correlation term from star-forming merging dusty galaxies computed in Chapter 4: it is clear that this signal is still the dominant one. Also in this case, however, it is possible to increase the amplitude of the correlation term by using very good spectral resolutions. This makes the angular fluctuations in the CII line emission not negligible compared with the continuum emission from dust in merging star forming galaxies and its different behaviour versus $\Delta\nu/\nu_{\rm obs}$ might make it detectable by future high-resolution exeperiments, like ALMA.

5.4.1. Comparison with similar works

An estimate of the fluctuations arising from atomic line emission was presented by Suginohara et al. (1999): when looking at the CII line at $z = 10$, my results predict emission amplitudes that are significantly (a factor of $\sim 10^2$) smaller than theirs. Most of this disagreement is due to the different value adopted for the amount of atoms emitting in the line (which depends on the

assumed metallicity and ionization/excitation fractions), while having a different set of cosmological parameters introduces an offset of a factor of a few. In this work, the actual abundance of atoms in the upper state is provided by the calibration of the model with observational data.

Basu et al. (2004) analyzed the effect on the CMB primordial spectrum induced by the resonant scattering of heavy elements in the intergalactic gas, expelled by supernova explosions, galactic winds and jets. They demonstrated that this effect is the sum of a damping of the original fluctuations plus the generation of new anisotropy. They obtained a very simple analytical expression for the change induced in the angular power spectrum at small scales

$$\delta C_l \simeq -2\tau_{\rm scat} C_l, \tag{5.10}$$

where $\tau_{\rm scat}$ is the scattering optical depth of the line. The linear scaling of δC_l with the optical depth produces quite strong effect even for small value of τ. In Figure 5.11 I plot the δC_l for the third transition of CO at 70 GHz and compare it with the correlation signal of the emission from the same line. For 1% solar abundance, the scattering optical depth of this line at this frequency is $\tau_{3-2} = 1.94 \times 10^{-4}$. It therefore introduces a change in the primordial power spectrum of the order of $\sim 4 \times 10^{-4}$. This term, however, dominates at large scales, while it drops towards higher multipoles, following the decrease of the primordial spectrum, where the correlation signal is more important.

More recently, Hernández-Monteagudo et al. (2007, 2008) considered the pumping effect of the ultraviolet background on the OI 63 μm line and the resulting distortion on the CMB. They computed the correlation signal associated with the clustering of the first star-forming objects: the amplitude they found is on the level of 10^{-6} $(\mu{\rm K})^2$ and it is therefore lower than the signal described here. However, this effect would show up at higher frequencies ($\nu \sim 400 - 700$ GHz), well within the spectral coverage of ALMA, whose sensitivity should be able to put constraints on this effect. I remark that the physical environments where both the collisional emission and the UV-induced emission take place are very similar, and therefore both effects constitute different probes for the same scenarios.

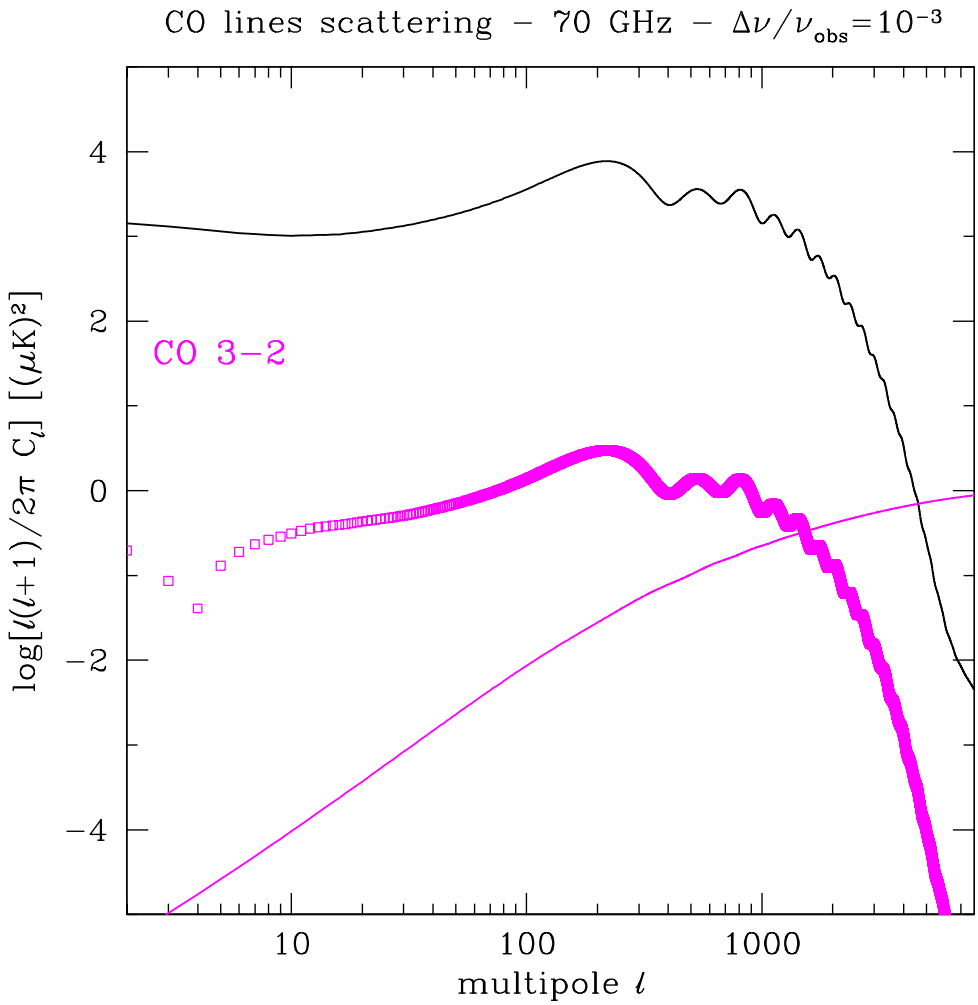

Figure 5.11: The effect of the scattering of the CO (3-2) line at 70 GHz (squares), according to the model of Basu et al. (2004). The solid lines is the correlation term from the emission in the same transition, for a spectral resolution $\Delta\nu/\nu_{\rm obs} = 10^{-3}$.

– No tengo más, señores, que deciros de mi historia; la cual, si es agradable y peregrina, júzguenlo vuestros buenos entendimientos; que de mí sé decir que quisiera habérosla contado más brevemente, puesto que el temor de enfadaros más de cuatro circunstancias me ha quitado de la lengua.

Miguel de Cervantes, El ingenioso Hidalgo Don Quijote de la Mancha

6 Concluding remarks

In this thesis I presented a simple model to determine the space density distribution of merging star-forming haloes as a function of their star formation rate. I used the extended Press-Schechter formalism (Lacey & Cole 1993) to compute the merger rate and introduced a characteristic time of star formation for each merger episode, derived from numerical simulations of merging gas-rich disk galaxies. Using the Kennicutt relation, which relates the infrared luminosity of a given object to its star formation rate, I then derived the infrared luminosity of the merging population.

I have assumed a dust emission model based on recent observations of bright infrared galaxies by SCUBA (Blain et al. 2002) depending on two free parameters: the emissivity index β and the dust equilibrium temperature $T_{\rm dust}$. I corrected the spectral energy distribution taking into account the presence of the CMB thermal bath which becomes non-negligible for high-redshift objects.

With these ingredients, I built estimates for several observables and I calibrated the model in order to obtain a good agreement with available data: the Madau plot for cosmic star formation history and the source counts measured by SCUBA. Furthermore, the results are within the limits imposed by COBE-FIRAS observations of the Cosmic Infrared Background. The calibration was obtained acting on the main free parameters of the model: the two spectral parameters β and $T_{\rm dust}$ and the escape fraction of ionizing photons which allows for correction to the Kennicutt relation to limit the luminosity of the most

abundant less massive objects.

This merging model is able to make predictions for the power spectrum of the angular fluctuations: such predictions are close to previous estimates, both in amplitude and the redshift range where anisotropies are generated (Haiman & Knox 2000; Song et al. 2003; González-Nuevo et al. 2005; Toffolatti et al. 2005) and confirm that the dust emission in merging star-forming galaxies is a powerful foreground for the high frequency channels of PLANCK, ACT and SPT. A simple estimate on the amount of intergalactic dust expelled by galaxy winds and AGN activity shows that it leaves a negligible signature at the low multipoles of the spectrum.

The same model has then been applied to estimate the impact that emission on molecular and atomic and ionic lines have on the angular power spectrum of the CMB. I have placed particular emphasis on the emission of CO rotational lines, since their effect is significant in the 20−60 GHz frequency range, although I have also considered the collisional emission of lines corresponding to species like CII, OI, NII and OIII.

If the star formation activity follows the halo merging history, then the spatial distribution of molecules and metals should closely resemble that of the haloes where they were produced and therefore the emission pattern generated by these molecules and metals should show similar clustering properties. The advantage of looking at the emission of particular lines is that each observing frequency is probing a given redshift shell, whose width is determined by the experimental spectral resolution ($\Delta z/z \sim \Delta\nu/\nu_{\rm obs}$). Furthermore, I demonstrated that the amplitude of the correlation signal increases with better spetral resolution (down to a threshold value $\Delta\nu/\nu_{\rm obs} \simeq 10^{-3}$).

This is a very interesing result, since all other signals that contribute in similar spectral ranges (dust far-infrared emission, as well as synchrotron radiation, intrinsic CMB, etc) are insensitive to the changes in the spectral resolution. This provides future experiments with a powerful tool to distinguish between the fluctuations in the line emission from all the other continuum sources *and* an efficient way to perform tomography of the reionization at different frequency bands.

Due to the large number of uncertainties when building a theoretical model for the collisional emission on molecular, atomic and ionic lines, I have used existing measurements at low and high redshift in order to calibrate the model. I have assumed that the star formation rate scales linearly with the luminosity in the various lines considered and I have collected a sample of local and high-redshift objects of different nature (including local mergings, bright infrared

sources, AGN, QSOs and radiogalaxies) to calibrate this proportionality. I have considered, for every transition, a broad range of possible values to give an upper and lower limit estimate of the expected amplitude of the fluctuations.

The results show that CO emission is already larger than dust emission in the frequency range $10 - 70$ GHz if $\Delta\nu/\nu = 10^{-3}$. Moreover, if one makes use of the different behaviour of the CO signal versus the observing spectral resolution, then it should be possible to project out continuum signals such as CMB, radio and dust emission with further confidence. In particular, the frequency interval ranging from 30 to 50 GHz is of special interest for the first three CO rotational lines, since they probe the redshift range $z \simeq 6-10$, crucial for our understanding of reionization. Atomic and ionic emission lines are more important at higher frequency, but only the CII 158 μm gives a non-negligible contribution to the amplitude.

This brings me to the conclusion that the emission on CO and CII lines studied in this thesis provides a new window to reionization, constituting a bridge between the low frequency observations, pursuing the HI 21 cm fluctuations in the radio range, and the high frequency observations targetting fine-structure lines in metals and ions like CII, OI or OIII (Basu et al. 2004; Hernández-Monteagudo et al. 2007, 2008). These three windows should allow one to perform tomography of the same cosmological epoch, but should be affected, in general, by very different contaminants and systematics. Therefore, the combination of these three perspectives should provide a consistent picture of an epoch that, to date, has remained hidden to observations.

A

The angular correlation of dust emission from star forming haloes

In this appendix I will follow the approach given by Hernández-Monteagudo et al. (2006).

A.1. Model of measured intensity fluctuations

When considering sources that are much smaller than the PSF of the observing experiment, it is convenient to explicitly introduce the finite size of the beam and the frequency response of the detector(s). In what follows, the observing experiment will be characterized by a Point Spread Function (PSF) $B(\mathbf{n})$ ($\mathbf{n}$ denoting a direction on the sky) and a frequency response function $\phi(\nu', \nu)$, with ν the central (observing) frequency. For simplicity, I shall assume that both functions have a Gaussian shape, so that

$$B(\mathbf{n}) = \exp\left[-\frac{\theta^2}{2\sigma_{\rm b}^2}\right], \tag{A.1}$$

$$\phi(\nu', \nu) = \exp\left[-\frac{(\nu' - \nu)^2}{2\sigma_\nu^2}\right]. \tag{A.2}$$

The integral over the PSF and the spectral response will be regarded as a normalization factor $\mathcal{N}$:

$$\begin{aligned}\mathcal{N} &\equiv \int d\mathbf{n}\, B(\mathbf{n})\, d\nu'\, \phi(\nu', \nu) = \\ &= (\sqrt{2\pi}\sigma_{\rm b})^2 \sqrt{2\pi}\sigma_\nu \equiv \Omega_{\rm beam}\, \Delta\nu. \end{aligned} \tag{A.3}$$

The brightness intensity fluctuations introduced by the dust emission in haloes can be then written as

$$\begin{aligned}\Delta I_\nu &= \frac{1}{\mathcal{N}} \int_0^{r_{\rm LSS}} dr\, d\mathbf{n}\, B(\mathbf{n})\, d\nu'\, \phi(\nu', \nu) \\ &\quad \times \sum_j j_{\nu(1+z[r])}\, W(\mathbf{x}_j - \mathbf{r})\, a^3(r), \end{aligned} \tag{A.4}$$

where r denotes the physical distance from the observer and the index j sweeps over all star forming haloes in the universe, $\mathbf{x}_j$ being their positions; $j_{\nu(1+z[r])}$ denotes the emissivity at the center of the halo placed at $\mathbf{x}_j$, and $W(\mathbf{x}_j - \mathbf{r})$ is the dust profile and accounts for the dilution of the emissivity as the distance to the halo center increases. Note that due to expansion-induced redshift, the experiment will be sensitive to the emissivity at a frequency $\nu(1+z[r])$. Finally, $a(r) \equiv 1/(1+z[r])$ is the scale factor at the epoch given by r, and the a^3 factor accounts for the dilution of the intensity as the universe expands. The sum over j can be replaced by a volume integral over the star-forming halo density $n(\mathbf{x})$:

$$\begin{aligned}\Delta I_\nu &= \frac{1}{\mathcal{N}} \int_0^{r_{\rm LSS}} dr\, d\mathbf{n}\, B(\mathbf{n})\, d\nu'\, \phi(\nu', \nu) \\ &\quad \times \int d\mathbf{x}\, n(\mathbf{x})\, j_{\nu(1+z[r])}\, W(\mathbf{x} - \mathbf{r})\, a^3(r). \end{aligned} \tag{A.5}$$

Next I integrate in $\mathbf{n}$ and ν, in order to obtain the contribution of all sources within the volume probed by the PSF and the frequency response of the instrument. The vector sweeping this volume will be $\mathbf{y}$: I use the relation $d\nu' = (\nu/r)\, dy$, and the spectral response ϕ becomes a function of y, with the maximum at $y = r$.
With this in mind, the argument of the function W is now $\mathbf{x} - \mathbf{y}$, resulting in

$$\begin{aligned}\Delta I_\nu &= \frac{1}{\mathcal{N}} \int_0^{r_{\rm LSS}} dr \int d\mathbf{x}\, n(\mathbf{x}) \left(\frac{\nu}{r^3}\right) r^2\, d\mathbf{n}\, dy\, \phi(y, r)\, j_{\nu(1+z[r])} \\ &\quad \times W(\mathbf{x} - \mathbf{y})\, a^3(r) = \end{aligned}$$

$$= \frac{1}{\mathcal{N}} \int_0^{r_{\rm LSS}} dr \left(\frac{\nu}{r^3}\right) \frac{L_{\nu(1+z[r])}}{4\pi} a^3(r) \times \int d\mathbf{x}\, n(\mathbf{x}) V(\mathbf{x}-\mathbf{r}). \quad \text{(A.6)}$$

In this case, the window function $V(\mathbf{x}-\mathbf{r})$ corresponds to the cosmological volume sampled by the finite size of the PSF and the frequency response. The integral on $\mathbf{x}$ corresponds to a convolution that allows us to rewrite the last equation as

$$\Delta I_\nu = \frac{1}{\mathcal{N}} \int_0^{r_{\rm LSS}} dr \left(\frac{\nu}{r^3}\right) \frac{L_{\nu(1+z[r])}}{4\pi} a^3(r) \times \int \frac{d\mathbf{k}}{(2\pi)^3}\, n_{\mathbf{k}} V_{\mathbf{k}}\, e^{-i\mathbf{kr}}. \quad \text{(A.7)}$$

The Fourier modes of the halo density and the window V are given by $n_{\mathbf{k}}$ and $V_{\mathbf{k}}$, respectively. Using my model for the PSF and the frequency response, the latter can be written, for each r, as

$$V_{\mathbf{k}} = \left(\sqrt{2\pi}\sigma_{\rm b} r\right)^2 \sqrt{2\pi}\,(r/\nu)\,\sigma_\nu\, e^{-\frac{k^2 r^2 \sigma_{\rm b}^2}{2}} e^{-\frac{k^2(\sigma_\nu r/\nu)^2}{2}}. \quad \text{(A.8)}$$

The Fourier modes of the halo density will depend on the halo clustering properties, and will be characterised below. I can introduce the expression for $V_{\mathbf{k}}$ into Equation (A.7), and this will remove the dependence on the normalization factor $\mathcal{N}$

$$\Delta I_\nu = \int_0^{r_{\rm LSS}} dr \frac{L_{\nu(1+z[r])}}{4\pi} a^3(r) \times \int \frac{d\mathbf{k}}{(2\pi)^3}\, n_{\mathbf{k}}\, e^{-\frac{k^2 r^2 \sigma_{\rm b}^2}{2}}\, e^{-\frac{k^2(\sigma_\nu r/\nu)^2}{2}}\, e^{-i\mathbf{kr}}. \quad \text{(A.9)}$$

Further, if we are interested in scales larger than the beam size, the latter expression can be further simplified to

$$\Delta I_\nu \simeq \int_0^{r_{\rm LSS}} dr \frac{L_{\nu(1+z[r])}}{4\pi} a^3(r)\, n(\mathbf{r}), \quad \text{(A.10)}$$

which is simply an integral of the halo luminosity weighted by the halo density along the line of sight. From this expression, it is easy to see that the correlation properties of ΔI_ν will depend on the correlation properties of the star forming

haloes.
There are, however, two more aspects that need to be taken into account, namely the peculiar velocities of the star forming regions and the gravitational redshift imprinted on the emitted photons on the way to the observer. The former can be observed by simply imtroducing a Doppler term (containing the peculiar velocity of the sources) in the integrand of Equation (A.10), the latter by explicitely writing the time-varying potential fluctuations in such integral. Thus, I rewrite Equation (A.10) as

$$\begin{aligned}\Delta I_\nu &= \int_0^{r_{\rm LSS}} dr \left[\left(1+\frac{\mathbf{v}\cdot\mathbf{n}}{c}\right)\frac{L_{\nu(1+z[r])}}{4\pi}\,a^3(r)\,n(\mathbf{r})\right. \\ &\quad \left. +2\left(\int_r^{r_{\rm LSS}} dr'\,\left(1+\frac{\mathbf{v}'\cdot\mathbf{n}}{c}\right)\frac{L_{\nu(1+z[r'])}}{4\pi}\,a^3(r')\,n(\mathbf{r}')\right)\frac{\dot\phi(r)}{c}\right].\end{aligned} \tag{A.11}$$

In this new expression, the term $\dot\phi/c$ accounts for the time derivative of the potential, whereas the dot product $\mathbf{v}\cdot\mathbf{n}$ provides the component of the source peculiar velocity along the line of sight. If I now argue that we are interested in scales where perturbations are still in the linear regime, then I may retain only the first order of the potential, velocity and density fluctuations that give rise to ΔI_ν:

$$\begin{aligned}\Delta I_\nu &= \text{const} \\ &\quad +\int_0^{r_{\rm LSS}} dr\left[\frac{\mathbf{v}\cdot\mathbf{n}}{c}\,\bar n(r)\frac{L_{\nu(1+z[r])}}{4\pi}\,a^3(r)+2\frac{\dot\phi}{c}\,\bar I_\nu^{\rm dust}(r)\right] \\ &\quad +\int_0^{r_{\rm LSS}} dr\,\delta n(\mathbf{r})\frac{L_{\nu(1+z[r])}}{4\pi}\,a^3(r)+\mathcal{O}(\delta^2),\end{aligned} \tag{A.12}$$

where the average dust intensity $\bar I_\nu^{\rm dust}(r)$ is defined as

$$\bar I_\nu^{\rm dust}(r)=\int_r^{r_{\rm LSS}} dr'\,L_{\nu(1+z[r'])}\,a^3(r')\,\bar n(r'). \tag{A.13}$$

This equation shows that, to the first order, source peculiar velocities and potential fluctuations will couple to the average source number density $\bar n(r)$, and the correlation properties of the measured intensities will be ruled by the correlation functions of each of the three quantities: gravitational potentials, peculiar velocities and source number overdensities $\delta n(\mathbf{r})$. We shall find, however, that the latter will be dominant over the first two.

A.2. Correlation of the measured intensity fluctuations

I first rewrite the change in brightness intensity in terms of an integral of quantities expressed with respect to comoving coordinates

$$\Delta I_\nu = \text{const} \;+\; \int_0^{r_{\rm LSS}} dr \left[\frac{\mathbf{v}\cdot\mathbf{n}}{c}\, a(r)\, \bar{n}(r) \frac{L_{\nu(1+z[r])}}{4\pi} + 2\,\frac{\dot{\phi}}{c}\, \bar{I}_\nu^{\rm dust}(r) \right] + \int_0^{r_{\rm LSS}} dr\, a(r)\, \delta n(\mathbf{r}) \frac{L_{\nu(1+z[r])}}{4\pi} + \mathcal{O}(\delta^2). \tag{A.14}$$

The comoving number density absorbs the $a(r)^3$ factor, and a new $a(r)$ factor appears from the line element. Note that peculiar velocities are *proper* velocities. Next, I express the star-forming halo number density as an integral over a luminosity distribution function

$$\bar{n}(\mathbf{x}) = \int dL_{\nu(1+z[x])} \frac{dn}{dL_{\nu(1+z[x])}}. \tag{A.15}$$

Finally, I decompose $dn/dL_{\nu(1+z[x])}$ as an integral over the haloes of different masses contributing to the same luminosity interval

$$\frac{dn}{dL_{\nu(1+z[x])}} = \int dM\, \frac{dn}{dM}\, G(M, L_{\nu(1+z[x])}). \tag{A.16}$$

In this equation, the function $G(M, L_{\nu(1+z[x])})$ provides the fraction of haloes present in the mass interval $[M, M+dM]$ (given by the Press-Schechter mass function dn/dM) that have recently experienced a major merger, and hence have given rise to significant star forming activity (see Chapter 2.1). I then write the spatial correlation function of haloes in the mass range $[M, M+dM]$, $n_{\rm h}(M, \mathbf{x})$,

$$\begin{aligned} \langle n_{\rm h}(M_1, \mathbf{x}_1)\, n_{\rm h}(M_2, \mathbf{x}_2)\rangle = {} & \frac{dn}{dM}(M_1, \mathbf{x}_1)\, \frac{dn}{dM}(M_2, \mathbf{x}_2) \\ & + \frac{dn}{dM}(M_1, \mathbf{x}_1)\, \delta_D^3(\mathbf{x}_1 - \mathbf{x}_2)\, \delta_D(M_1 - M_2) \\ & + \frac{dn}{dM}(M_1, \mathbf{x}_1) \frac{dn}{dM}(M_2, \mathbf{x}_2) \\ & \times\; b(M_1, z[x_1])\, b(M_2, z[x_2])\, \xi_{\rm m}(\mathbf{x}_1 - \mathbf{x}_2). \end{aligned} \tag{A.17}$$

The symbol δ_D stands for Dirac delta and $b(M, z)$ is the mass and redshift dependent bias factor that relates the halo and the matter linear correlation function $\xi_{\rm m}$ (Mo & White 1996). The first term on the right hand side accounts for the Poissonian fluctuations in the number counts, whereas the second term accounts for the dependence of the halo number density on the environment. Having this present, one easily finds that the angular correlation function of the intensity fluctuations can be written as

$$\langle \Delta I_\nu(\mathbf{n}_1)\, \Delta I_\nu(\mathbf{n}_2)\rangle = \sum_l \frac{2l+1}{4\pi} \left(C_l^{\rm P} + C_l^{\rm C}\right) P_l(\mathbf{n}_1 \cdot \mathbf{n}_2), \tag{A.18}$$

with $P_l(\mathbf{n}_1 \cdot \mathbf{n}_2)$ the Legendre polynomia of order l and where $C_l^{\rm P}$ and $C_l^{\rm C}$ are the Poissonian and the correlation terms of the l-th angular power spectrum multipole. $C_l^{\rm P}$ is given by

$$C_l^P = \frac{2}{\pi} \int dk\, k^2 \left| \int_0^{r_{\rm LSS}} dr\, a(r)\, j_l(kr) \frac{\sqrt{n\mathcal{L}^2}}{4\pi} \right|^2 \tag{A.19}$$

with

$$n\mathcal{L}^2 = \int dL_\nu \frac{dn}{dL_\nu} L_\nu^2. \tag{A.20}$$

In practice, this expression is equivalent to

$$\tilde{C}_l^P = \int dS_\nu \frac{dN}{dS_\nu} S_\nu^2 \tag{A.21}$$

where dN/dS_ν is the angular number density of sources per spectral flux unit. Due to its simplicity, I preferred to use Equation (A.21) in my computations. The correlation term can be expressed in terms of a k-space integral of the initial scalar metric power spectrum $P_\psi(k)$ times a squared transfer function, as in Seljak & Zaldarriaga (1996),

$$C_l^{\rm C} = \frac{2}{\pi} \int k^2 dk\, P_\psi(k)\, |\Delta_l(k)|^2, \tag{A.22}$$

with the transfer function $\Delta_l(k)$ given by

$$\begin{aligned} \Delta_l(k) \;=\; & \int_0^{r_{\rm LSS}} dr\, j_l(kr) \left[S_1(r)\, \delta_k + \frac{dS_2(r)}{dr} \frac{v_k/c}{k} \right. \\ & \left. + S_2(r)\, \frac{\dot{v}_k/c^2}{k} + \frac{\dot{\psi}+\dot{\phi}}{c}\, \bar{I}_\nu^{\rm dust} \right]. \end{aligned} \tag{A.23}$$

In this equation, $j_l(x)$ is the spherical Bessel function of order l, δ_k is the k-mode of the dark matter density contrast, v_k is the k-Fourier mode of the peculiar velocity field of the emitting sources and ψ and ϕ are the two scalar potentials perturbing the FRW metric (in the conformal Newtonian gauge). The functions $S_1(r)$ and $S_2(r)$ are defined by

$$\begin{aligned} S_1(r) \equiv & \int dL_{\nu(1+z[r])}\, dM\, G(M, L_{\nu(1+z[r])}) \\ & \times \frac{dn}{dM}\, \frac{a(r) L_{\nu(1+z[r])}}{4\pi}\, b(M, z[r]) \end{aligned} \tag{A.24}$$

and

$$\begin{aligned} S_2(r) \equiv & \int dL_{\nu(1+z[r])}\, dM\, G(M, L_{\nu(1+z[r])}) \\ & \times \frac{dn}{dM}\, \frac{a(r) L_{\nu(1+z[r])}}{4\pi}, \end{aligned} \tag{A.25}$$

respectively.

B

The angular correlation of line emission from star forming haloes

In this appendix I compute the angular power spectrum induced on the CMB by the emission of the lines described in Chapter 5. I shall follow the line of sight approach (los) already outlined in Appendix A, although here I shall make more emphasis on particular aspects related to the observing frequency resolution.
Let $B(\hat{\mathbf{n}}, \hat{\mathbf{n}}')$ be the PSF of the observing beam on the sphere unit vector $\hat{\mathbf{n}}'$ while pointing along $\hat{\mathbf{n}}$. Let also $\nu_{\rm obs}$ be the observing frequency of the experiment that measures the emission of a line of rest frequency ν and therefore probes the Universe at a redshift $1+z = \nu/\nu_{\rm obs}$. The spectral intensity introduced by such line reads

$$\begin{aligned} \Delta I_\nu &= \int dr \int d\hat{\mathbf{n}}\, B(\hat{\mathbf{n}}, \hat{\mathbf{n}}') \int d\nu'\, \phi_{\nu',\rm instr} \times \\ &\int d\mathbf{y}\, dL_{\nu'(1+z)} \frac{dn(\mathbf{y})}{dL_{\nu'(1+z)}} W(\mathbf{y}-\mathbf{r}') j_{\nu'(1+z)}\, a^3. \end{aligned} \tag{B.1}$$

$\phi_{\nu',\rm instr}$ is the frequency response of the experiment, and $dn/dL_{\nu'(1+z)}$ is the luminosity function of haloes hosting the metal/ionic species responsible for the line emission under study. The emissivity on the line at the center of the halo is given by $j_{\nu'(1+z')}$, which is diluted by cube power of the scale factor a.

The function $W(\mathbf{y}-\mathbf{r}')$ provides the profile of the density distribution of the species in the halo. The vector $\mathbf{r}'$ is determined by $\hat{\mathbf{n}}'$ and the frequency ν' providing the effective distance to the observer: $\mathbf{r}' = r'(\nu')\ \hat{\mathbf{n}}'$. At this point, all spatial coordinates are physical. As shown in Appendix A, the convolution in Equation (B.1) can be rewritten in terms of the source luminosity

$$\begin{aligned}\Delta I_\nu &= \int dr \int d\hat{\mathbf{n}}\ B(\hat{\mathbf{n}},\hat{\mathbf{n}}') \int d\nu'\ \phi_{\nu',\mathrm{instr}}\ \times \\ &\int dL_{\nu'(1+z)} \frac{d\tilde{n}(\mathbf{r}')}{dL_{\nu'(1+z)}} \frac{a^3\ L_{\nu'(1+z)}}{4\pi}.\end{aligned} \tag{B.2}$$

The new number density $d\tilde{n}/dL_{\nu'(1+z)}$ is just the previous one smoothed in scales corresponding to the typical halo size. The spectral luminosity can be expressed as a product of the bolometric luminosity on the line and the emission spectral profile, $L_{\nu'(1+z)} = L_{\mathrm{bol}}\psi_{\nu'(1+z)}$. We shall approximate this profile as a top hat function of the thermal width of the line, ($\psi_{\nu'(1+z)} = 1/(\Delta\nu)_{\mathrm{th}}$ if $|\nu'(1+z)-\nu| < (\Delta\nu)_{\mathrm{th}}$, $\psi_{\nu'(1+z)} = 0$ otherwise), and assume that this width will be much smaller than the instrumental one ($(\Delta\nu)_{\mathrm{th}}/\nu \ll (\Delta\nu)_{\mathrm{instr}}/\nu_{\mathrm{obs}}$). This enables the replacement of the integral along r by $cH^{-1}(z)(\Delta\nu)_{\mathrm{th}}/\nu$, yielding

$$\begin{aligned}\Delta I_\nu &= \int d\hat{\mathbf{n}}\ B(\hat{\mathbf{n}},\hat{\mathbf{n}}') \int d\nu'\ \phi_{\nu',\mathrm{instr}}\ \times \\ &\int dL_{\nu'(1+z)} \frac{dn(\mathbf{r}')}{dL_{\nu'(1+z)}} \frac{a^3\ \tilde{L}_{\nu'(1+z)}}{4\pi}\ cH^{-1}(z)\end{aligned} \tag{B.3}$$

where $\tilde{L_\nu} \equiv L_{\mathrm{bol}}/\nu$. This cancels any dependence on $(\Delta\nu)_{\mathrm{th}}$. Note that the halo number density is evaluated at $\mathbf{r}'$, and that the integral along the line of sight is carried out under the frequency response of the instrument:

$$\begin{aligned}\Delta I_\nu &= \int dr'\ \mathcal{P}(r-r') \int d\hat{\mathbf{n}}\ B(\hat{\mathbf{n}},\hat{\mathbf{n}}')\ \times \\ &\int dL_{\nu'(1+z)} \frac{dn(\mathbf{r}')}{dL_{\nu'(1+z)}} \frac{a^3\ \tilde{L}_{\nu'(1+z)}}{4\pi}\ cH^{-1}(z)\end{aligned} \tag{B.4}$$

The product $\mathcal{P}(r-r') \equiv \partial\nu'/(\partial r')\ \phi_{\nu',\mathrm{instr}}$ constitutes the radial profile of the los integration. We next attempt to show the impact that the shape of the radial (and angular) responses of the experiment have on the measured intensity. If we convert $\hat{\mathbf{n}}'$ into the transversal spatial component by introducing r'^2, Equation (B.4) reads like a convolution

$$\Delta I_\nu(\mathbf{r}) = \int d\mathbf{r}'\ \mathcal{B}(\mathbf{r}-\mathbf{r}')\ \tilde{I}_{\nu'(1+z)}(\mathbf{r}') \tag{B.5}$$

with $\mathcal{B}(\mathbf{r}-\mathbf{r}') \equiv \mathcal{P}(r-r')/r'^2$ and

$$\tilde{I}_{\nu'(1+z)}(\mathbf{r}') \equiv cH^{-1}(z) \int dL_{\nu'(1+z)} \frac{a^3\ \tilde{L}_{\nu'(1+z)}}{4\pi}\ \frac{d\tilde{n}(\mathbf{r}')}{dL_{\nu'(1+z)}}. \tag{B.6}$$

Here, $\mathcal{B}(\mathbf{r}-\mathbf{r}')$ represents the 3D window function of the instrumental response, and is responsible for some smoothing of the original signal $\tilde{I}_{\nu'(1+z)}(\mathbf{r}')$. This becomes more obvious if we rewrite the convolution in Fourier space

$$\Delta I_\nu(\mathbf{r}) = \int \frac{d\mathbf{k}}{(2\pi)^3}\ \exp\left(-i\mathbf{k}\cdot\mathbf{r}\right)\ \mathcal{B}_\mathbf{k}\ \tilde{I}_{\nu'(1+z)}(\mathbf{k}) \tag{B.7}$$

If the instrument is not sensitive to small scales (due to a poor angular *or* spectral resolution), then at large $\mathbf{k}$ the $\mathcal{B}_\mathbf{k}$ will vanish, suppressing the contribution of $\tilde{I}_{\nu'(1+z)}(\mathbf{k})$ at the same $\mathbf{k}$'s. This is also reflected in the difference scaling of the power spectra versus the spectral resolution of the experiment. Indeed, if we compute the power spectrum of $\Delta I_\nu(\mathbf{r})$ in terms of the halo power spectrum, we obtain

$$|\Delta I_{\nu,\mathbf{k}}|^2 \propto |\mathcal{B}_\mathbf{k}|^2\ P_h(k)\ \left(cH^{-1}(z)\frac{\tilde{L}_{\nu'(1+z)}}{4\pi}\frac{d\bar{n}}{dL_{\nu'(1+z)}}\right)^2, \tag{B.8}$$

with $d\bar{n}/dL_\nu$ the *average* number density of haloes per unit luminosity. If the haloes are Poisson distributed, then $P_h(k) \propto 1/(d\bar{n}/dL_{\nu'(1+z)})$ upto very large k-s, and the high-k integral is actually limited by the window function $\mathcal{B}_\mathbf{k}$ (as long as k corresponds to scales larger than the source size). On the contrary, if haloes are clustered so that their power spectrum is proportional to the linear matter density power spectrum $P_m(k)$, then we have that $P_m(k) \to 0$ for some large k, and the increase of spectral/angular resolution of the experiment will not make any difference at this large k range. *Therefore, improving the spectral resolution helps increasing the Poisson contribution, but does not change the contribution from the clustering term beyond some large $k_c = 2\pi/L_c$, with L_c the typical clustering scale.*

Having this present, following the same procedure of Appendix A.2, it is possible to write the angular correlation function of the intensity fluctuations as

$$\langle \Delta I_\nu(\hat{\mathbf{n}}_1)\, \Delta I_\nu(\hat{\mathbf{n}}_2)\rangle = \sum_l \frac{2l+1}{4\pi}\left(C_l^{\rm P} + C_l^{\rm C}\right) P_l(\hat{\mathbf{n}}_1\cdot\hat{\mathbf{n}}_2). \tag{B.9}$$

After switching to comoving units, the Poisson term $C_l^{\rm P}$ is given by

$$C_l^P = \left[r^2\ \frac{(\Delta\nu)_{\rm instr}}{\nu_{\rm obs}}\right]^{-1} \int dL_{\nu'(1+z)}\ cH^{-1}(z) \left(\frac{\tilde{L}_{\nu'(1+z)}}{4\pi}\right)^2 \frac{d\bar{n}}{dL_{\nu'(1+z)}}. \tag{B.10}$$

The correlation term can be written as

$$C_l^{\rm C} = \frac{2}{\pi} \int k^2 dk \, P_\psi(k) \, |\Delta_l(k)|^2, \tag{B.11}$$

with the transfer function $\Delta_l(k)$ given by

$$\Delta_l(k) = \int dr \, j_l(kr) \, \mathcal{P}(r) \, [S(r) \, \delta_k] \tag{B.12}$$

In this equation, $j_l(x)$ is the spherical Bessel function of order l, $\mathcal{P}(r)$ is the instrumental profile function as defined after Equation (B.4), δ_k is the k-mode of the dark matter density contrast, and the function $S(r)$ is defined by

$$\begin{aligned} S(r) \;\equiv\; & \int dL_{\nu'(1+z)} \, dM \, G(M, L_{\nu'(1+z)}) \\ & \times \frac{dn}{dM} \, \frac{\tilde{L}_{\nu'(1+z)}}{4\pi} \, cH^{-1}(z) \, b(M, z[r]). \end{aligned} \tag{B.13}$$

C

Useful cosmological formulae

In this Appendix I summarize some basic cosmological quantities which are very useful for the description of the properties of the haloes and their evolution. The fitting formulae presented here are retrieved from the literature and can be applied in a flat ΛCDM cosmology ($\Omega_{\rm m} + \Omega_\Lambda = 1$).

C.1. Growth factor

The growth factor for linear density fluctuations, normalized to unity at the present time is defined by

$$D(z) = D_0\, H(z) \int_z^\infty \frac{(1+z')dz'}{H^3(z')}. \tag{C.1}$$

This can be written, to a very good approximation, as (Carroll et al. 1992)

$$D(z) = \frac{g(z)}{g(0)(1+z)}, \tag{C.2}$$

where

$$g(z) \simeq \frac{5}{2}\Omega_{\rm m}(z)\left[\Omega_{{\rm m},z}^{4/7} - \Omega_{\Lambda,z} + \left(1+\frac{\Omega_{{\rm m},z}}{2}\right)\left(1+\frac{\Omega_{\Lambda,z}}{70}\right)\right], \tag{C.3}$$

with $\Omega_{\mathrm{m},z} = \Omega_{\mathrm{m}}(1+z)^3/E^2(z)$, $\Omega_{\Lambda,z} = \Omega_{\Lambda}/E^2(z)$ and

$$E(z) = \left[\Omega_{\mathrm{m}}(1+z)^3 + \Omega_{\Lambda}\right]^{1/2}. \tag{C.4}$$

C.2. Power spectrum

The evolution of the power spectrum of density fluctuations from an initial Harrison-Zel'dovich shape ($P(k) \propto k^n$, with $n = 1$) is governed by the transfer function $T(k)$

$$P(k) \propto kT^2(k) \tag{C.5}$$

This can be computed using the fitting formula of van den Bosch (2002)

$$T(k) = \frac{\ln(1+2.34q)}{2.34q}[1 + 3.89q + (16.1q)^2 + (5.46q)^3 + (6.71q)^4]^{-1/4}, \tag{C.6}$$

where $q = k/\Gamma$ and k is in units of $h\mathrm{Mpc}^{-1}$. The paramater Γ is called shape parameter and can be written as (Sugiyama 1995)

$$\Gamma = \Omega_{\mathrm{m}} h\, e^{-\Omega_{\mathrm{b}}(1+\sqrt{2h}/\Omega_{\mathrm{m}})}. \tag{C.7}$$

C.3. Mass variance

The mass variance of the Gaussian density field is given by the integral in the Fourier space

$$\sigma^2(M) = \frac{1}{(2\pi)^3}\int d^3k\, P(k)\, \hat{W}(kR) \tag{C.8}$$

where $P(k)$ is the power spectrum and $\hat{W}(kR)$ is a window function. For a spherical top-hat the filtering radius R is related to the mass by the simple relation $R = (M/\rho)^{1/3}$. The mass variance is usually normalized to σ_8, i.e. the value at a scale of 8 h^{-1} Mpc.
From the computational point of view is more convenient to use the fitting formula proposed by (van den Bosch 2002)

$$\sigma(M) = \sigma_8 \frac{f(u)}{f(u_8)}, \tag{C.9}$$

where

$$u = 2.804 \times 10^{-4}\, \Gamma \left(\frac{M}{\Omega_{\mathrm{m}}}\right)^{1/3}, \tag{C.10}$$

with M in units of $h^{-1}M_\odot$, and

$$f(u) = 64.087(1 + 1.074u^{0.3} - 1.581u^{0.4} + 0.954u^{0.5} - 0.185u^{0.6})^{-10} \quad \text{(C.11)}$$

This fit is claimed to be accurate to better than 0.5% in the mass range $10^6 \leq M \leq 10^{16}\, h^{-1}M_\odot$.

C.4. Critical density

The critical density for spherical collapse evolves with redshift according to the growth factor

$$\delta_{\rm cr}(z) = \frac{\delta_{\rm cr}}{D(z)} \quad \text{(C.12)}$$

where $\delta_{\rm cr} \simeq\simeq 1.69$ can be assumed constant. In reality this value has itself a very slight dependence on redshift, which can be parametrized as (Kitayama & Suto 1996)

$$\delta_{\rm cr} = \frac{3(12\pi)^{2/3}}{20}\left[1 + 0.0123\log\left(\frac{\Omega_{\rm m}}{\Omega_{\rm m} + \Omega_\Lambda(1+z)^3}\right)\right] \quad \text{(C.13)}$$

This correction, however, is smaller than 1%.

C.5. Halo bias factor

The halo relates the halo-halo autocorrelation with the mass-mass autocorrelation, for large separations: $\xi_{\rm hh}(r,z) = b^2(M,z)\xi_{\rm mm}(r,z)$. According to Mo & White (1996) the bias factor can be expressed as

$$b(M,z) = 1 + \frac{\nu^2(M,z) - 1}{\delta_{\rm cr}} \quad \text{(C.14)}$$

with

$$\nu = \frac{\delta_{\rm cr}}{D(z)\sigma(M)} \quad \text{(C.15)}$$

C.6. Distances

The comoving distance of an object at redshift z is given by the well-known formula (see e.g. Hogg 1999)

$$r_{\rm C} = \frac{c}{H_0}\int_0^z \frac{dz'}{E(z')} \quad \text{(C.16)}$$

where c is the speed of light and $c/H_0 \approx 3000\,h^{-1}$ Mpc.
Once the comoving distance is determined, it is easy to obtain the angular diameter distance r_A (defined as the ratio of the physical transverse size and the angular size of an object) and the luminosity distance r_L (which enters in the flux-luminosity relation). These three quantities are related by

$$r_\mathrm{L} = (1+z)\, r_\mathrm{C} = (1+z)^2\, r_\mathrm{A}. \tag{C.17}$$

Another useful quantity is the comoving volume element dV_C in a solid angle $d\Omega$ and a redshift slice dz. This is written as

$$\frac{dV_\mathrm{C}}{d\Omega} = r_\mathrm{C}^2 \frac{dr_\mathrm{C}}{dz} dz = \frac{c}{H_0} \frac{r_\mathrm{C}^2}{E(z)} dz. \tag{C.18}$$

References

Alexander, D. M., Bauer, F. E., Chapman, S. C., Smail, I., Blain, A. W., Brandt, W. N., Ivison, R. J. (2005a), *The X-ray spectral properties of SCUBA galaxies*, ApJ, 632, 736

Alexander, D. M., Smail, I., Bauer, F. E., Chapman, S. C., Blain, A. W., Brandt, W. N., Ivison, R. J. (2005b), *Rapid growth of black holes in massive star-forming galaxies*, Nature, 434, 738

Alton, P. B., Davies, J. I., Bianchi, S. (1999), *Dust outflows from starburst galaxies*, A&A, 343, 51

Andreani, P., Cimatti, A., Loinard, L., Röttgering, H. (2000), *CO detection of the extremely red galaxy HR10*, A&A, 354, L1

Baan, W. A., Henkel, C., Loenen, A. F., Baudry, A., Wiklind, T. (2008), *Dense gas in luminous infrared galaxies*, A&A, 477, 747

Baker, A. J., Tacconi, L. J., Genzel, R., Lehnert, M. D., Lutz, D. (2004), *Molecular gas in the lensed lyman break galaxy cB58*, ApJ, 604, 125

Barvainis, R., Alloin, D., Bremer, M. (2002), *A CO survey of gravitationally lensed quasars with the IRAM interferometer*, A&A, 385, 399

Barvainis, R., Maloney, P., Antonucci, R., Alloin, D. (1997), *Multiple CO transitions, CI, and HCN from the Cloverleaf quasar*, ApJ, 484, 695

Barvainis, R., Tacconi, L., Antonucci, R., Alloin, D., Coleman, P. (1994), *Extremely strong carbon-monoxide emission from the Cloverleaf quasar at a redshift of 2.5*, Nature, 371, 586

Basu, K., Hernández-Monteagudo, C., Sunyaev, R. A. (2004), *CMB observations and the production of chemical elements at the end of the dark ages*, A&A, 416, 447

Bayet, E., Gerin, M., Phillips, T. G., Contursi, A. (2006), *A survey of submillimeter C and CO lines in nearby galaxies*, A&A, 460, 467

Bennett, C. L., Halpern, M., Hinshaw, G., Jarosik, N., Kogut, A., Limon, M., Meyer, S. S., Page, L., Spergel, D. N., Tucker, G. S., Wollack, E., Wright, E. L., Barnes, C., Greason, M. R., Hill, R. S., Komatsu, E., Nolta, M. R., Odegard, N., Peiris, H. V., Verde, L., Weiland, J. L. (2003), *First-Year Wilkinson Microwave Anisotropy Probe (WMAP) observations: preliminary maps and basic results*, ApJS, 148, 1

Benson, A. J., Kamionkowski, M., Hassani, S. H. (2005), *Self-consistent theory of halo mergers*, MNRAS, 357, 847

Bersanelli, M., Mandolesi, N. (2000), *Design concept of the Planck-LFI instrument*, Astrophysical Letters Communications, 37, 171

Bertoldi, F., Carilli, C., Aravena, M., Schinnerer, E., Voss, H., Smolcic, V., Jahnke, K., Scoville, N., Blain, A., Menten, K. M., Lutz, D., Brusa, M., Taniguchi, Y., Capak, P., Mobasher, B., Lilly, S., Thompson, D., Aussel, H., Kreysa, E., Hasinger, G., Aguirre, J., Schlaerth, J., Koekemoer, A. (2007), *COSBO: The MAMBO 1.2 millimeter imaging survey of the COSMOS field*, ApJS, 172, 132

Blain, A. W. (1999), *Dust temperature and the submillimetre-radio flux density ratio as a redshift indicator for distant galaxies*, MNRAS, 309, 955

Blain, A. W., Smail, I., Ivison, R. J., Kneib, J.-P., Frayer, D. T. (2002), *Submillimeter galaxies*, Phys. Rep., 369, 111

Brown, R. L., Vanden Bout, P. A. (1991), *CO emission at* $z = 2.2867$ *in the galaxy IRAS F10214+4724*, AJ, 102, 1956

Buat, V., Marcillac, D., Burgarella, D., Le Floc'h, E., Takeuchi, T. T., Iglesias-Paràmo, J., Xu, C. K. (2007), *The ultraviolet properties of luminous infrared galaxies at z ˜ 0.7. Is there any evolution in their dust attenuation?*, A&A, 469, 19

Carilli, C. L., Cox, P., Bertoldi, F., Menten, K. M., Omont, A., Djorgovski, S. G., Petric, A., Beelen, A., Isaak, K. G., McMahon, R. G. (2002), *Imaging low-order CO emission from the* $z = 4.12$ *Quasi-Stellar Object PSS J2322+1944*, ApJ, 575, 145

Carroll, S. M., Press, W. H., Turner, E. L. (1992), *The cosmological constant*, ARA&A, 30, 499

Chapman, S. C., Blain, A. W., Smail, I., Ivison, R. J. (2005), *A redshift survey of the submillimeter galaxy population*, ApJ, 622, 772

Combes, F., Maoli, R., Omont, A. (1999), *CO lines in high redshift galaxies: perspective for future MM instruments*, A&A, 345, 369

Coppin, K., Chapin, E. L., Mortier, A. M. J., Scott, S. E., Borys, C., Dunlop, J. S., Halpern, M., Hughes, D. H., Pope, A., Scott, D., Serjeant, S., Wagg, J., Alexander, D. M., Almaini, O., Aretxaga, I., Babbedge, T., Best, P. N., Blain, A., Chapman, S., Clements, D. L., Crawford, M., Dunne, L., Eales, S. A., Edge, A. C., Farrah, D., Gaztañaga, E., Gear, W. K., Granato, G. L., Greve, T. R., Fox, M., Ivison, R. J., Jarvis, M. J., Jenness, T., Lacey, C., Lepage, K., Mann, R. G., Marsden, G., Martinez-Sansigre, A., Oliver, S., Page, M. J., Peacock, J. A., Pearson, C. P., Percival, W. J., Priddey, R. S., Rawlings, S., Rowan-Robinson, M., Savage, R. S., Seigar, M., Sekiguchi, K., Silva, L., Simpson, C., Smail, I., Stevens, J. A., Takagi, T., Vaccari, M., van Kampen, E., Willott, C. J. (2006), *The SCUBA Half-Degree Extragalactic Survey - II. Submillimetre maps, catalogue and number counts*, MNRAS, 372, 1621

Cortese, L., Boselli, A., Buat, V., Gavazzi, G., Boissier, S., Gil de Paz, A., Seibert, M., Madore, B. F., Martin, D. C. (2006), *UV dust attenuation in normal star-forming galaxies. I. Estimating the $L_{\rm TIR}/L_{\rm FUV}$ ratio*, ApJ, 637, 242

Cox, A. N. (2000), *Allen's astrophysical quantities*, Allen's astrophysical quantities, 4th ed. Publisher: New York: AIP Press; Springer, 2000. Editedy by Arthur N. Cox. ISBN: 0387987460

Cox, P., Omont, A., Djorgovski, S. G., Bertoldi, F., Pety, J., Carilli, C. L., Isaak, K. G., Beelen, A., McMahon, R. G., Castro, S. (2002), *CO and dust in PSS 2322+1944 at a redshift of 4.12*, A&A, 387, 406

De Breuck, C., Neri, R., Morganti, R., Omont, A., Rocca-Volmerange, B., Stern, D., Reuland, M., van Breugel, W., Röttgering, H., Stanford, S. A., Spinrad, H., Vigotti, M., Wright, M. (2003a), *CO emission and associated HI absorption from a massive gas reservoir surrounding the z = 3 radio galaxy B3 J2330+3927*, A&A, 401, 911

De Breuck, C., Neri, R., Omont, A. (2003b), *CO emission from $z \gtrsim 3$ radio galaxies*, New Astronomy Review, 47, 285

de Zotti, G., Ricci, R., Mesa, D., Silva, L., Mazzotta, P., Toffolatti, L., González-Nuevo, J. (2005), *Predictions for high-frequency radio surveys of extragalactic sources*, A&A, 431, 893

Downes, D., Solomon, P. M. (2003), *Molecular Gas and Dust at z=2.6 in SMM J14011+0252: a strongly lensed ultraluminous galaxy, not a huge massive disk*, ApJ, 582, 37

Downes, D., Solomon, P. M., Radford, S. J. E. (1995), *New observations and a new interpretation of CO(3-2) in IRAS F10214+4724*, ApJ, 453, L65

Dunne, L., Eales, S. A. (2001), *The SCUBA Local Universe Galaxy Survey - II. 450-μm data: evidence for cold dust in bright IRAS galaxies*, MNRAS, 327, 697

Erb, D. K., Shapley, A. E., Pettini, M., Steidel, C. C., Reddy, N. A., Adelberger, K. L. (2006), *The mass-metallicity relation at $z \gtrsim 2$*, ApJ, 644, 813

Fan, X. (2006), *Evolution of high-redshift quasars*, New Astronomy Review, 50, 665

Fixsen, D. J., Bennett, C. L., Mather, J. C. (1999), *COBE Far Infrared Absolute Spectrophotometer observations of galactic lines*, ApJ, 526, 207

Fixsen, D. J., Dwek, E., Mather, J. C., Bennett, C. L., Shafer, R. A. (1998), *The spectrum of the extragalactic far-infrared background from the COBE FIRAS observations*, ApJ, 508, 123

Fixsen, D. J., Mather, J. C. (2002), *The spectral results of the Far-Infrared Absolute Spectrophotometer instrument on COBE*, ApJ, 581, 817

Frayer, D. T., Ivison, R. J., Scoville, N. Z., Evans, A. S., Yun, M. S., Smail, I., Barger, A. J., Blain, A. W., Kneib, J.-P. (1999), *Molecular gas in the $z = 2.565$ submillimeter galaxy SMM J14011+0252*, ApJ, 514, L13

Gao, Y., Lo, K. Y., Lee, S.-W., Lee, T.-H. (2001), *Molecular gas and the modest star formation efficiency in the "Antennae" galaxies: Arp 244=NGC 4038/9*, ApJ, 548, 172

Genzel, R., Baker, A. J., Tacconi, L. J., Lutz, D., Cox, P., Guilloteau, S., Omont, A. (2003), *Spatially resolved millimeter interferometry of SMM J02399-0136: a very massive galaxy at* $z = 2.8$, ApJ, 584, 633

González-Nuevo, J., Toffolatti, L., Argüeso, F. (2005), *Predictions of the angular power spectrum of clustered extragalactic point sources at Cosmic Microwave Background frequencies from flat and all-sky two-dimensional simulations*, ApJ, 621, 1

Granato, G. L., De Zotti, G., Silva, L., Bressan, A., Danese, L. (2004), *A physical model for the coevolution of QSOs and their spheroidal hosts*, ApJ, 600, 580

Greve, T. R., Bertoldi, F., Smail, I., Neri, R., Chapman, S. C., Blain, A. W., Ivison, R. J., Genzel, R., Omont, A., Cox, P., Tacconi, L., Kneib, J.-P. (2005), *An interferometric CO survey of luminous submillimetre galaxies*, MNRAS, 359, 1165

Greve, T. R., Ivison, R. J., Papadopoulos, P. P. (2003), *Gas and dust in the extremely red object ERO J164502+4626.4*, ApJ, 599, 839

Greve, T. R., Sommer-Larsen, J. (2008), *CO line emission from Lyman break galaxies. Cosmological simulations and predictions for ALMA*, A&A, 480, 335

Guilloteau, S., Omont, A., Cox, P., McMahon, R. G., Petitjean, P. (1999), *Dust and CO lines in high redshift quasars*, A&A, 349, 363

Güsten, R., Nyman, L. Å., Schilke, P., Menten, K., Cesarsky, C., Booth, R. (2006), *The Atacama Pathfinder EXperiment (APEX) - a new submillimeter facility for southern skies*, A&A, 454, L13

Haiman, Z., Knox, L. (2000), *Correlations in the far-infrared background*, ApJ, 530, 124

Hainline, L. J., Blain, A. W., Greve, T. R., Chapman, S. C., Smail, I., Ivison, R. J. (2006), *Observing cold gas in submillimeter galaxies: detection of CO (1-0) emission in SMM J13120+4242 with the Green Bank Telescope*, ApJ, 650, 614

Hainline, L. J., Scoville, N. Z., Yun, M. S., Hawkins, D. W., Frayer, D. T., Isaak, K. G. (2004), *A study of CO emission in high-redshift QSOs using the Owens Valley Millimeter Array*, ApJ, 609, 61

Heckman, T. M., Robert, C., Leitherer, C., Garnett, D. R., van der Rydt, F. (1998), *The ultraviolet spectroscopic properties of local starbursts: implications at high redshift*, ApJ, 503, 646

Heger, A., Woosley, S. E. (2002), *The nucleosynthetic signature of population III*, ApJ, 567, 532

Hernández-Monteagudo, C., Haiman, Z., Jimenez, R., Verde, L. (2007), *Oxygen pumping: probing intergalactic metals at the epoch of reionization*, ApJ, 660, L85

Hernández-Monteagudo, C., Haiman, Z., Verde, L., Jimenez, R. (2008), *Oxygen pumping. II. probing the inhomogeneous metal enrichment at the epoch of reionization with high-frequency CMB observations*, ApJ, 672, 33

Hernández-Monteagudo, C., Verde, L., Jimenez, R., Spergel, D. N. (2006), *Correlation properties of the kinematic Sunyaev-Zel'dovich effect and implications for dark energy*, ApJ, 643, 598

Hernquist, L., Springel, V. (2003), *An analytical model for the history of cosmic star formation*, MNRAS, 341, 1253

Hildebrand, R. H. (1983), *The determination of cloud masses and dust characteristics from submillimetre thermal emission*, QJRAS, 24, 267

Hogg, D. W. (1999), *Distance measures in cosmology*, ArXiv Astrophysics e-prints

Hopkins, A. M. (2004), *On the evolution of star-forming galaxies*, ApJ, 615, 209

Hopkins, A. M., Beacom, J. F. (2006), *On the normalization of the cosmic star formation history*, ApJ, 651, 142

Inoue, A. K., Kamaya, H. (2004), *Amount of intergalactic dust: constraints from distant supernovae and the thermal history of the intergalactic medium*, MNRAS, 350, 729

Kennicutt, Jr., R. C. (1998), *Star formation in galaxies along the Hubble sequence*, ARA&A, 36, 189

Kitayama, T., Susa, H., Umemura, M., Ikeuchi, S. (2001), *Criteria for the formation of Population III objects in the ultraviolet background radiation*, MNRAS, 326, 1353

Kitayama, T., Suto, Y. (1996), *Semianalytic predictions for statistical properties of X-ray clusters of galaxies in Cold Dark Matter universes*, ApJ, 469, 480

Kitayama, T., Yoshida, N., Susa, H., Umemura, M. (2004), *The Structure and evolution of early cosmological HII regions*, ApJ, 613, 631

Kneib, J.-P., Neri, R., Smail, I., Blain, A., Sheth, K., van der Werf, P., Knudsen, K. K. (2005), *Molecular gas in a $z \sim 2.5$ triply-imaged, sub-mJy submillimetre galaxy typical of the cosmic far-infrared background*, A&A, 434, 819

Kneib, J.-P., van der Werf, P. P., Kraiberg Knudsen, K., Smail, I., Blain, A., Frayer, D., Barnard, V., Ivison, R. (2004), *A multiply imaged, submillimetre-selected ultraluminous infrared galaxy in a galaxy group at $z \sim 2.5$*, MNRAS, 349, 1211

Knudsen, K. K., Barnard, V. E., van der Werf, P. P., Vielva, P., Kneib, J.-P., Blain, A. W., Barreiro, R. B., Ivison, R. J., Smail, I., Peacock, J. A. (2006), *An ultradeep submillimetre map: beneath the SCUBA confusion limit with lensing and robust source extraction*, MNRAS, 368, 487

Kohno, K. (2005), *The Atacama Submillimeter Telescope Experiment*, in *The cool universe: observing cosmic dawn*, edited by C. Lidman, D. Alloin, volume 344 of *Astronomical Society of the Pacific Conference Series*, 242

Komatsu, E., Kitayama, T. (1999), *Sunyaev-Zeldovich fluctuations from spatial correlations between clusters of galaxies*, ApJ, 526, L1

Kosowsky, A. (2006), *The Atacama Cosmology Telescope project: a progress report*, New Astronomy Review, 50, 969

Kovács, A., Chapman, S. C., Dowell, C. D., Blain, A. W., Ivison, R. J., Smail, I., Phillips, T. G. (2006), *SHARC-2 350 μm observations of distant submillimeter-selected galaxies*, ApJ, 650, 592

Lacey, C., Cole, S. (1993), *Merger rates in hierarchical models of galaxy formation*, MNRAS, 262, 627

Lagache, G., Puget, J.-L., Dole, H. (2005), *Dusty infrared galaxies: sources of the cosmic infrared background*, ARA&A, 43, 727

Lamarre, J.-M., Puget, J. L., Piat, M., Ade, P. A. R., Lange, A. E., Benoit, A., De Bernardis, P., Bouchet, F. R., Bock, J. J., Desert, F. X., Emery, R. J., Giard, M., Maffei, B., Murphy, J. A., Torre, J.-P., Bhatia, R., Sudiwala, R. V., Yourchenko, V. (2003), *Planck high-frequency instrument*, in *IR Space Telescopes and Instruments. Edited by John C. Mather . Proceedings of the SPIE, Volume 4850, pp. 730-739 (2003).*, edited by J. C. Mather, volume 4850 of *Presented at the Society of Photo-Optical Instrumentation Engineers (SPIE) Conference*, 730–739

Laurent, G. T., Aguirre, J. E., Glenn, J., Ade, P. A. R., Bock, J. J., Edgington, S. F., Goldin, A., Golwala, S. R., Haig, D., Lange, A. E., Maloney, P. R., Mauskopf, P. D., Nguyen, H., Rossinot, P., Sayers, J., Stover, P. (2005), *The Bolocam Lockman Hole millimeter-wave galaxy survey: galaxy candidates and number counts*, ApJ, 623, 742

Li, A., Draine, B. T. (2002), *Infrared emission from interstellar dust. III. The Small Magellanic Cloud*, ApJ, 576, 762

Madau, P., Ferguson, H. C., Dickinson, M. E., Giavalisco, M., Steidel, C. C., Fruchter, A. (1996), *High-redshift galaxies in the Hubble Deep Field: colour selection and star formation history to* $z \sim 4$, MNRAS, 283, 1388

Madau, P., Pozzetti, L., Dickinson, M. (1998), *The star formation history of field galaxies*, ApJ, 498, 106

Malhotra, S., Kaufman, M. J., Hollenbach, D., Helou, G., Rubin, R. H., Brauher, J., Dale, D., Lu, N. Y., Lord, S., Stacey, G., Contursi, A., Hunter, D. A., Dinerstein, H. (2001), *Far-infrared spectroscopy of normal galaxies: physical conditions in the interstellar medium*, ApJ, 561, 766

Mayya, Y. D., Bressan, A., Carrasco, L., Hernandez-Martinez, L. (2006), *The star formation history of the disk of the starburst galaxy M82*, ApJ, 649, 172

Mihos, J. C., Hernquist, L. (1994), *Ultraluminous starbursts in major mergers*, ApJ, 431, L9

Mihos, J. C., Hernquist, L. (1996), *Gasdynamics and starbursts in major mergers*, ApJ, 464, 641

Mo, H. J., White, S. D. M. (1996), *An analytic model for the spatial clustering of dark matter haloes*, MNRAS, 282, 347

Neri, R., Genzel, R., Ivison, R. J., Bertoldi, F., Blain, A. W., Chapman, S. C., Cox, P., Greve, T. R., Omont, A., Frayer, D. T. (2003), *Interferometric observations of powerful CO emission from three submillimeter galaxies at* $z = 2.39$*,* 2.51*, and* 3.35, ApJ, 597, L113

Papadopoulos, P. P., Röttgering, H. J. A., van der Werf, P. P., Guilloteau, S., Omont, A., van Breugel, W. J. M., Tilanus, R. P. J. (2000), *CO (4-3) and dust emission in two powerful high-z radio galaxies, and CO lines at high redshifts*, ApJ, 528, 626

Planesas, P., Martin-Pintado, J., Neri, R., Colina, L. (1999), *Gas-rich galaxy pair unveiled in the lensed quasar 0957+561.*, Science, 286, 2493

Pope, A., Chary, R.-R., Alexander, D. M., Armus, L., Dickinson, M., Elbaz, D., Frayer, D., Scott, D., Teplitz, H. (2008), *Mid-infrared spectral diagnosis of submillimeter galaxies*, ApJ, 675, 1171

Press, W. H., Schechter, P. (1974), *Formation of galaxies and clusters of galaxies by self-similar gravitational condensation*, ApJ, 187, 425

Reach, W. T., Dwek, E., Fixsen, D. J., Hewagama, T., Mather, J. C., Shafer, R. A., Banday, A. J., Bennett, C. L., Cheng, E. S., Eplee, Jr., R. E., Leisawitz, D., Lubin, P. M., Read, S. M., Rosen, L. P., Shuman, F. G. D., Smoot, G. F., Sodroski, T. J., Wright, E. L. (1995), *Far-infrared spectral observations of the Galaxy by COBE*, ApJ, 451, 188

Ricotti, M., Shull, J. M. (2000), *Feedback from galaxy formation: escaping ionizing radiation from galaxies at high redshift*, ApJ, 542, 548

Righi, M., Hernández-Monteagudo, C., Sunyaev, R. A. (2008), *The clustering of merging star-forming haloes: dust emission as high frequency arcminute CMB foreground*, A&A, 478, 685

Robertson, B., Bullock, J. S., Cox, T. J., Di Matteo, T., Hernquist, L., Springel, V., Yoshida, N. (2006), *A merger-driven scenario for cosmological disk galaxy formation*, ApJ, 645, 986

Ruhl, J., Ade, P. A. R., Carlstrom, J. E., Cho, H.-M., Crawford, T., Dobbs, M., Greer, C. H., Halverson, N. w., Holzapfel, W. L., Lanting, T. M., Lee, A. T., Leitch, E. M., Leong, J., Lu, W., Lueker, M., Mehl, J., Meyer, S. S., Mohr, J. J., Padin, S., Plagge, T., Pryke, C., Runyan, M. C., Schwan, D.,

Sharp, M. K., Spieler, H., Staniszewski, Z., Stark, A. A. (2004), *The South Pole Telescope*, in *Proceedings of the SPIE, Volume 5498, pp. 11-29.*

Sanders, D. B., Mazzarella, J. M., Kim, D.-C., Surace, J. A., Soifer, B. T. (2003), *The IRAS Revised Bright Galaxy Sample*, AJ, 126, 1607

Sanders, D. B., Mirabel, I. F. (1996), *Luminous infrared galaxies*, ARA&A, 34, 749

Schlegel, D. J., Finkbeiner, D. P., Davis, M. (1998), *Maps of dust infrared emission for use in estimation of reddening and Cosmic Microwave Background radiation foregrounds*, ApJ, 500, 525

Scott, D., White, M. (1999), *Implications of SCUBA observations for the Planck surveyor*, A&A, 346, 1

Sebring, T. A., Giovanelli, R., Radford, S., Zmuidzinas, J. (2006), *Cornell Caltech Atacama Telescope (CCAT): a 25-m aperture telescope above 5000-m altitude*, in *Proceedings of the SPIE, Volume 6267, pp. 62672C.*

Seljak, U., Zaldarriaga, M. (1996), *A line-of-sight integration approach to Cosmic Microwave Background anisotropies*, ApJ, 469, 437

Sheth, K., Blain, A. W., Kneib, J.-P., Frayer, D. T., van der Werf, P. P., Knudsen, K. K. (2004), *Detection of CO from SMM J16359+6612, the multiply imaged submillimeter galaxy behind A2218*, ApJ, 614, L5

Sheth, R. K., Diaferio, A. (2001), *Peculiar velocities of galaxies and clusters*, MNRAS, 322, 901

Silk, J., Spaans, M. (1997), *Molecular lines as diagnostics of high-redshift objects*, ApJ, 488, L79

Solomon, P. M., Downes, D., Radford, S. J. E. (1992a), *Warm molecular gas in the primeval galaxy IRAS 10214+4724*, ApJ, 398, L29

Solomon, P. M., Radford, S. J. E., Downes, D. (1992b), *Molecular gas content of the primaeval galaxy IRAS 10214+4724*, Nature, 356, 318

Solomon, P. M., Vanden Bout, P. A. (2005), *Molecular gas at high redshift*, ARA&A, 43, 677

Song, Y.-S., Cooray, A., Knox, L., Zaldarriaga, M. (2003), *The far-infrared background correlation with Cosmic Microwave Background lensing*, ApJ, 590, 664

Spergel, D. N., Bean, R., Doré, O., Nolta, M. R., Bennett, C. L., Dunkley, J., Hinshaw, G., Jarosik, N., Komatsu, E., Page, L., Peiris, H. V., Verde, L., Halpern, M., Hill, R. S., Kogut, A., Limon, M., Meyer, S. S., Odegard, N., Tucker, G. S., Weiland, J. L., Wollack, E., Wright, E. L. (2007), *Three-Year Wilkinson Microwave Anisotropy Probe (WMAP) observations: implications for cosmology*, ApJS, 170, 377

Springel, V., Hernquist, L. (2005), *Formation of a spiral galaxy in a major merger*, ApJ, 622, L9

Suginohara, M., Suginohara, T., Spergel, D. N. (1999), *Detecting $z > 10$ objects through carbon, nitrogen, and oxygen emission lines*, ApJ, 512, 547

Sugiyama, N. (1995), *Cosmic background anisotropies in Cold Dark Matter cosmology*, ApJS, 100, 281

Sunyaev, R. A., Zeldovich, I. B. (1980), *Microwave background radiation as a probe of the contemporary structure and history of the universe*, ARA&A, 18, 537

Sunyaev, R. A., Zeldovich, Y. B. (1972), *The observations of relic radiation as a test of the nature of X-ray radiation from the clusters of galaxies*, Comments on Astrophysics and Space Physics, 4, 173

Sutherland, R. S., Dopita, M. A. (1993), *Cooling functions for low-density astrophysical plasmas*, ApJS, 88, 253

Tacconi, L. J., Neri, R., Chapman, S. C., Genzel, R., Smail, I., Ivison, R. J., Bertoldi, F., Blain, A., Cox, P., Greve, T., Omont, A. (2006), *High-resolution millimeter imaging of submillimeter galaxies*, ApJ, 640, 228

Takata, T., Sekiguchi, K., Smail, I., Chapman, S. C., Geach, J. E., Swinbank, A. M., Blain, A., Ivison, R. J. (2006), *Rest-frame optical spectroscopic classifications for submillimeter galaxies*, ApJ, 651, 713

Tarenghi, M., Wilson, T. L. (2005), *The ALMA project*, in *EAS Publications Series*, edited by L. I. Gurvits, S. Frey, S. Rawlings, 423–430

Tauber, J. A. (2004), *The Planck mission*, Advances in Space Research, 34, 491

Tegmark, M., Eisenstein, D. J., Hu, W., de Oliveira-Costa, A. (2000), *Foregrounds and forecasts for the Cosmic Microwave Background*, ApJ, 530, 133

Toffolatti, L., Argueso Gomez, F., de Zotti, G., Mazzei, P., Franceschini, A., Danese, L., Burigana, C. (1998), *Extragalactic source counts and contributions to the anisotropies of the cosmic microwave background: predictions for the Planck Surveyor mission*, MNRAS, 297, 117

Toffolatti, L., Negrello, M., González-Nuevo, J., de Zotti, G., Silva, L., Granato, G. L., Argüeso, F. (2005), *Extragalactic source contributions to arcminute-scale Cosmic Microwave Background anisotropies*, A&A, 438, 475

Tremonti, C. A., Heckman, T. M., Kauffmann, G., Brinchmann, J., Charlot, S., White, S. D. M., Seibert, M., Peng, E. W., Schlegel, D. J., Uomoto, A., Fukugita, M., Brinkmann, J. (2004), *The origin of the mass-metallicity relation: insights from 53,000 star-forming galaxies in the Sloan Digital Sky Survey*, ApJ, 613, 898

van den Bosch, F. C. (2002), *The universal mass accretion history of cold dark matter haloes*, MNRAS, 331, 98

Weingartner, J. C., Draine, B. T. (2001), *Dust grain-size distributions and extinction in the Milky Way, Large Magellanic Cloud, and Small Magellanic Cloud*, ApJ, 548, 296

Weiß, A., Downes, D., Walter, F., Henkel, C. (2005a), *Multiple CO lines in SMM J16359+6612 - further evidence for a merger*, A&A, 440, L45

Weiß, A., Henkel, C., Downes, D., Walter, F. (2003), *Gas and dust in the Cloverleaf quasar at redshift 2.5*, A&A, 409, L41

Weiß, A., Walter, F., Scoville, N. Z. (2005b), *The spectral energy distribution of CO lines in M 82*, A&A, 438, 533

Wilner, D. J., Zhao, J.-H., Ho, P. T. P. (1995), *The molecular medium of H1413+117: BIMA CO(3-2) and HCO^+ (4-3) observations*, ApJ, 453, L91

Wright, E. L., Mather, J. C., Bennett, C. L., Cheng, E. S., Shafer, R. A., Fixsen, D. J., Eplee, Jr., R. E., Isaacman, R. B., Read, S. M., Boggess,

N. W., Gulkis, S., Hauser, M. G., Janssen, M., Kelsall, T., Lubin, P. M., Meyer, S. S., Moseley, Jr., S. H., Murdock, T. L., Silverberg, R. F., Smoot, G. F., Weiss, R., Wilkinson, D. T. (1991), *Preliminary spectral observations of the Galaxy with a 7 deg beam by the Cosmic Background Explorer (COBE)*, ApJ, 381, 200

Yoshida, N., Omukai, K., Hernquist, L., Abel, T. (2006), *Formation of primordial stars in a ΛCDM universe*, ApJ, 652, 6

Zeldovich, Y. B., Syunyaev, R. A. (1980), *The angular distribution of the microwave background, and its intensity in the direction of galaxy clusters*, Soviet Astronomy Letters, 6, 285

Curriculum vitae

Personal data

First Name:	Mattia
Last name:	Righi
Date of birth:	May 9th, 1980
Place of birth:	Rovereto, TN (Italy)
Nationality:	Italian
Civil status:	single

Contacts

Permanent address:	via S. Caterina, 69 38062 Arco, TN (Italy)
Current address:	Max-Planck-Institut für Astrophysik (MPA) Karl-Schwarzschild-Strasse, 1 D-85741 Garching bei München (Germany)
e-mail:	righi@mpa-garching.mpg.de
Phone:	+49 (0)89 30000 2328
Fax:	+49 (0)89 30000 2235

Languages

Italian:	mother tongue
English:	excellent (TOEFL score 250/300)
German:	basic level

Computer skills

Operating systems:	Windows, Unix, Linux
Programming languages:	Fortran 77, Fortran 90
Graphic languages:	SuperMongo, IDL
Textual languages:	LaTeX, PowerPoint
Image data reduction:	AIPS

Education

September, 2004 – now:
PhD Student
Max-Planck-Institut für Astrophysik (MPA) - Garching (Germany)
PhD Thesis: *CO lines and dust emission from merging star-forming galaxies as CMB foregrounds*
Supervisor: Prof. Dr. Rashid Sunyaev

July 16, 2004:
Laurea in Astronomy
Alma Mater Studiorum - University of Bologna (Italy)
Laurea Thesis: *Numerical simulation of the Rees-Sciama effect in dark energy cosmological models*
Supervisor: Prof. Lauro Moscardini
Final score: 110/110 *cum laude*

September 1999 – July 2004:
Undergraduate student
Alma Mater Studiorum - University of Bologna (Italy)
Faculty of Mathematical, Physical and Natural Sciences
Department of Astronomy
Graduate point average: 29.2/30

July 16, 1999:
Diploma of Maturità Scientifica
Liceo Scientifico "A. Maffei" - Riva del Garda, TN (Italy)
Final score: 87/100

Talks and seminars

December 20, 2007:
Invited talk
Dust emission from merging galaxies as CMB foreground
INAF - Osservatorio astronomico di Bologna (Italy)

July 23, 2007:
MPA institute seminar
Dust emission from merging galaxies as CMB foreground
Max-Planck-Institut für Astrophysik (MPA) - Garching (Germany)

February 27, 2004:
PhD candidate talk
Numerical simulations of the Rees-Sciama effect
Max-Planck-Institut für Astrophysik (MPA) - Garching (Germany)

Schools and conferences

October 2007:
From planets to dark energy - The modern radio universe
Manchester (UK)
Poster presented

August 2007:
A century of Cosmology - Past, present and future
San Servolo, Venice (Italy)
Poster presented

October 2006:
Ecole Internationale Daniel Chalonge
Physics of the early universe confronts observations: WMAP 2006
Paris (France)

June 2005:
Reionizing the universe - The epoch of reionization and the physics of the IGM
Kapteyn Institute - Department of Astronomy
Groningen (The Netherlands)

September 2004 – 2007:
IMPRS on Astrophysics - Introductory course and 3 advanced courses
Max-Planck-Institut für Astrophysik (MPA)
Garching (Germany)

May 2004:
Scuola Nazionale di Astrofisica
Gravitational lensing – Chaos and its astrophysical consequencies
Bertinoro, FC (Italy)

Teaching exeprience

March 2001: Lectures on General Astronomy for kids
Scuola Media "A. Frank"
Villa Lagarina, TN (Italy)

Publications

M. Righi, C. Hernández-Monteagudo, R.A. Sunyaev
Carbon monoxide line emission as a CMB foreground: tomography of the star-forming universe with different spectral resolutions
Accepted for publication by *A&A*

M. Righi, C. Hernández-Monteagudo, R.A. Sunyaev
The clustering of merging star-forming haloes: dust emission as high frequency arcminute CMB foreground
A&A **478**, 685 (2008)